

UNIVERSITÀ DEGLI STUDI DI PAVIA
FACOLTÀ DI INGEGNERIA

DOTTORATO DI RICERCA IN
INGEGNERIA ELETTRONICA, INFORMATICA
ED ELETTRICA
CICLO XXX A.A. 2016-2017



**ANALYSIS AND DESIGN
OF PROTECTIVE STRUCTURES FOR
FEED AND REFLECTOR ANTENNAS**

DOCTORAL THESIS OF
ANDREA MARTELLOSIO

TUTOR: PROFESSOR MARCO PASIAN



Index

Index	1
Acknowledgments	3
Acronyms and Abbreviations	4
Preface	7
1 Introduction	10
2 Radomes for Ground Stations in Polar Regions	17
2.1 Large Ground Based Radomes	20
2.2 MLR Radomes: study and analysis	23
2.2.1 MLR Wall	23
2.2.2 MLR Interconnection	27
2.3 SNOWBEAR System	30
2.3.1 Antenna Architecture	30
2.3.2 Antenna Analysis	32
2.3.3 Preliminary test in Mainz	35
2.3.4 Preliminary test in Svalbard	38
2.4 Rainy Conditions	40
2.5 Down-Link Performance	47
2.5.1 Gain over Temperature Budget	47
2.6 Conclusions	51
2.7 References	52
3 Receivers for Radio Telescopes	56
3.1 Radio Astronomy Receivers	56
3.2 Cryogenic receivers for VLBI applications	59
3.2.1 Design and Architecture of the Cryogenic Dewar	60
3.2.2 Measurement of the Cryogenic Dewar	63



3.3	12-m Radio Telescope	70
3.3.1	Analysis of the antenna system	71
3.4	Calibration of the VLBI receivers	78
3.4.1	Design of the Ultra-Wideband (UW) Coaxial Probe Antenna	78
3.4.2	Optimization of the coupling factor between the UW-Coaxial probe antenna and the QRFH feed	80
3.4.3	Design of the Ultra-Wideband PCB Probe Antenna	84
3.4.4	Summary	88
3.5	Conclusions	89
3.6	References	90
4	Conclusions	94
5	Appendices	97
5.1	Appendix A: EM evaluation of Radome performance	97
5.2	Appendix B: Evaluation of the down-link budget	100
5.3	Appendix C: Export-Import Grasp to HFSS Transfer procedure	104
6	Personal Bibliography	105



Acknowledgments

Special thanks to my tutor, Prof. Marco Pasian, for being not only an essential mentor but also a friend, and for giving me the opportunity to work on amazing projects relating to the antennas world, becoming totally addicted by these so interesting topics and subjects.

Thanks a lot to my colleagues, who precedes me and who is following me. In particular thanks to Stefano, Riccardo, Andrea, Claudio, Lorenzo and Simone. Thanks also to the other students/workers that year-by-year spend weeks or months in the Lab.

Thanks to Dr. Rémi Rayet, Dr. Steve Rawson and Dr. Thomas Bonhoure from Callisto, for their support and the essential interactions during the several project phases.

Thanks to Dr. Luca Piffer and Dr. Roberto Riccardi from FDS ITALY, for their support and the essential interactions during the several project phases.

Thanks to Dr. Piermario Besso and Dr. Filippo Concaro from ESOC/ESA, for giving me the opportunity to spend 9 months at ESOC. In particular, I want to thank Filippo, I really tried to learn as much as possible from his expertise.



Acronyms and Abbreviations

SNOWBEAR - Svalbard grouNd statiOn for Wide Band Earth observation dAta Re-
ception

GS - Ground Station

ESOC - European Space Operations Centre

ESA - European Space Agency

VLBI - Very Long Baseline Interferometry

LNA - Low Noise Amplifier

FEM - Finite Elements Method

PO - Physical Optics

EM - Electromagnetic

IFR - Induced Field Ratio

ANARESAT - Australian National Antarctic Research Expeditions Satellite

NGR - Next Generation Radar

NWS - National Weather Service

NOAA - National Oceanic and Atmospheric Administration

RF - Radio Frequency

JPSS - Joint Polar Satellite System

Metop-SG - Meteorological Operational Satellites-Second Generation

NASA - National Aeronautics and Space Administration

EUMETSAT - European Organisation for the Exploitation of Meteorological Satel-
lites

SvalSat - Svalbard Satellite Station

MLR - Multi Layer

MSF - Metal Space Frame

TE - Transversal Electric

TM - Transversal Magnetic

LEO - Low Earth Orbit

MOM - Method of Moments

CPO - Co-polarization

XPO - Cross-polarization

ΔG - Gain reduction

BSE - Bore-Sight Error



SLL - Side-Lobe Level
XPD - Cross-Polar Discrimination
NT - Noise Temperature
CD - Cumulative Distribution
SNR - Signal to Noise Ratio
SATCOM - Satellite Communication
 G/T_{SYS} - Gain over System Temperature
FOM - Figure OF Merit
 T_{CMB} - Noise Temperature of the cosmic background
 T_{ATM} - Noise Temperature of the atmosphere
 T_{RAD} - Noise Temperature of the Radome
 T_{ANT} - Noise Temperature of the antenna
 T_{GND} - Noise Temperature of the ground
 T_{FEED} - Noise Temperature of the feed
 T_{LNA} - Noise Temperature of the LNA
OMT - Orthomode Transducer
FAST - Five hundred meter Aperture Spherical Telescope
VLA - Very Large Array
ATA - Allen Telescope Array
ATCA - Australia Telescope Compact Array
SRT - Sardinia Radio Telescope
SKA - Square Kilometre Array
VLBA - Very Long Baseline Array
NRAO - National Radio Astronomy Observatory
AUI - Associated Universities, Inc.
NSF - National Science Foundation
QRFH - Quadruple-Ridged Flared Horn
CALTECH - California Institute of Technology
UV - Ultra-Violet
IR - Infrared
LNF - Low Noise Factory
VLBI - Global Observing System (VGOS).
UW - Ultra Wideband
PCB - Printed Circuit Board



IF - Intermediate Frequency

EL - Elevation

NF - Noise Figure

ATC - Air Traffic Control



Preface

The present thesis is organized into two parts which represent the core of this work. The first part, described in Chapter 2, is devoted to the study and analysis of protective structures for reflector antennas and the second part, described in Chapter 3, is devoted to the study and analysis of protective structures for feed antennas. The division of the thesis into four chapters is as follow.

Chapter 1 provides the aims and motivations of this work, highlighting a general overview of the structures used to protect feed and reflector antennas. In particular, it will be provided a description of the two key projects on which this thesis is focused and developed. Taking part in the SNOWBEAR (Svalbard grouNd statiOn for Wide Band Earth observation dAta Reception) project, the first topic concerns the analysis and design of a high frequency Radome for harsh environment, intended to be installed in Polar Regions and necessary to protect a 6.4-m Ground Station (GS). This work has been carried out in cooperation with the European Space Operations Centre (ESOC) of the European Space Agency (ESA) and FDS ITALY S.r.l., an Italian company with experience in the design and production of Radomes. The second topic concerns the analysis and design of a compact wideband cryogenic Dewar intended to provide the cryogenic cooling and protection of the feed enclosed. The cryogenic receiver, characterized by the feed and the Dewar, will be installed on a 12-m radio telescope, located in Hobart (Tasmania), for Very Long-Baseline Interferometry (VLBI) applications. This work has been addressed with the cooperation of the French company CALLISTO, which has over 20 years' experience producing cryogenic Low Noise Amplifiers for satellite ground stations.

Chapter 2 addresses the Radome structures, which are used to provide a protection of the antenna reflectors against the external environments. This chapter starts with a description of the typical Radomes installed at Polar latitudes, by identifying the best typology for these kind of applications. They will be described the principal parameters and properties used to evaluate the Radomes, providing both theoretical and practical results. Thereafter it will be described the architecture of the SNOWBEAR system, providing the electromagnetic model designed to have a first theoretical assessment on the antenna system performance. Finally, the first measurements to evaluate the radiation performances of the system with and without the Radome will be presented.



Chapter 3 addresses the cryogenic Dewars, which are used to bring the receiver front-end (feed antenna and Low-Noise-Amplifiers (LNAs)) at cryogenic temperatures, and provide its protection against the external agents at once. This chapter starts with a general description of the receivers used in the field of the Radio Astronomy, with a particular emphasis dedicated to the cryogenic receivers. In particular it will be propose a detailed description of the analysis carried out and related to the cryogenic Dewar. Thereafter, it will be introduced the architecture and the analysis of the 12-m Radio Telescope on which the cryogenic Dewar is currently installed. In particular, the study will be focused on the impact, due to the presence of the Dewar structure around the feed, on the performance of the whole antenna system. Finally, the issue about the calibration of the receiver has been considered by means the study and development of two different probe antennas, necessary to inject the calibration signals with the receiver, will be presented setting out the advantages and disadvantages for these purposes.

Chapter 4 provides the conclusions of this work, although it is self-explaining, it will focus the attention on the main results achieved during the several activities.

So far as the appendices are concerned and reported in Chapter 5. Appendix A discusses the electromagnetic (EM) evaluation of the Radome performance, describing in detail the principal parameters typically adopted as the scattering parameters and the Induced Field Ratio (IFR). Appendix B discusses the evaluation of the down-link budget, describing step-by-step the parameters and the formulations adopted to provide a comprehensive analysis of the down-link chain. Appendix C discusses the Export Import GRASP to HFSS Transfer procedure (EIGHT-procedure) developed to export the radiation pattern of the feed simulated by HFSS (FEM method), and to import it in the GRASP (PO method) tool in order to illuminate the antenna system.

Finally, Chapter 5 provides the personal bibliography of the author.

To the attention of the reader: the exact materials, stratifications, geometries, and fabrication processes are usually company proprietary information. In particular, this is referred to the project in cooperation with FDS ITALY S.r.l. (discussed in Chapter 2) and to the project in cooperation with Callisto (discussed in Chapter 3).





1 Introduction

Reflector and feed antennas often require the use of suitable structures to be protected from the external conditions in order that the electromagnetic performance of the antennas remain unchanged regardless of what happens outside. This represents a clear advantage both in terms of the economical and designing point of view, and nowadays, the requests of structures able to provide high electrical and mechanical performance in the same time, is constantly increasing. Unfortunately, these two properties are almost always mutually exclusive and therefore the search of a smart and feasible compromise represents practically always the best solution. In particular, the investigation of structures electrically transparent is fundamental in order to do not cause several negative effects for the operating frequencies like: strong transmission losses, beam-width changes, antenna noise temperature increments, polarization distortion, radiation pattern distortion, bore-sight error. At the same time, structures mechanically compact and resistant represent the key factors to take into account during the entire development and design phase, in order to guarantee a high degree of protection.

The reflector antennas generally require the use of opportune structures (i.e. Radomes) to provide a protection, above all against the environmental conditions and improving the system availability. For instance a strong wind can cause vibrations and movements of a reflector antenna, with the consequent misalignment respect to predefined pointing direction. Otherwise, an accumulation of rain water, snow or ice may cause a surface degradation of the reflector/s with high electrical losses, while a high rainfall intensity entails an erosion and a rapid wear of the reflectors with consequent high repairing costs. Furthermore, the lightning storms can cause a strong impact on the electric properties of the RF systems and the impact may damage the structure of the reflectors. As example, in Figure 1.1 a photo of the Australian National Antarctic Research Expeditions Satellite (ANARESAT) Radome is shown, which protects the ground station from the harsh Antarctic weather during a snowstorm.



Figure 1.1: Photo of the ANARESAT Radome installed at Casey Station, located Antarctica (Photo credits of G. Snow).

Further example is shown in Figure 1.2, in which it is reported a “fake” photo (dissemination purposes) of a Radome that provides a protection of the antenna enclosed against an incoming supercell thunderstorm. As possible to imagine, in both cases just mentioned the absence of the Radome would entails strong damages on the reflectors antenna surrounded. Moreover, beyond to provide a protection against the external weather conditions, other services can be proffered. A protection for the personnel devoted to the maintenance and installation is necessary, especially in locations characterized by harsh weather conditions, such as extremes temperatures, blowing sand, salt spray, and freezing rain. Finally, the structures concerned are also very effective in concealing the type of electronics and mechanicals equipment inside the dome. In Figure 1.3 is shown a picture of the Westford Radio Telescope by two perspectives, inside and outside of a 20 meters Radome used to provide an adequate protection of the reflectors enclosed against the typical cold and snowy winters of Massachusetts. Examples of L-band Radomes typically used in Air Traffic Control (ATC) and military SATCOM applications are reported in Figure 1.4 and Figure 1.5 respectively.



Figure 1.2: Photo of the Next-Generation Radar (NEXRAD) Radar, also known as Weather Surveillance Radar, operated by the National Weather Service (NWS) (agency of the National Oceanic and Atmospheric Administration (NOAA)). (Fake photo created by Photoshop).

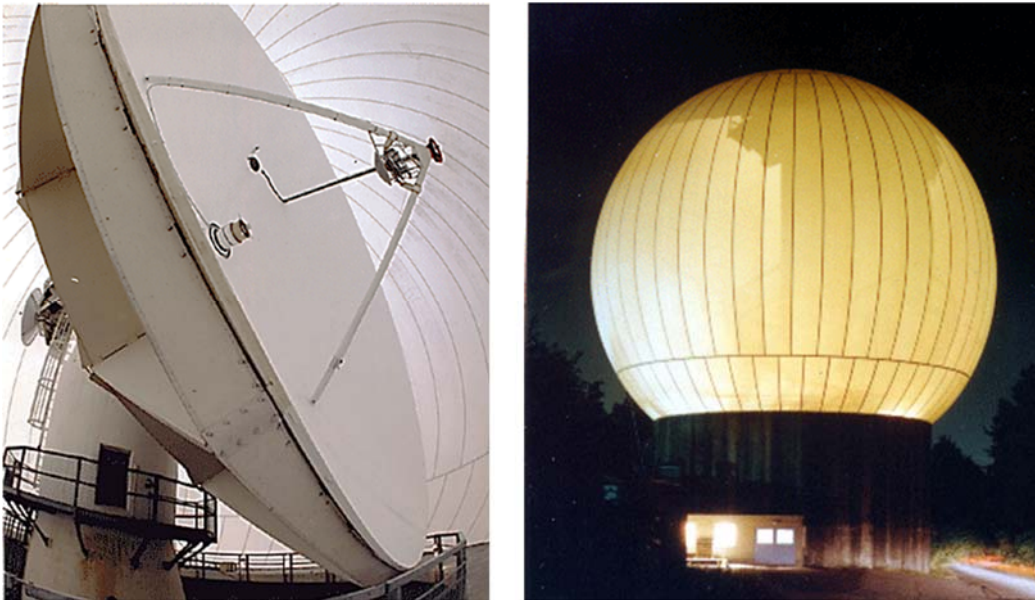


Figure 1.3: Photo of the Westford Radio Telescope. 18.3 meters radio telescope surrounded by a 28 meters Radome. (On the left) internal perspective. (On the right) external perspective. (Photo credits of MIT Haystack Observatory).



Figure 1.4: Photo of a 11.8 meters ATC (air traffic control) Radome. (Photo credits of FDS ITALY S.r.l.).

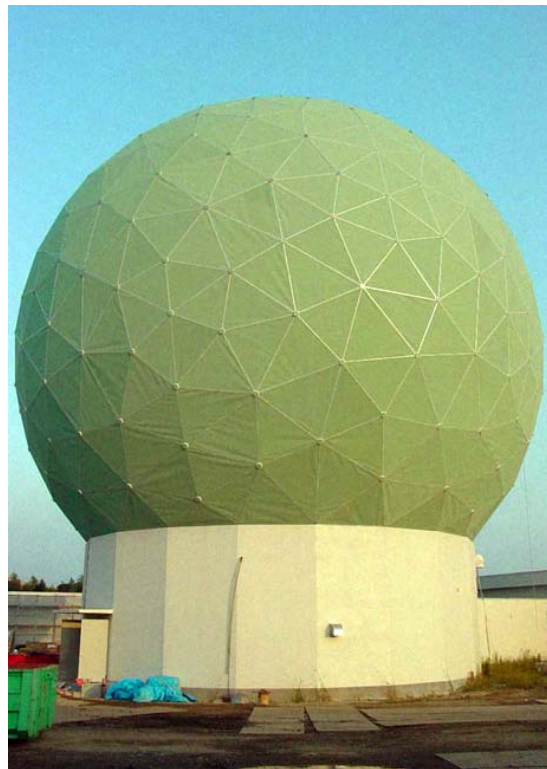


Figure 1.5: Photo of a 26 meters Metal Space Frame Radome for Military SATCOM application. (Photo credits of L-3 ESSCO).



The feed antennas also require the use of protective structures (i.e. Dewars) to minimize the influence of the external environmental influences. For example, they are useful to avoid the moisture condensation and its possible infiltrations inside the feed (i.e., when it is directly installed outside, as it happens for prime focus or Cassegrain/Gregorian antenna configurations), otherwise possible infiltrations inside the other Radio Frequency (RF) systems (i.e., when the feed is installed inside the ground station or radio telescope, as it happens for Nasmyth–Cassegrain and beam waveguide antenna configurations). These situations are very important to take into consideration, because they can cause a total degradation of the whole antenna system, in fact the radiation pattern can be distorted and the transmitted/received signals can be seriously attenuated. Moreover, in some cases, if the moisture freezes, serious hardship may occur with consequent significant economic damage. Furthermore, they prevent that the solar radiation comes directly into the feed causing a strong increasing of the noise temperature. Therefore, as far as feasible, it is clear that these structures have to be resistant to several factors such as rain, wind, dust, hail, ultraviolet radiation, and even birds attack in some cases! These structures are very often used to realize a thermal interface between the inner part, where the feed antenna is normally installed, and the external environment. This approach is required when the receiver has to be cryogenically cooled, because it is essential to use a structure completely insulated. In this way it is possible to realize a strong temperature gradient between the outer room temperature (typically at 25°C) and the inner cryogenic temperature (around -193°C). This approach, as it will be addressed in the Chapter 3, is used to reduce the noise temperature introduced by the receiver itself by cooling to low temperatures not only the active stage, in particular the LNA, but even the feed antenna, and therefore reducing its unacceptable ohmic losses at higher frequencies. As example, in Figure 1.6 a photo of the cryogenic Dewar during the installation phase on a 12-m parabolic reflector, placed in Hobart (Tasmanian), is shown. In this particular case, the Dewar protects the feed enclosed from the external agents and provides the cryogenic cooling. Another example of this kind of structures, used generally for satellite missions where link margins are critical (i.e., for Deep Space Missions), is shown in Figure 1.7. Respect to the Dewar presented and discussed in this thesis, the inner cryogenic temperature used in these structures is 15 K (-258 °C).



Figure 1.6: Photo of the cryogenic Dewar (highlighted in the box on the right) installed on a 12-m parabolic reflector placed in Hobart (Tasmania). Photo credits of Callisto.



Figure 1.7: (On the left) photo of the cryogenic Dewar (developed by Callisto) used for Deep Space Missions. (On the right) photo of the Cebrenros station (DSA 2). Photo credits of Callisto/ESA.





2 Radomes for Ground Stations in Polar Regions

In the last years, several satellite missions devoted to the Earth Exploration Service have been designed to operate at high frequencies to provide high bit-rate data capture about the global environment and thereby avoiding the congested lower bands like the S- and X-band. Joint Polar Satellite System-1 (JPSS-1) [1] and Meteorological Operational Satellites Second-Generation (Metop-SG) [2] represent the first candidates for these future satellites generation. JPSS-1, planned by the cooperation of National Aeronautics and Space Administration (NASA) and the National Oceanic and Atmospheric Administration (NOAA), is scheduled to be launched on 10th of November 2017 at 1:47 a.m. PST, from Vandenberg Air Force Base in California. Concerning Metop-SG, which is planned by the cooperation of the European Space Agency (ESA) and the European Organization for the Exploitation of Meteorological Satellites (EUMETSAT), the first launch will be expected in 2021. Another determinant key feature for these missions regards the exploitation of polar orbits to maximize the satellite passes hence the data return, and this aspect entails the installation of the GSs at polar latitudes. The Svalbard Satellite Station (Figure 2.1 and Figure 2.2) represents one of the best geographical position for these purposes, it is located in the Svalbard archipelago and it is currently providing satellite services up to the X-band using reflector antennas up to 13 meters. However, strong winds, low temperatures, precipitations and periods of frost make these places a harsh reality for the electronics and telecommunications system. For this reason the GSs require the use of Radomes structures to protect the antennas enclosed.

A Radome is a structure designed to protect an antenna from environmental conditions such as wind, rain, snow, ice, blowing sand, fungus, corrosion, ultraviolet rays, and wide temperature fluctuations [3]. The Radome has to be RF transparent in order to have a minimum impact on the electrical performance of the enclosed antenna but must also has high mechanical strength properties. Unfortunately, these properties are often mutually exclusive and the best solution is to find out a clever compromise between them. Furthermore, besides the electrical and mechanical requirements, on the basis of the designed application additional aspects like installation, maintenance, and cost have to be considered for the proper selection of the Radome.



Figure 2.1: Aerial photo take over the Svalbard Satellite Station (SvalSat). Photo credits of KSAT.



Figure 2.2: Photo of the Svalbard Satellite Station (SvalSat). Photo credits of ESOC.



In order to appraise the extent of the weather conditions that may interest this area, it is fundamental to provide a detailed climate statistics and therefore obtain all the necessary information for the design of an appropriate Radome. A detailed weather analysis, based on 10-years continuous statistics covering the time frame 2005–2015 is reported in [4].

As example, summarizing the weather data collected at the Svalbard Airport station over the timeframe from July 2016 to July 2017, the closest official weather station located at 3.9 km away from Longyearbyen and provided by the Norwegian meteorological institute [5], it is noted that the highest temperature was 14.5 °C (3rd July 2016) and the lowest -23.5 °C (18th March 2017). The highest daily precipitation was 41.7 mm (8th November 2016), the maximum snow depth was 35 cm (24th March 2017), while the strongest daily wind was 24.8 m/s (89.28 km/h) (29th December 2016).



2.1 Large Ground Based Radomes

Among several kind of Radomes typically installed in Arctic regions, the Multi-Layer (MLR) Radomes and the Metal Space Frame Radomes (MSF) are the most common design suitable to protect large antennas reflectors [6,7]. These kind of structure can be distinguished on the basis of two main elements: wall and interconnections. The typical geometry used in the MLR Radomes, based on a random configuration of pentagonal and hexagonal shapes, is shown in Figure 2.3 (on the left). In this case the wall is characterized by a multilayer panel realized by a stack of several layers alternating a layer with high dielectric constant (i.e. E-glass or polyester fiberglass) and a layer with low dielectric constant (i.e. honeycombs or foams). Conversely, the interconnections are characterized by dielectric struts which joint together the adjacent panels with metallic bolts. A photo of this kind of Radome currently installed in Svalbard, in which it is possible to appreciate the sequence of bolts, is presented in Figure 2.4. Concerning the MSF Radomes, the typical geometry used is based on a triangular configuration, as shown in Figure 2.3 (on the right). Here the wall is characterized by a single dielectric layer whereas the interconnections are characterized by metallic struts. Once again a photo of this kind of Radome currently installed in Svalbard is presented in Figure 2.5.

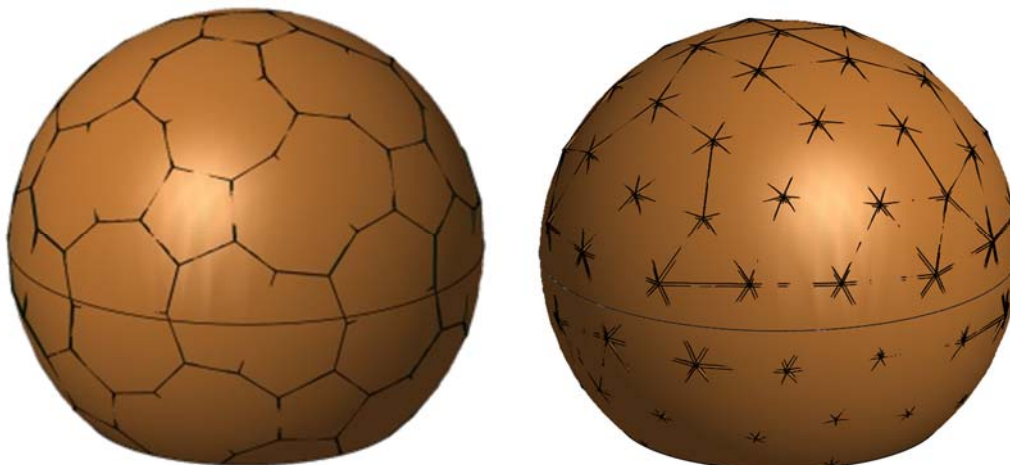


Figure 2.3: Schematic drawing of the typical Large Ground Based Radomes. (on the left) Multi-Layer Radome; (on the right) Metal-Space-Frame Radome.



Figure 2.4: In this photo may be observed a MLR Radome currently installed in Svalbard. It is possible to appreciate the typical hexagonal and pentagonal geometry adopted by the panels, the interconnections characterized by series of bolts and the rope stuck on the surface used to remove the accumulation of snow and ice. (Photo credits of ESOC).



Figure 2.5: In this photo may be observed a MSF Radome currently installed in Svalbard. It is possible to appreciate the typical triangular frames adopted by the interconnections and the wall characterized by a membrane. (Photo credits of ESOC).



From the design point of view, in the MLR Radome the thicknesses of each layer can be varied for optimum performance at discrete operating frequencies, while in the MSF Radomes this opportunity is quite limited. However, this aspect can be mitigated by the fact that these latter present better EM performance over a variety of bands respect to the former. In addition, from the structural point of view, the MLR Radomes present generally a better insulation respect to the other ones, in which, if insulating materials are not used, they deteriorate quickly over the time. Although several pros and cons from the electrical and mechanical point of view, both Radome technologies present the same cost. In fact, a marked difference would entail a predominance from the market point of view.

The electromagnetic response¹ of these Radomes is traditionally approached using two different parameters: the scattering parameters [8,9] for the wall and the IFR [10,11] for the interconnections. From a practical point of view it is advisable that the impact of the wall and interconnections is minimal. However, walls or interconnections with similar responses can have a different impact on the antenna performance according to the Radome geometry and the radiation characteristics of antenna itself (for example, the size or the number of the panels drive the total length of the interconnection and therefore it influences the performance of the Radome). For these reasons, it is good practice to evaluate numerically the response of the antenna protected by the Radome, often using asymptotic methods (e.g., physical optic or ray tracing) [12,13], full-wave methods usually based on integral equations, closed-formula approximations directly built upon the IFR definition.

¹ Detailed formulations adopted to evaluate the EM performance of a Radome may be found in Appendix A.



2.2 MLR Radomes: study and analysis

A detailed EM comparison addressed in [14] has shown a substantial equivalence between MLR and MSF Radomes. This result suggests that a comprehensive evaluation on the compromises between the electromagnetic, mechanical, installation, maintenance, and economical aspects is important to derive the optimum solution. From this point of view the MLR Radomes have several advantages driving the choice as the best structure to protect a large antenna reflector placed in Arctic regions. In the frame of the SNOW-BEAR system, the MLR Radome designed is characterized by a spherical truncated structure with a diameter equal to 11.8 m and truncation of 87%. Being a rigid free-standing and self-supporting structure, it does not require internal positive pressure.

2.2.1 MLR Wall

The MLR wall is composed by a stratification of different high- and low-dielectric-constant layers. Foam is used for the realization of the low-dielectric-constant layers ($\epsilon_r = 1.07$ and $\tan\delta = 0.0014$, [4]), whereas the fiberglass, due to its good compromise between mechanical and electromagnetic properties in addition to its reasonable costs, is adopted to realize the high-dielectric-constant layer ($\epsilon_r = 4.09$ and $\tan\delta = 0.0125$, [4]). The thickness of each layer plays a fundamental role, therefore they have been opportunely designed to provide an excellent compromise between mechanical stiffness and electromagnetic transparency for the frequencies of interest. Given that the stratification is realized by different dielectric layers (i.e., 3 layers for the A-Sandwich), at lower frequencies the resulting structure is almost always robust enough from a mechanical point of view to support the radome weight and external forces (e.g., wind or snow accumulated) for a medium-to-large ground station. Conversely, at higher frequencies the resulting panel is just too thin. Therefore, a possible solution could be working with a larger number of layers, realizing thicknesses at multiples of the half-wavelength. In particular, a stratification based on the layout shown in Figure 2.6 (on the left) has been designed. In this case, two half-wavelength stratifications are separated by an inner low-dielectric-constant layer, achieving the best performance for both the mechanical and electromagnetic aspects, with minimum compromise. Ensuing this aspect, a photo of the designed and realized prototype panel is shown in Figure 2.6 (on the right), in which it is possible to appreciate the different layers.

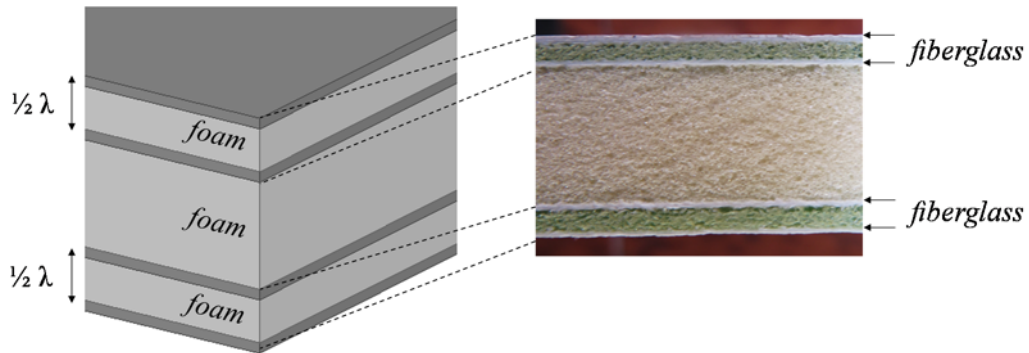


Figure 2.6: MLR wall: (on the left) schematic drawing of the layout; (on the right) photo of a prototype panel.

Exploiting the setup made available by FDS ITALY S.r.l facilities (shown in Figure 2.7), the panel has been measured in the anechoic chamber where two broadband horn antennas are used and opportunely placed at a distance from the panel in such a way the illumination on the panel itself can be approximated by a plane-wave, and the edge effects are minimized.

Figure 2.8 shows the transparency of the panel which has been derived using a differential measurements with a without the panel itself. It can be observed that an excellent agreement has been obtained between simulations and measurements for the frequency band of interest.

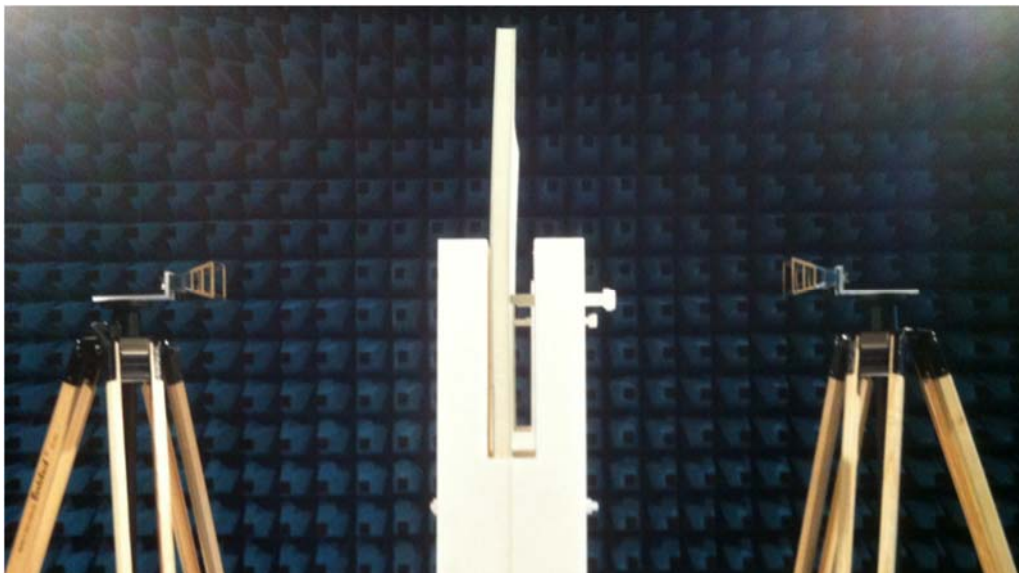


Figure 2.7: Measurement setup implemented for the measurements of the MLR panel.

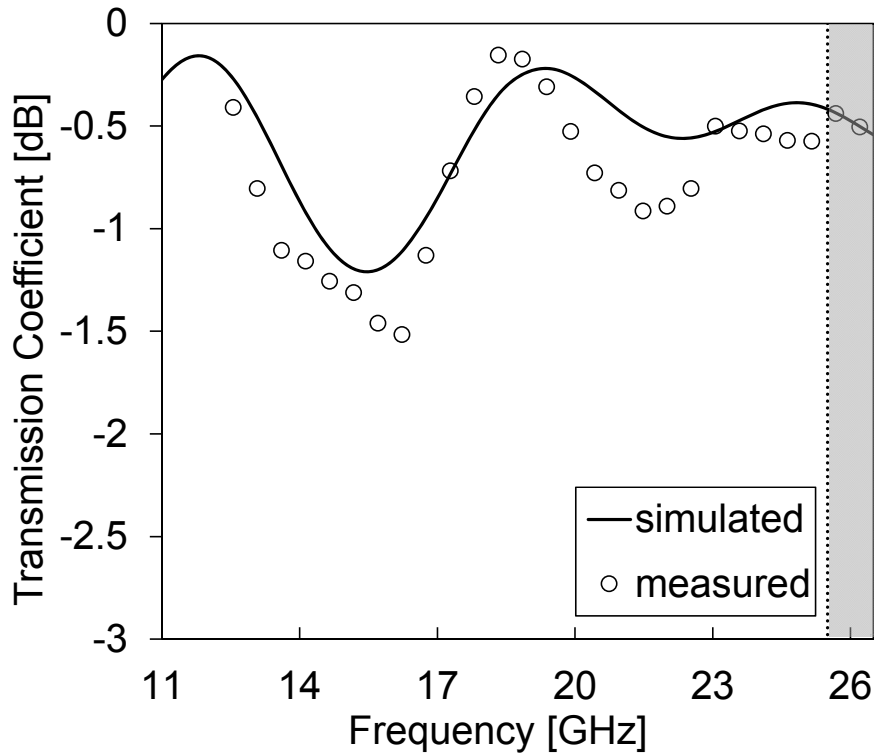


Figure 2.8: Magnitude of the transmission coefficient, calculated by analytical approach, and measured for normal incidence. The frequency band of interest, for the ESA K-band test case, is highlighted with a grey band.

Another feature of the MLR wall concerns the presence of an external thin layer that acts as an external coating around the inner dielectric stratification, allowing the Radome to be protected from the accumulation of rain, snow ice and moisture which can create large electromagnetic losses and noise temperature increase. Moreover, it provides a good protection from fungus, blowing sand, dust and solar radiation. It is clear how important it is the use of material with good hydrophobicity to mitigate this problem. For this reason, an experimental campaign on several samples has been carried out to evaluate the performance of different materials and find out the best solution through a characterization of the outer layers (i.e. gelcoat and paint) in terms of contact angle for a water droplet. A photo of the measurement setup based on the use of a digital microscope is shown in Figure 2.9 (on the left) while the contact angle with a water drop is highlighted with red lines in Figure 2.9 (on the right).



Figure 2.9: Characterization of the hydrophobicity level of the MLR panel. (On the left) Digital microscope used during the experimental measurements; (on the right) microscope image of a water drop on the MLR sample in which the contact angle is highlighted with red lines.

Sample	Contact angle [°]
Gelcoat	91
Gelcoat with hydrophobic treatment	95
Paint	87
Paint with hydrophobic treatment	107

Table 1: Contact angle measured for different MLR samples.

With the aim to provide an adequate statistics, for each sample the contact angles with 5 different bi-distilled water droplets placed in 5 different positions have been measured. The experimental results are reported in Table 1 in terms of average value calculated between the 5 measurements. Although it is well known that a surface can be formally defined hydrophobic if the contact angle exceeds 90 degrees, the experimental data confirms that the normal outer layers used in MLR panels (i.e. gelcoat/paint without treatment), commonly with a shiny and uniform finishing to protect the inner dielectric stratification from external agents can provide a good contact angle, practically very close to hydrophobicity. The extra margin that can be achieved using hydrophobic coating is not considered a viable solution for the test case of the ESA ground station due to concerns related to the possible wear over the years. In fact, it has been demonstrated that the wear due to the aging may entail a degradation on the hydrophobic properties just after a few months of exposure to the environment [15-17]. In addition, on top of all aging agents typical of Polar installations, an additional wear can be given by the



procedure commonly employed to remove snow from the Radome surface, if required. This is based on a rope fixed at the Radome apex and dragged along the surface, causing significant friction on the outer coating. While for normal gelcoat and paint, with a typical thickness in the order of hundreds of microns, this is tolerable, the hydrophobic coatings, with typical thicknesses in the order of tens of microns or even smaller, this can cause a very rapid deterioration.

2.2.2 MLR Interconnection

The MLR interconnections are realized through the overlapping of two adjacent MLR panels, and joined together by metallic screws and nuts, as shown by the schematic drawing and the photo reported in Figure 2.10. The overlapping of the junctions are designed in order to reduce the variation in RF transmission characteristics throughout the Radome surface. The feature to use curved MLR panels of 2 different geometry (hexagonal and pentagonal) with a tuneable size, allows to reduce the total length of the interconnections with a corresponding decreasing of the blocking and scattering. A sample has been manufactured and evaluated in terms of the IFR. The measurement setup, which exploits the same typology of the setup adopted during the measurements of the transparency, is show in Figure 2.11. In this case a laser pointer has been used to align the axis of the interconnection in the centre of the antennas bore-sight, an important requirement to perform the measurement as a function of the polarizations: Transverse Electric - TE and Transverse Magnetic - TM).

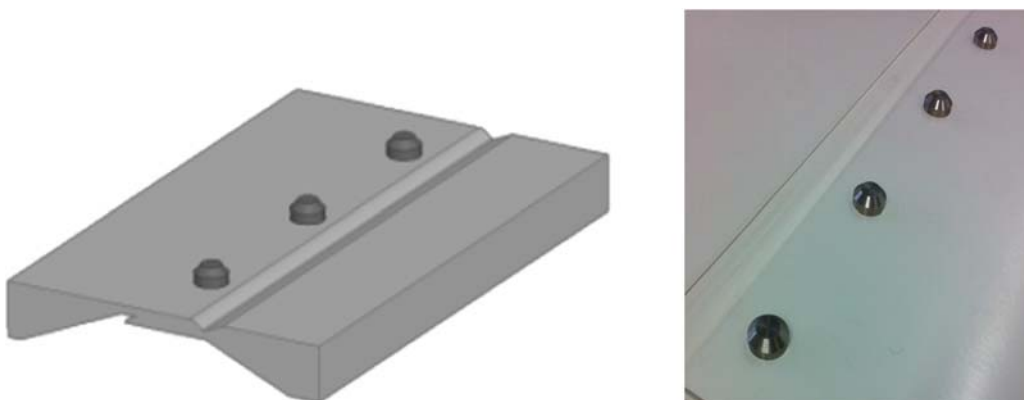


Figure 2.10: MLR interconnection: (on the left) schematic drawing of the interconnection; (on the right) photo of the interconnection.

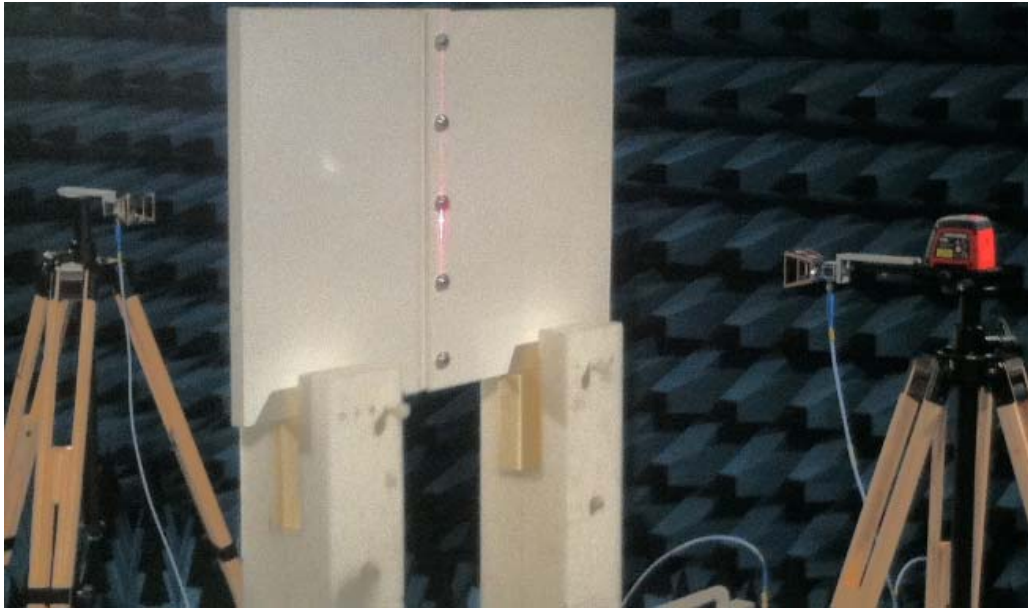


Figure 2.11: Measurement setup implemented for the measurements of the MLR panel.

Incidence Angle [°]	Magnitude Simulated	Magnitude Measured	Phase [°] Simulated	Phase [°] Measured
0	1.45	1.55	134	140
15	1.3	1.55	145	140
30	1.3	1.65	142	142

Table 2: IFR numerical results. TE polarization

Incidence Angle [°]	Magnitude Simulated	Magnitude Measured	Phase [°] Simulated	Phase [°] Measured
0	1.45	1.5	136	140
15	1.2	1.5	155	145
30	1.3	1.6	146	143

Table 3: IFR numerical results. TM polarization.

Table 2 and Table 3 report the numerical results of the IFR evaluated for TE and TM polarization respectively as a function of the incidence angle. It can be observed that for normal incidence comparable results are obtained between simulation and measurement. Conversely, as shown in Figure 2.12, measurement errors due to the finite size of the panel entail a slight deviation from the theoretical values. However, the main contribution conferred from the interconnection concerns the bore-sight of the antenna enclosed and therefore the normal incidence.

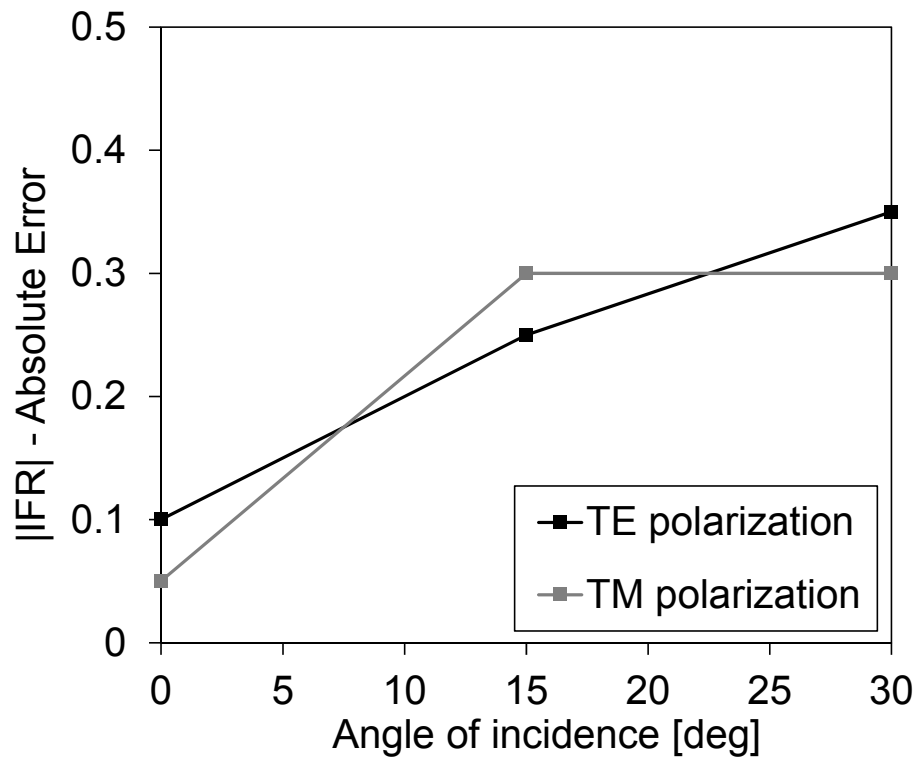


Figure 2.12: Measurement error on the $|IFR|$ (respect to the simulations) due to the finite size of the panel.



2.3 SNOWBEAR System

2.3.1 Antenna Architecture

The SNOWBEAR GS is a dual reflector antenna characterized by a Cassegrain configuration where in its basic shape this type of dual reflector system is composed of an hyperbolic sub-reflector and a parabolic main-reflector. In Figure 2.13 a photo of this antenna, developed and manufactured by MT Mechatronics [18], is shown. The main-reflector is characterized by a 6.4-m parabolic dish with a quadropod structure that supports the 0.8-m sub-reflector, whereas due to the vicinity of the feed respect to the sub-reflector, this latter is designed with a shaped geometry in order to reduce the coupling effects. In this figure it can be easily appreciate the tip in the centre of the dish to reduce the principal reflection. The antenna is design and equipped to receive a down-link channel in S-band (2.2 – 2.3 GHz) and K-band (25.5 – 27 GHz) from Low Earth Orbit (LEO) satellites. The typical orbit for LEO satellites spans from 300 to 1000 km above the ground, and they fly at very high speed (up to 6-7 km/s). Consequently, the visibility of the spacecraft from a point on the ground is limited to a few minutes (10-15 min). To track these satellites the antenna system is equipped with a 3-axis control movement: the azimuth axis to rotate the antenna structure along a vertical axis, the elevation axis to rotate the reflector along a horizontal axis, and the cross-elevation axis to tilt the reflector perpendicularly to the elevation direction. Concerning the feed, this is opportunely positioned in the focus of the sub-reflector and it is characterized by two circular corrugated horns in which the K-band feed.

In Figure 2.14 it is shown a photo taken during the installation phase. It is possible to observe the placement of the Radome around the reflector antenna. In particular, the use of a crane within safety limits, it allowed the minimization of the overall installation times and a reduction of the radar downtime.



Figure 2.13: Photo of the SNWOBEAR antenna system. In the lateral box: corrugated horn antenna used as feed of the reflector antenna and shaped sub-reflector.



Figure 2.14: Photo of the SNWOBEAR GS system installed at SvalSat. Operations phase of the MLR Radome. Photo credits of ESOC.



2.3.2 Antenna Analysis

In order to evaluate accurately the impact of the MLR Radome on the antenna enclosed, the whole system (feed, antenna and Radome) has been modelled and simulated by a mixed combination based on the MOM (Method Of Moments) and PO (Physical Optics) method. The feed system has been simulated by Tiera CHAMP (MOM) [19] while the antenna system (antenna + Radome) has been simulated by Tiera GRASP (PO) [20]. The analysis has been carried out at the centre frequency for the S-Band (2.25 GHz) and K-Band (26.25 GHz). The design of the system simulated, composed by the feed, the dual reflector antenna and the MLR Radome, is sketched in Figure 2.15. As it can be possible to observe, the feed is characterized by the K-band structure (depicted in light grey) which is coaxial to the S-band one (depicted in dark grey), and the Radome has been modelled paying a particular attention to the Radome details. In fact, the wall is modelled as a dome obtained from a truncated sphere and the interconnections are modelled by a dielectric framework whose layout is around 380 meters and characterized by more than 2000 metallic bolts. The whole structure required several days in order to implement accurately all the details, while it took a simulation time around 24 hours. In particular, it has been achieved a high degree of field accuracy equal to -80 dB.

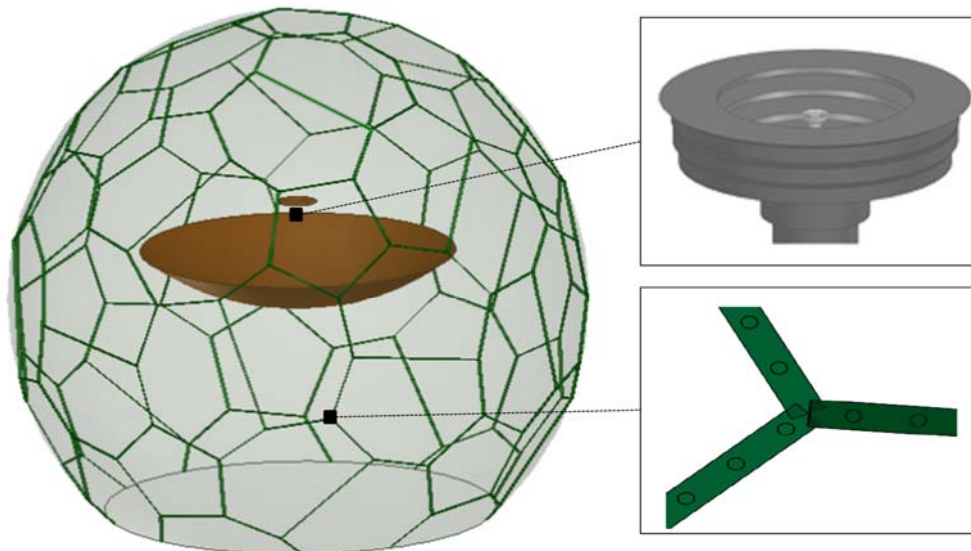


Figure 2.15: Schematic drawing of the SNOWBEAR antenna system modelled by GRASP. In the black box it is shown: (down) a junction point between three MLR interconnections; (up) the feed.



The antenna has been simulated with and without the presence of the Radome in order to appraise the impact on its radiation properties. For the sake of simplicity and since the antenna presents anyhow a circularly symmetric pattern, only the cut $\phi = 0$ deg is reported. In addition, given the particular configuration of the Radome geometry in which the multilayer panels are placed with a certain symmetry and repetition, and given that the antenna placed in centre for the Radome looks for each elevation angle the same portion of the Radome itself, a similar impact at different elevation angles is expected and consequently the radiation pattern reported only for the antenna elevation equal to 0 deg (i.e., at zenith) is representative of the entire system response.

The radiation patterns are evaluated and presented through the co-polarization (cpo) and cross-polarization (xpo) in order to estimate fundamental parameters like the Gain reduction (ΔG), Bore-Sight Error (BSE), Side-Lobe Level (SLL), 1_{dB} Cross-Polar Discrimination (XPD), co-polar 1^{st} null position and 3_{dB} Beam-Width. Figure 2.16 and Figure 2.17 report the radiation patterns for the S-Band (2.25 GHz) and K-Band (26.25 GHz) setting out the comparison the case with and without the Radome.

The numerical results obtained by the simulation of the antenna system are listed in Table 4 and in Table 5. In particular, they show the comparison between the antenna with and without the Radome. As possible to observe, the impact of the Radome is very limited and the worst-case degradation is 0.88 dB achieved in K-Band. This means that through an optimum design it is possible to realize a MLR with high performance at higher frequency as well.

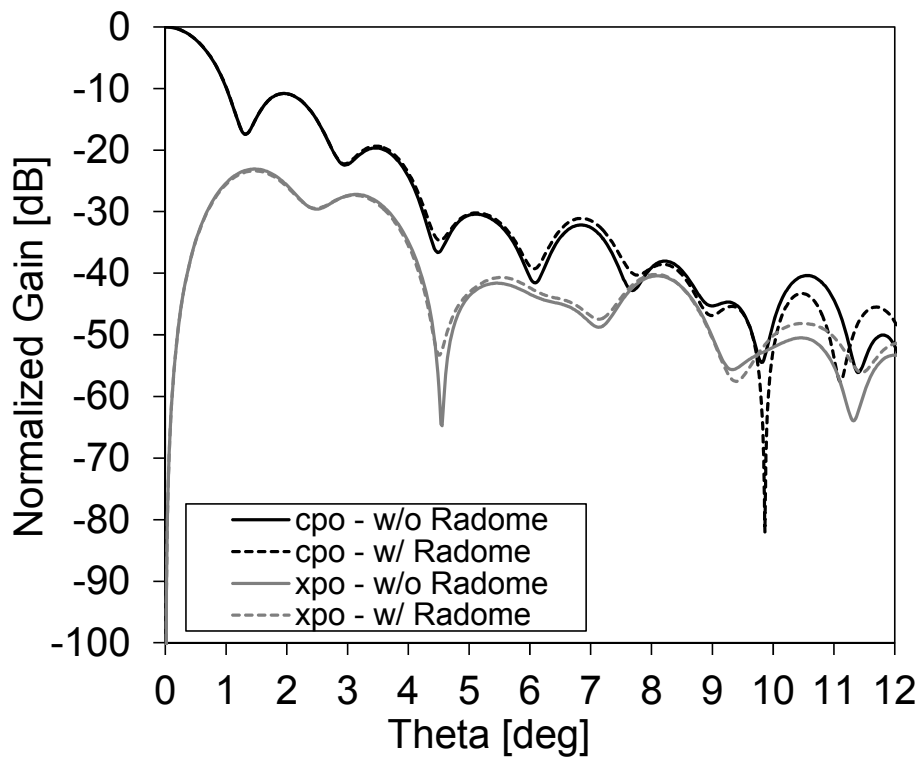


Figure 2.16: Antenna radiation pattern simulated for the S-Band. Comparison with (w/) and without (w/o) the Radome.

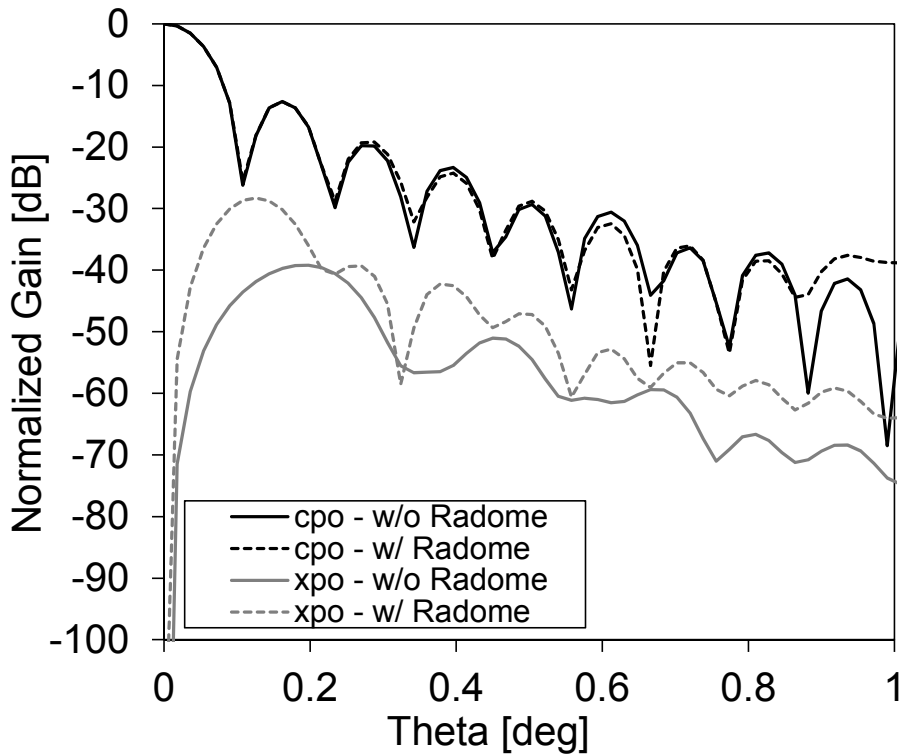


Figure 2.17: Antenna radiation pattern simulated for the K-Band. Comparison with (w/) and without (w/o) the Radome.



Parameter	Without	With	$ \Delta $
Gain [dB]	41.29	41.11	0.18
Bore-Sight Error [deg]	0	0	0
Side-Lobe Level [dB]	-10.9	-10.85	0.05
1_{dB} Cross-Polar Discrimination [dB]	29	29	0
1^{st} Null Position [deg]	1.32	1.34	0.02
3_{dB} Beam-Width[deg]	1.19	1.19	0

Table 4: Antenna system parameters, numerical results calculated for the S-band.

Parameter	Without	With	$ \Delta $
Gain [dB]	63.98	63.1	0.88
Bore-Sight Error [deg]	0	0	0
Side-Lobe Level [dB]	-12.6	-12.62	0.02
1_{dB} Cross-Polar Discrimination [dB]	60	55	5
1^{st} Null Position [deg]	0.112	0.111	0.001
3_{dB} Beam-Width[deg]	0.099	0.099	0

Table 5: Antenna system parameters, numerical results calculated for the K-band.

2.3.3 Preliminary test in Mainz

In order to test the system performance before the installation in Svalbard, the radiation pattern of the antenna has been measured in Mainz, at MT mechatronics [18]. Some photos of the antenna during the first test are shown in Figure 2.18. In particular, the antenna is pointing in the direction of the satellite to perform a measurement of the radiation pattern. The measurements are carried out, both for the K-band and for the S-band, evaluating the Sum- and Delta-channel (Σ and Δ , respectively) of a monopulse auto-tracking system. These channel are generally used in the automatic tracking schemes, in which once the satellite acquisition has been established the tracking continues with no operator intervention. The satellite Alphasat has been used for the K-band test (26.5 GHz), whereas the satellite Xtar has been used for the S-band test (2.3276 GHz). The measured results compared with the simulations, reported in Figure 2.19 and in Figure 2.20, show a very good agreement in particular for the S-band. Conversely, a slight discrepancy may be observed for the Δ -channel measured in K-band (Figure 2.20). This is due to the not perfect circular polarization provided by the antenna satellite causing a contained increment respect to the theoretical one.



Figure 2.18: Some photos of the antenna taken during the test-measurements with satellite.

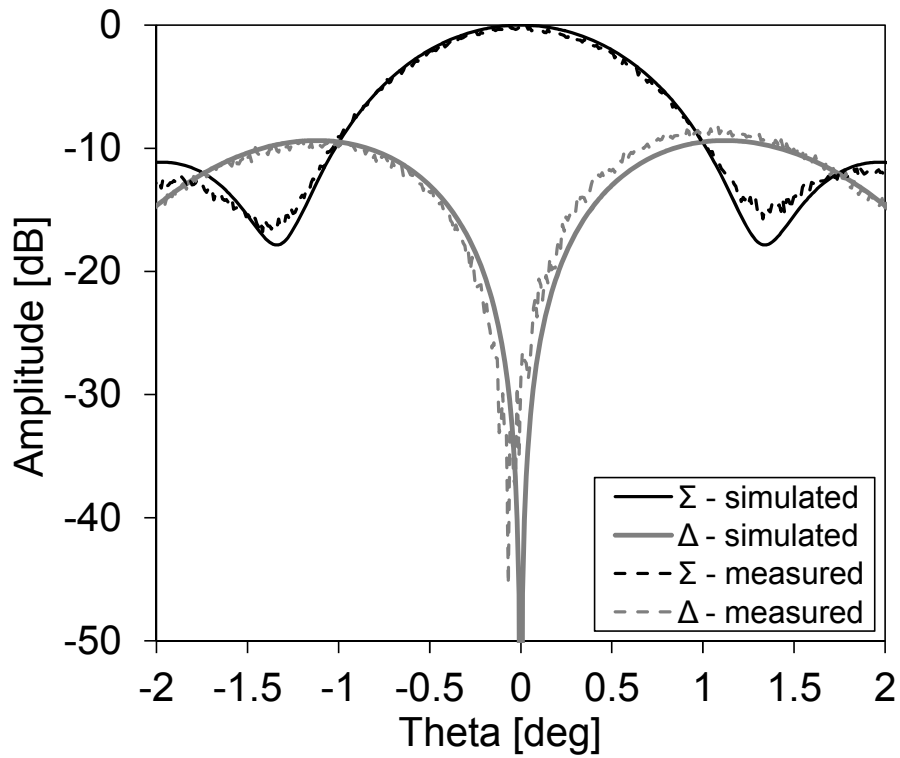


Figure 2.19: Antenna radiation pattern measured in S-band (2.3276 GHz).

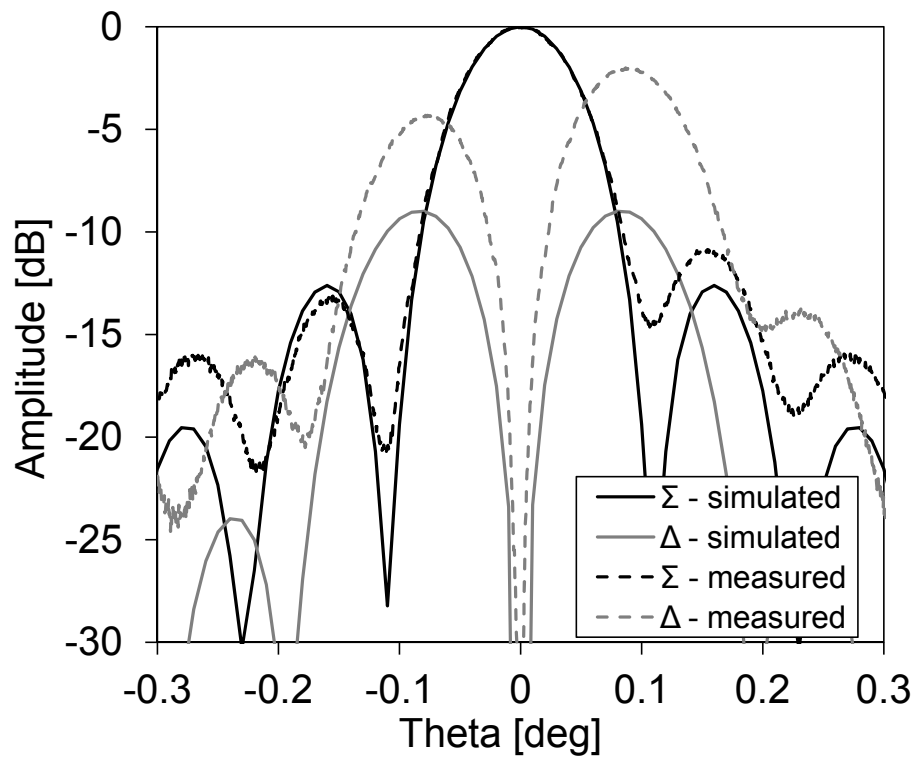


Figure 2.20: Antenna radiation pattern measured in K-band (26.5 GHz).



2.3.4 Preliminary test in Svalbard

The antenna system (antenna + Radome) has been transported by trucks in Svalbard. Figure 2.21 shows the SvalSat, located outside Longyearbyen and approximately 450 meter above sea level. As it possible to observe, the site has an access road suitable for the commercial transportation carriers during installation and for operations personnel. In particular the site is accessible for heavy goods vehicles allowing delivery and installation of large components, including antennas and Radomes.

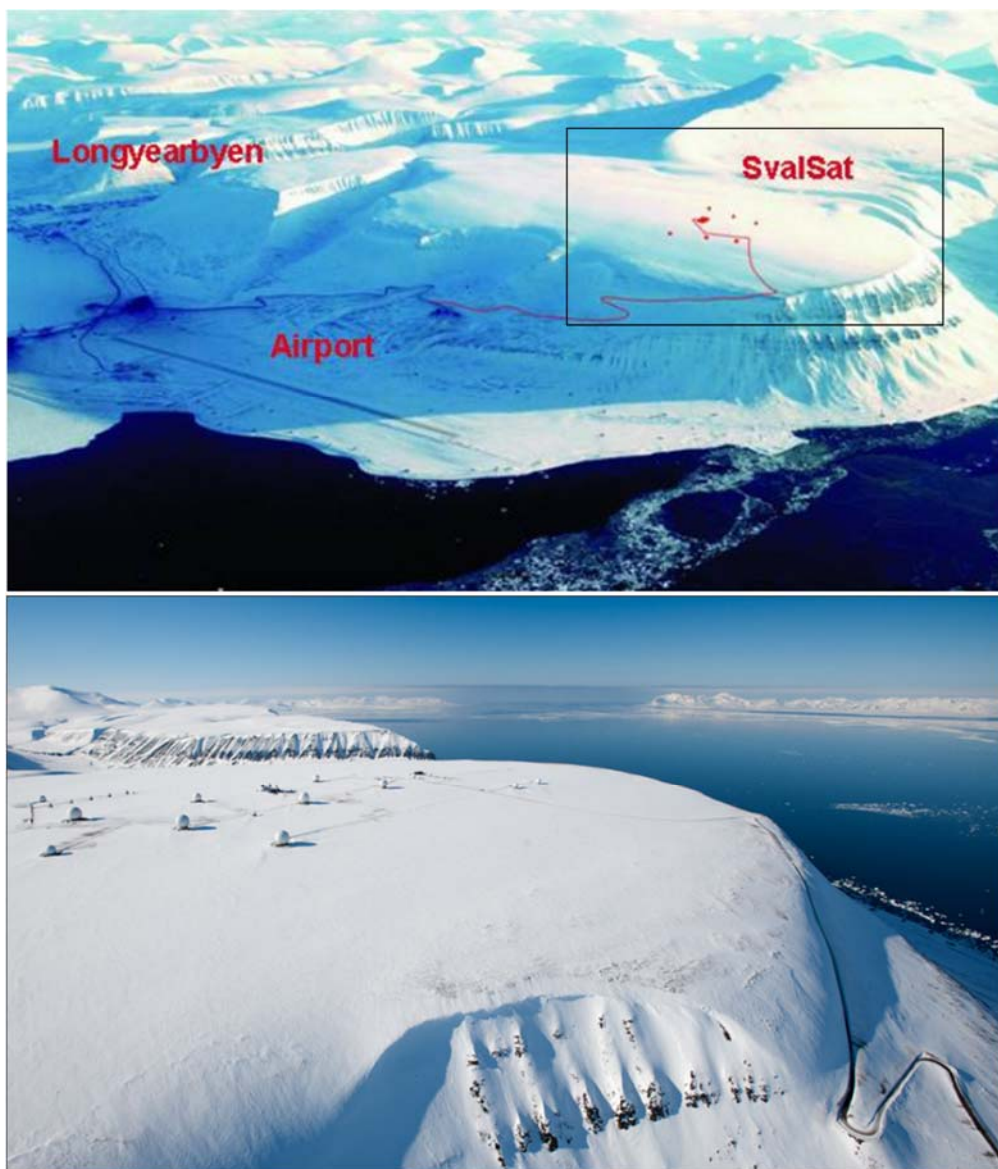


Figure 2.21: Overview of the SvalSat area with main access road. (Photo credits of KSAT).



The radiation patterns with and without the Radome are compared in order to appreciate the impact of this latter on the antenna performance. The results are shown in Figure 2.22.

First of all, in accordance with the simulated results, it can be observed that the presence of the Radome does not affect strongly the radiation characteristics of the antenna introducing significant pattern distortions.

Moreover, it can be noted that both specifications required for the 1st Side-Lobe (<-10 dB, highlighted with black dashed line) level and the Δ -null position (<0.02 deg, highlighted with black dashed-dotted line), are satisfied.

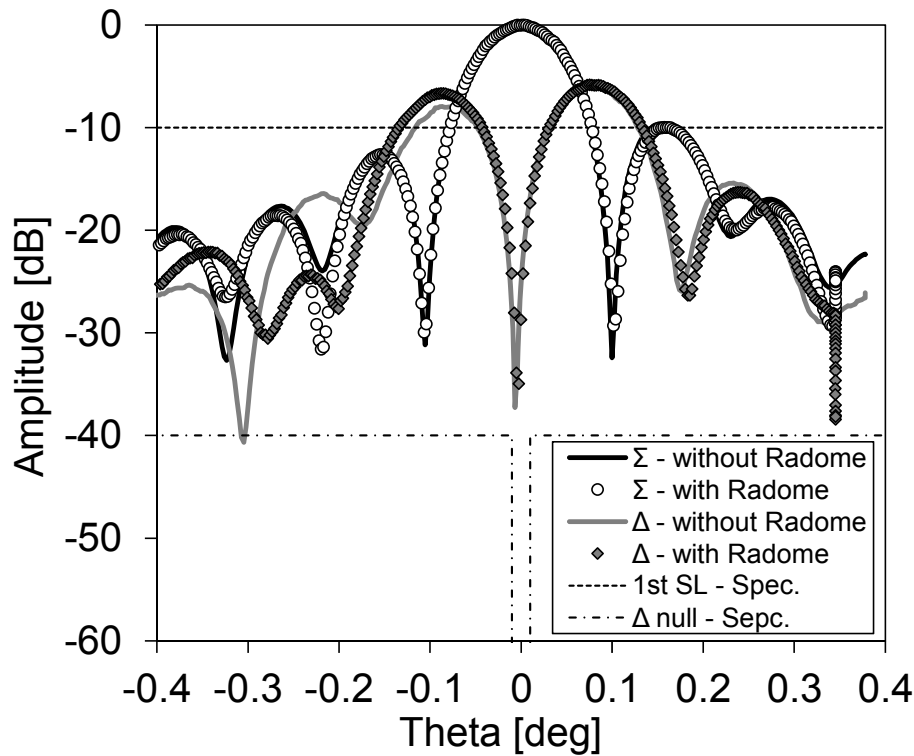


Figure 2.22: Antenna radiation pattern measured in K-band (26.7 GHz). Comparison between without (black and grey solid line) and with (white circle and grey diamond marker) Radome. They are reported also the specifications related to the 1st Side-Lobe (black dashed line) and the Δ -Null (black dashed-dotted line).



2.4 Rainy Conditions

The radio waves propagating through atmosphere experience bumps into several attenuation mechanisms such as absorption, reflection, refraction, scattering, polarization, group delay and fading/scintillation. In particular, the rain is considered to be the major cause of attenuation at frequencies above 10 GHz. In the previous sections, it has been asserted that a Radome should provide a protection to the antenna from the adverse weather conditions such as wind and precipitations and at the same time be as much electromagnetically transparent as possible with low reflections, low transmission loss and minimum distortion of antenna polarization. However a real Radome is not completely transparent and its electromagnetic performances worsen in presence of adverse weather conditions, especially in case of rainy conditions making the Radome wet. As a matter of fact, the accumulation of the rain water on the Radome surface can severely impact the reception of the satellite signal at the Ground Station degrading the quality of the link below an acceptable threshold, and in extreme cases causing a complete loss of the communication link with a consequent impact on the station availability statistics. Moreover, an excerpt from [21] shown in Figure 2.23 shows that the attenuation caused by a wet Radome is extremely high for higher frequencies. For this reason, it is fundamental to assess theoretically the performance of a wet Radome in order to have a first global point of view. Given that it is not possible to predict the way that the rainwater flows on the Radome's surface without experimental measurements, which would be the most reliable method, the only manner is to consider a uniform additional water layer on its surface. Consequently, it is possible to calculate the scattering parameters of the wet Radome (Radome wall + rainwater) exploiting the transmission matrices for plane-wave incidence².

On this basis, Figure 2.24 depicts the model of the wet MLR Radome, characterized by a layer of rainwater with uniform thickness. The implementation of the model and the computation of the scattering parameters, require the knowledge of two fundamental parameters: the thickness and the dielectric properties of the rainwater layer.

² Method based on the formulations used to characterize the wall transparency reported in Appendix A.



Band	Rain rate (mm h ⁻¹)	Two-way attenuation (dB)		Condition	References	
		Standard	Hydrophobic			
20 GHz	05		2.0	Artificial rain	Fenn (1997)	
	10	14.2	2.2	Artificial rain	Chang (1985)	
	10	14.4	3.6	Theory/measured	Chang (1985)	
	20	15.0	4.8	Theory/measured	Chang (1985)	
	40	—	5.0	Theory/measured	Chang (1985)	
	50	16.2	4.2	Artificial rain	Fenn (1997)	
	60	16.4	5.2	Theory/measured	Chang (1985)	
	80	16.8	5.4	Theory/measured	Chang (1985)	
	100	18.0	5.6	Theory/measured	Chang (1985)	
	160		5.8	Theory/measured	Chang (1985)	
	X	10	2.9	—	Theory	Frasier et al. (2013)
10		4.40	2.1	Measured	Frasier et al. (2013)	
10		6.40	3.1	Artificial rain	Bechini et al. (2010)	
10		7.40	1.8	Measured	Trabal et al. (2008)	
25		8.90	4.8–4.9	Measured	Gorgucci et al. (2013)	
40			0.50	Artificial rain	SCAT (2009)	
100			0.60	Artificial rain	SCAT (2009)	
200			0.65	Artificial rain	SCAT (2009)	
300			0.65	Artificial rain	SCAT (2009)	
C		10	4.0	0.50	Theory	Manz et al. (1999)
		15	5.0	0.80	Laboratory and simulations	Effenberger et al. (1986)
	22.1	9.5	3.9 ± 1.5	Laboratory and artificial, clean	Kurri and Huuskonen (2008)	
	22.1	19	4.3 ± 1.4	Laboratory and artificial, dirty	Kurri and Huuskonen (2008)	
	100		3.32	Theory	Merceret and Ward (2002)	
	200		6.63	Theory	Merceret and Ward (2002)	
	300		5.00	Artificial rain	Manz et al. (1999)	
	S	15	2.00	0.3	Laboratory and simulations	Effenberger et al. (1986)
10		1.50	0.3	Theory	Manz et al. (1999)	
20		0.56	0.2	Theory	Merceret and Ward (2002)	
100		2.80	0.98	Theory	Merceret and Ward (2002)	
200		5.60	1.95	Theory	Merceret and Ward (2002)	

Figure 2.23: Typical impact of wet Radome for difference operation frequencies

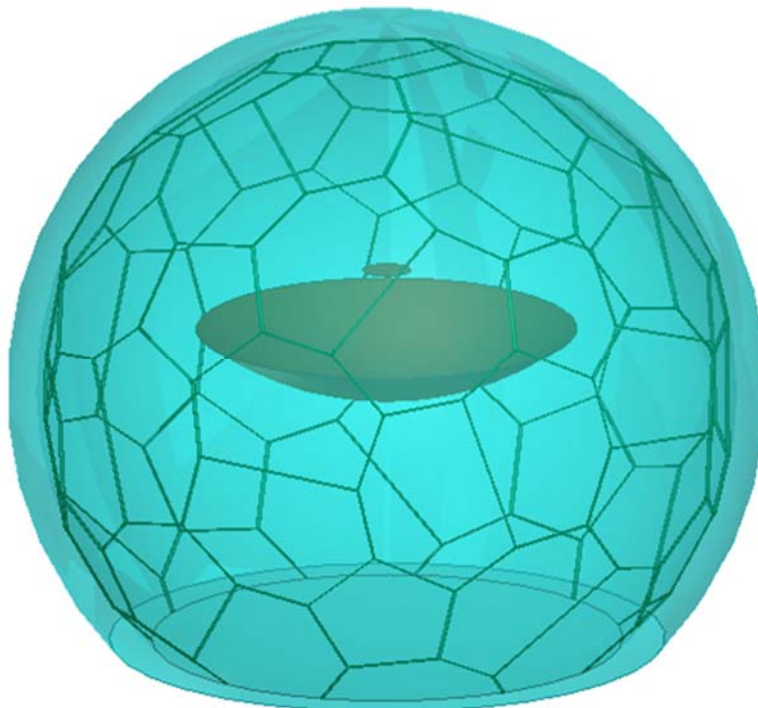


Figure 2.24: Schematic drawing of the wet MLR Radome, characterized by a layer of rainwater with uniform thickness.



Concerning the thickness, the Eq. 1 allows assuming that the formation of the rain-water on the surface of the Radome consists of a thin film of water [22].

$$t = \sqrt[3]{\frac{3\mu_s a R}{2g}} \quad (\text{Eq. 1})$$

Where:

- μ_s is the specific viscosity of the water (mm^2/s);
- a is the radius of the Radome (m);
- R is the rain rate (mm/h);
- g is the gravitational acceleration (m/s^2);
- t is the thickness of the rainwater layer (mm).

It has been anyhow demonstrated [23,24] that the accumulation of pollution, dirt, sand, etc., can change the wettability characteristic of the Radome surface and therefore to cause the formation of rivulet and scattered drops. This means that the theoretical results based on the additional water layer may show some discrepancies compared with the experimental results. In addition, the formation of this water layer can occur in heavy rain conditions and hence in very sporadic situations. For this reason is useful to provide a worst-case study given an idea about the possible performance degradation in the extreme cases. As described by the equation, it is necessary to know as well the viscosity of the water. This because increasing the viscosity of the rain water, the flowing resistance increases and consequently the thickness of the water layer increases in turn. In addition, it is essential to take into account that the kinematic viscosity of the water is temperature-dependent [25]. For example, Figure 2.25 reports the thickness of the rainwater layer calculating as a function of the temperature and for different rainfall intensities.

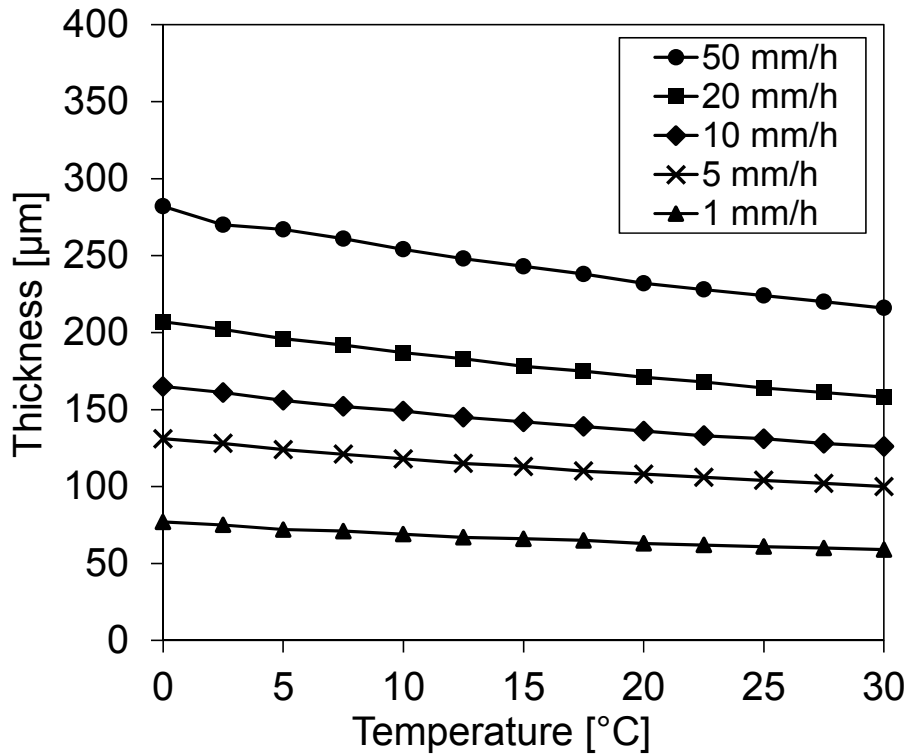


Figure 2.25: Thickness of the water layer as a function of the temperature and the rain intensity.

As anticipated, the rainfall intensity can be characterized through the concept of the rain rate which is classified according to the rate of precipitation [26, 27]:

- Light rain: when the precipitation rate is < 2.5 mm/h.
- Moderate rain: when the precipitation rate is between 2.5 mm/h and 10 mm/h.
- Heavy rain: when the precipitation rate is between 10 mm/h and 50 mm/h.

Beyond the thickness of the rain water layer, it is necessary to know the dielectric properties at 2.25 GHz and 26.25 GHz. Implementing the mathematical Debye model [28,29] which can be described by the Eq. 2 it is possible to extrapolate the real and imaginary part of the complex permittivity for different frequencies.

$$\varepsilon(\omega) = \varepsilon_{\infty} + \frac{\varepsilon_s - \varepsilon_{\infty}}{1 + j\omega\tau} \quad (\text{Eq. 2})$$



Where:

- $\omega = 2\pi f$, is the pulsation (expressed in rad/s);
- ϵ_{∞} is the permittivity at the infinite frequency;
- ϵ_s is the static permittivity;
- τ is the relaxation time of the water (typically expressed in picosecond).

Also in this case, as it can be observed in Figure 2.26 and in Figure 2.27, the temperature plays a fundamental role. For the purposes of this thesis, and due to the low temperatures that characterize the arctic regions, a temperature equal to 0 °C has been considered and the dielectric properties derived are listed in Table 6.

In conclusion, exploiting the Eq. 1 and Eq. 2, it is possible to achieve the essential information to characterized the rain water layer above the Radome and consequently evaluate the impact on the Radome performance.

Figure 2.28 reports the transmission coefficient and the noise temperature (computed for an elevation angle equal to 0 deg and 90 deg) of the Radome, calculated for the S- and K-band, as a function of the rainfall intensity. It can be easily perceived that the high attenuation obtained for the K-band is due to the high losses of the water at these frequencies. In order to achieve a mathematical instrument useful to estimate the Radome losses as a function of the rain rate, a parameter generally measured by the weather stations, a logarithmic fitting has been applied in order to extrapolate the Eq. 3 and Eq. 4, which compute the Radome losses expressed in decibel for the S- and K-band respectively.

Parameter	S-band (2.25 GHz)	K-band (26.25 GHz)
Dielectric Constant	83.18	13.7
Loss Tangent	0.23	1.85

Table 6: Dielectric properties of the rainwater at 2.25 GHz and 26.25 GHz.

$$\text{loss}_{(\text{S-band})} = -0.339 \ln(rr) - 0.5833 \quad (\text{Eq. 3})$$

$$\text{loss}_{(\text{K-band})} = -1.217 \ln(rr) - 4.5052 \quad (\text{Eq. 4})$$

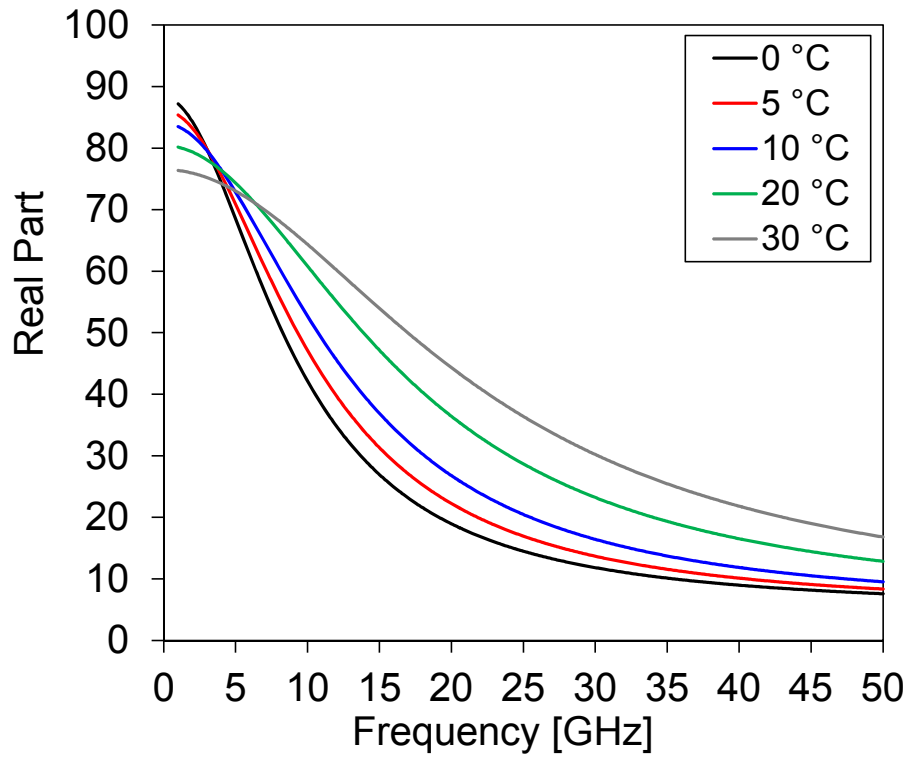


Figure 2.26: Real part of the complex permittivity of the water as a function of the temperature.

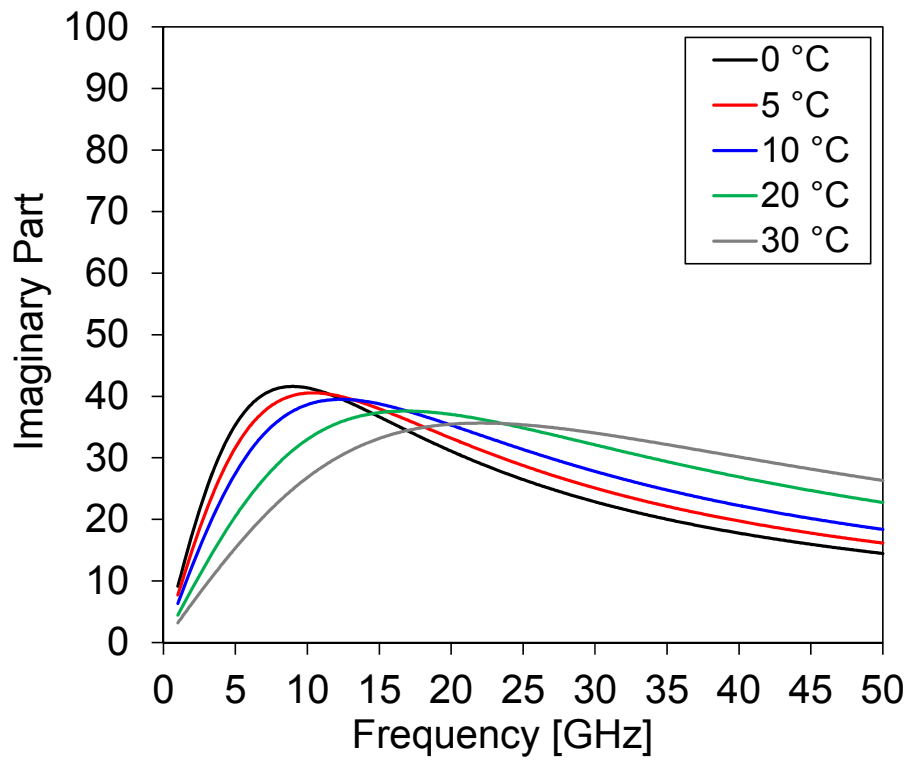


Figure 2.27: Imaginary part of the complex permittivity of the water as a function of the temperature.

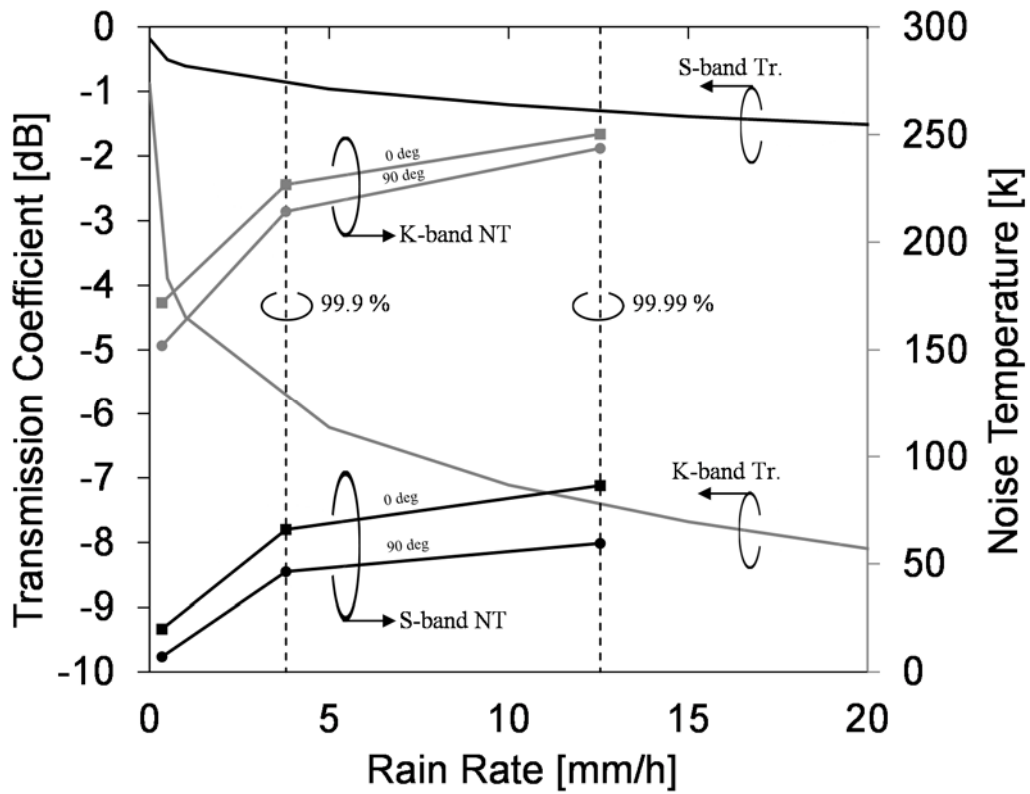


Figure 2.28: Transmission Coefficient (dB) and Noise Temperature [K] of the Radome calculated as a function of the rain rate (mm/h). As reference, two values of Cumulative Distribution (CD) are considered, and highlighted by the vertical dashed black lines.



2.5 Down-Link Performance

2.5.1 Gain over Temperature Budget

A link budget is a statistical tool used to determine if a communications link can be closed, i.e. if the wanted signal can be received in a reliable manner [30]. The ability of a receiver station to achieve high Signal to Noise Ratio (SNR) in a satellite communication (SATCOM) is characterized by the ratio of effective system gain to system noise temperature (G/T_{SYS}), which represents a fundamental Figure Of Merit (FOM) for the design of a GS down-link budget. The estimation of its theoretical value is achieved by calculating separately the two components: the Gain (G) and the System NT (T_{SYS}), which are referred to the same point of the down-link chain. In this section the performance of the SNOWBEAR antenna system with and without the Radome are compared in terms of the G/T_{SYS} , taking into account a complete set of information (as reported in Figure 2.29), in order to provide a dynamic model to use as a benchmark in-service experience.

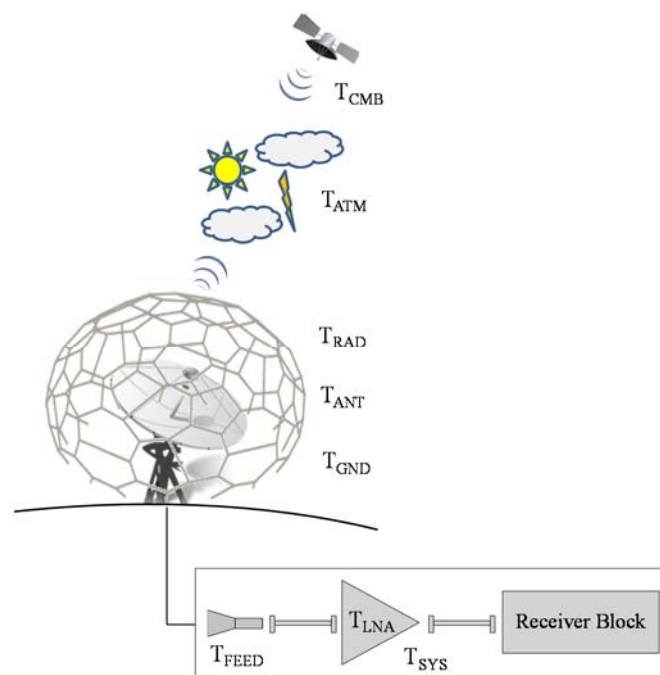


Figure 2.29: Schematic drawing of a typical SATCOM down-link chain. Noise temperature contributions of the T_{SYS} : T_{CMB} (cosmic background), T_{ATM} (atmosphere temperature), T_{RAD} (Radome temperature), T_{ANT} (antenna temperature), T_{GND} (ground temperature), T_{FEED} (feed temperature) and T_{LNA} (low-noise amplifier temperature).



It has been shown in section 2.3.2 the gain of the antenna system simulated both for the S- and K-band. However in the simulation it is not possible to consider all the losses related to the antenna system (i.e. antenna and feed), therefore these additional losses must be taken into account to compute the correct gain referred to the LNA input. In particular, the antenna losses (i.e. surface loss and mirror panel gaps) amount to 0.2 dB and 0.58 dB for the S- and K-band respectively, while the feed losses (i.e. waveguide, filter and Orthomode Transducer (OMT)) amount to 1.2 dB and 1.18 dB for the S- and K-band respectively. The computation of the gain at the LNA input is obtained by reducing the values reported in Table 4 and in Table 5 by the aforementioned feed and antenna losses. Table 7 and Table 8 summarize therefore the values computed for the antenna system without and with Radome as a function of the environmental conditions, which are usually characterized in terms of CD. As expected, the formation of a uniform rainwater layer on top of the Radome, affects the Radome performance by means a reduction of the antenna gain. Conversely, as it can be noted, this aspect does not happen in the scenario “without Radome” because in this case it is assumed that there is no the formation of a rain water layer.

CD (%)	Rain Rate (mm/h)	S-Band (dB)	K-band (dB)	Scenario
25	0	39.89	62.22	Without Radome
90	0	39.89	62.22	Without Radome
99	0.35	39.89	62.22	Without Radome
99.9	3.8	39.89	62.22	Without Radome
99.99	12.55	39.89	62.22	Without Radome

Table 7: Effective gain calculated at the LNA input. Antenna without Radome.

CD (%)	Rain Rate (mm/h)	S-Band (dB)	K-band (dB)	Scenario
25	0	39.71	61.34	With Radome
90	0	39.71	61.34	With Radome
99	0.35	39.66	58.99	With Radome
99.9	3.8	38.86	56.09	With Radome
99.99	12.55	38.45	54.63	With Radome

Table 8: Effective gain calculated at the LNA input. Antenna with Radome.



The T_{SYS} calculations shall take into account several contributions both from the environment (i.e. cosmic background, atmosphere, and ground) and from the electronic system itself (i.e. Radome, antenna, feed, etc.). All of these contributions are combined by the Eq. 5, calculating³ the T_{SYS} of the antenna system without and with Radome

$$T(SYS)_{@LNA} = T(ANT)_{@LNA} + T(FEED)_{@LNA} + T(LNA)_{@LNA} \quad (\text{Eq. 5})$$

As shown in Figure 2.30, depending on the weather conditions three different scenarios are considered:

- CD = 25 % - Clear sky.
- CD = 90 % - Very cloudy sky but without rain.
- CD \geq 99 % - Rainy weather: CD = 99 % (light rain), CD = 99.9 % (moderate rain) and CD = 99.99 % (heavy rain).

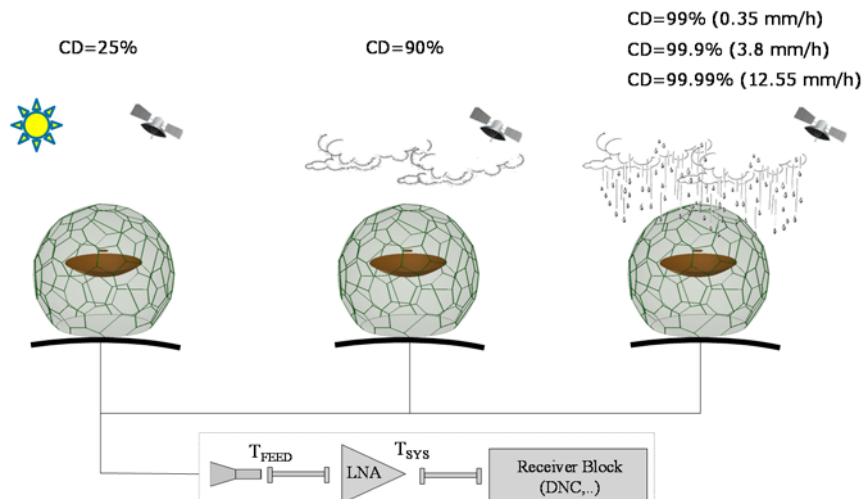


Figure 2.30: Schematic drawing of the GS system. Three different scenarios distinguished on the basis of the weather conditions: CD = 25 % - clear sky (on the left), CD = 90 % - very cloudy sky but without rain (in the centre) and CD \geq 99 % - rainy weather (on the right).

On the basis on these three different environmental conditions, the G/T_{SYS} has been calculated both for the antenna system with and without Radome in order to appraise the performance. The results, as a function of the antenna Elevation (EL), are reported in Figure 2.31 and in Figure 2.32.

³ The procedure to compute the T_{SYS} may be found in the Appendix B

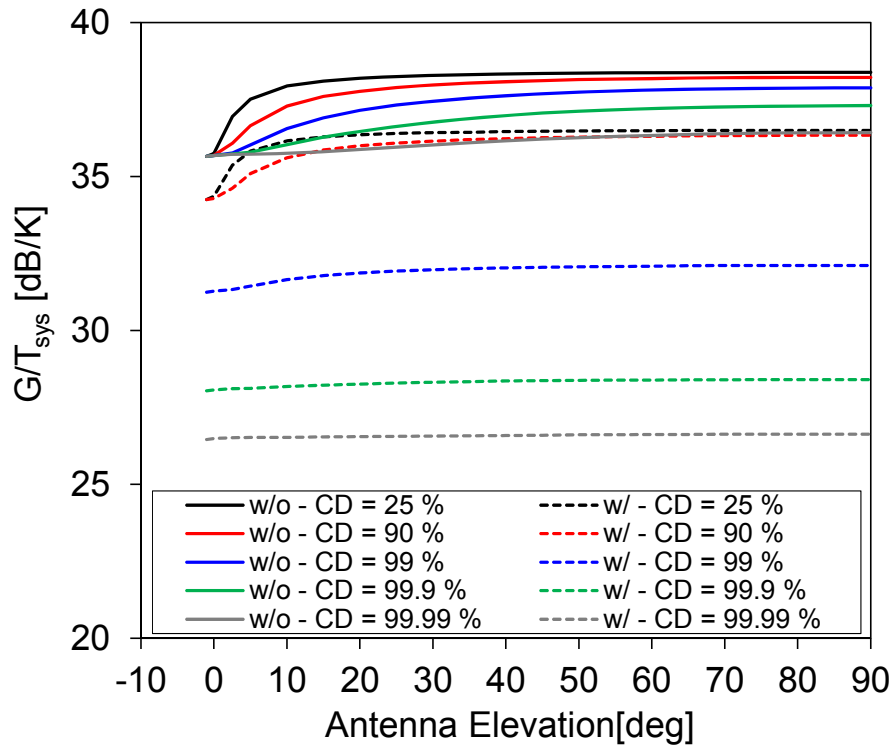


Figure 2.31: Theoretical G/T_{sys} calculated for the K-band as a function of the antenna elevation and the weather condition. Comparison with (w/) and without (w/o) Radome.

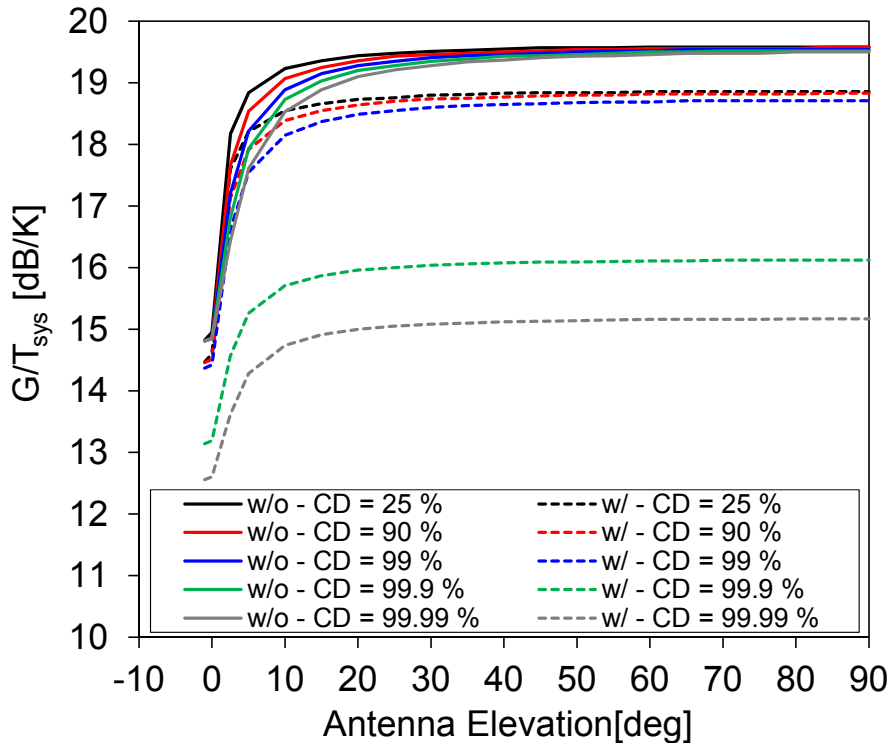


Figure 2.32: Theoretical G/T_{sys} calculated for the S-band as a function of the antenna elevation and the weather condition. Comparison with (w/) and without (w/o) Radome



2.6 Conclusions

In this second chapter, the issue of Large Ground Based Radomes has been addressed. In particular it has been shown a thorough description, analysis and design of a MLR Radome necessary to protect a 6.4-m GS system, installed in Svalbard, against the harsh weather conditions. The architecture of the antenna system (SNOWBEAR) has been modelled and simulated by suitable EM tools, both for the S- and K-band. It has been demonstrated that the Radome does not have a strong impact on the radiation properties of the antenna enclosed, hence confirming this technology as the best for this application. In addition to the radiation performances of the antenna system, also the G/T_{SYS} has been considered evaluating the impact of adverse weather conditions (i.e., rainy conditions). In this case, it has been observed, a strong impact due to the rain on the G/T_{SYS} , which is mainly due to the high losses introduced by the water, in particular for the K-band.



2.7 References

- [1] L. Zhou, M. Divakarla and X. Liu 2, “An Overview of the Joint Polar Satellite System (JPSS) Science Data Product Calibration and Validation,” *Remote Sens.* 2016, 8, 139.
- [2] “The case for EPS/Metop Second-Generation: cost benefit analysis,” EU-METSAT, January 2014.
- [3] J. Kozakoff, *Analysis of Radome-enclosed antennas*, Second edition, Artech Huose, Norwood, U.S.A., 2010.
- [4] A. Martellosio et al., "High-Frequency Radomes for Polar Region Ground Stations: The State of the Art and Novel Developments of Radome Technologies," in *IEEE Antennas and Propagation Magazine*, vol. 59, no. 6, pp. 88-101, Dec. 2017.
- [5] Norwegian meteorological institute, official website:
<https://www.yr.no/place/Norway/Svalbard/Longyearbyen/statistics.html>
- [6] A. Kay, “Electrical design of metal space frame Radomes,” *IEEE Transactions on Antennas and Propagation*, Vol. 13, No. 2, pp. 188– 202, February 1965.
- [7] R. Shavit, A. P. Smolski, E. Michielssen, and R. Mittra, “Scattering analysis of high performance large sandwich Radomes,” *IEEE Transactions on Antennas and Propagation*, Vol. 40, No. 2, pp. 126–133, February 1992.
- [8] R. Sorrentino and G. Bianchi, *Microwave and RF Engineering*, John Wiley & Sons, Chichester, United Kingdon, 2010.
- [9] X.-Q. Sheng and W. Song, *Essentials of Computational Electromagnetics*, John Wiley & Sons – IEEE Press, Chichester, United Kingdom, 2012.
- [10] J. Richmond, “Scattering by a dielectric cylinder of arbitrary cross section shape,” *IEEE Transactions on Antennas and Propagation*, Vol. 13, No. 3, pp. 334–341, March 1965.
- [11] W. Rusch, J. Appel-Hansen, C. Klein, and R. Mittra, “Forward scattering from square cylinders in the resonance region with application to aperture blockage,” *IEEE Transactions on Antennas and Propagation*, Vol. 24, No. 2, pp. 182–189, February 1976.
- [12] S. R. Rengarajan and E. S. Gillespie, “Asymptotic approximations in Radome analysis,” *IEEE Transactions on Antennas and Propagation*, Vol. 36, No. 3, pp. 405–414, March 1988.



- [13] J. H. Kim, H. J. Chun, I. P. Hong, Y. J. Kim, and Y. B. Park, "Analysis of FSS Radomes Based on Physical Optics Method and Ray Tracing Technique," *IEEE Antennas and Wireless Propagation Letters*, Vol. 13, pp. 868–871, 2014.
- [14] A. Martellosio, M. Pasian, L. Perregrini, L. Piffer, R. Riccardi, F. Concaro, and P. Besso, "Electromagnetic Analysis of High Frequency Radomes for Ground Stations in Polar Regions," 2017 11th European Conference on Antennas and Propagation (EuCAP 2017), Paris, France, March 19-24, 2016.
- [15] C. Siller, "Preliminary testing of teflon as a hydrophobic coating for microwave Radomes," *IEEE Transactions on Antennas and Propagation*, Vol. 27, No. 4, pp. 555–557, April 1979.
- [16] R. M. Weigand, "Performance of a water-repellent Radome coating in an airport surveillance radar," *Proceedings of the IEEE*, Vol. 61, No. 8, pp. 1167–1168, August 1973.
- [17] F. J. Dietrich, and D. B. West, "An experimental Radome panel evaluation," *IEEE Transactions on Antennas and Propagation*, Vol. 36, No. 11, pp. 1566–1570, November 1988.
- [18] MT Mechatronics, official website:
<http://www.mt-mechatronics.com/home.html>
- [19] Ticra CHAMP, official website:
<http://www.ticra.com/products/software/champ>
- [20] Ticra GRASP, official website:
<http://www.ticra.com/products/software/grasp>
- [21] J. L. Salazar-Cerreño *et al.*, A Drop Size Distribution (DSD)-Based Model for Evaluating the Performance of Wet Radomes for Dual-Polarized Radars, *Journal of Atmospheric and Oceanic Technology*.
- [22] D. Gibble, Effect of rain on transmission performance of a satellite communication system, *IEEE International Convention Record*, Part VI, IEEE, 52.
- [23] Anderson, I., 1975: Measurements of 20-GHz transmission through a Radome in rain. *IEEE Trans. Antennas Propag.*, 23, 619–622.
- [24] Chang, K.-C., 1985: System performance in rain in a Radome enclosed environment. 1985 IEEE Military Communications Conference: MILCOM '85, Vol. 1, IEEE, 293–299.



- [25] Kestin, J., Sokolov, M., & Wakeham, W. A. (1978). Viscosity of liquid water in the range -8°C to 150°C . [New York]: American Chemical Society and the American Institute of Physics for the National Bureau of Standards.
- [26] Glossary of Meteorology (June 2000). "Rain". American Meteorological Society. Retrieved 2010-01-15.
- [27] Met Office (August 2007). "Fact Sheet No. 3: Water in the Atmosphere" (PDF). Crown Copyright. p. 6. Retrieved 2011-05-12.
- [28] F. Buckley and A. A. Maryott, Tables of dielectric dispersion data for pure liquids and dilute solutions, U.S. Dept. of Commerce, National Bureau of Standards.
- [29] Gabriel, C.: 'Dielectric properties of biological materials, Chapter 3', in 'Handbook of biological effects of electromagnetic field' (CRC Press, Florida, USA, 2006).
- [30] G. Maral and M. Bousquet, Satellite Communications Systems: Systems, Techniques and Technology, 5th Edition, John Wiley & Sons Ltd.
- [31] Centre national d'études spatiales (CNES), official website:
<https://cnes.fr/en>





3 Receivers for Radio Telescopes

3.1 Radio Astronomy Receivers

With the electronic development of the radio-communication and radar system in the years that followed the Second World War, the radio astronomy had a fundamental role in the study of the Universe at radio frequencies. The radio waves emitted by extra-terrestrial sources, whose investigation represents the key issue, are usually collected by radio telescopes which in the microwave region (300MHz – 300 GHz) are practically based on reflector antennas consisting of one or more dishes. Due to the weakness of the astronomical signals coming from faraway sources [1] generally in the order of -100 dBm ÷ -120 dBm, the main dish of the radio telescope is always designed to be very large in terms of wavelength in order to ensure high directivity and large collecting area. In this way, the high sensitivity and resolution achievable allow to proffer an high quality in the radio astronomy observations [2]. Although large antennas for radio astronomical purposes already exist (most notably, the Effelsberg telescope [3], the Sardinia Radio telescope [4], and the Green Bank telescope [5]), the design and realization of large dishes is very complex beyond to show several drawbacks that limit their applicability. For example the main reflector can be strongly deformed by gravity, thermal and wind loads causing a poor surface accuracy and the consequently low antenna efficiency [6]. From the economic and operational point of view, a single large antenna represents a huge investment and a critical single-point failure architecture entails significant risks to the availability of the ground segment. In addition the maximum resolution achievable by the biggest radio telescopes in the world characterized by a single main dish (Five hundred meter Aperture Spherical Telescope (FAST) [7] and Arecibo [8], which are built within natural depression) is not enough to satisfy the continues challenges in the field of the Radio Astronomy Imaging.

All of these limitations can be mitigated exploiting the interferometric techniques in which the signals detected from different radio telescopes are mathematically combined through the Aperture Synthesis technique [9]. In this way, it is possible to enlarge the collecting area of the Radio Telescope without increasing the diameter of the single antenna. Although this strategy has already been implemented for many years (most notably, the VLA - Very Large Array [10], the ATA - Allen Telescope Array [11], and the ATCA - Australia Telescope Compact Array [12]) in which the antennas relatively



close to each other and physically connected to each other by coaxial cable, waveguide or optical fiber, an evolution of this approach consist in the Very Long Baseline Interferometry (VLBI) technique [13,14] in which the antennas are located at distant locations on the Earth surface.

Figure 3.1 shows an example of radio telescope that exploits this mechanism in which depending on the position of each single the antenna, the signal from the Space arrives with a slightly different time on the basis of the different paths. The signals received and recorded are thereafter cross-correlated in order to infer the position of the emitting object. Reaching very large distances between each station it is possible to obtain a superior resolution than the conventional antennas array configurations. In Figure 3.2 it is shown a comparison in terms of the resolution achievable between different radio telescopes. It can be observed that the use of a radio telescope based on one single dish (Medicina, Sardinia Radio Telescope (SRT), Arecibo and FAST), the maximum resolution achievable is greater than 10^{-1} arcmin. Conversely, using a radio telescope based on an array configuration (Square Kilometre Array (SKA) and VLBI) a resolution of about 10^{-5} arcmin can be reached. Although the VLBI technique allows to increase considerably the resolving power of the radio telescope, it nevertheless remains the case that the incoming signal from the astronomical radio source is extremely feeble and much smaller than the noise from the receiver, background and atmosphere. Principally due to the large propagation distance, still constitute a critical point that has to be addressed, and therefore it is very important to differentiate this low level signal from other noise sources.



Figure 3.1: Schematic drawing of the Very Long Baseline Array (VLBA). 10 radio telescopes with a diameter of 25m, covering 8000km from St. Croix, Virgin Islands to Mauna Kea, HI. Image credit: NRAO/AUI/NSF.

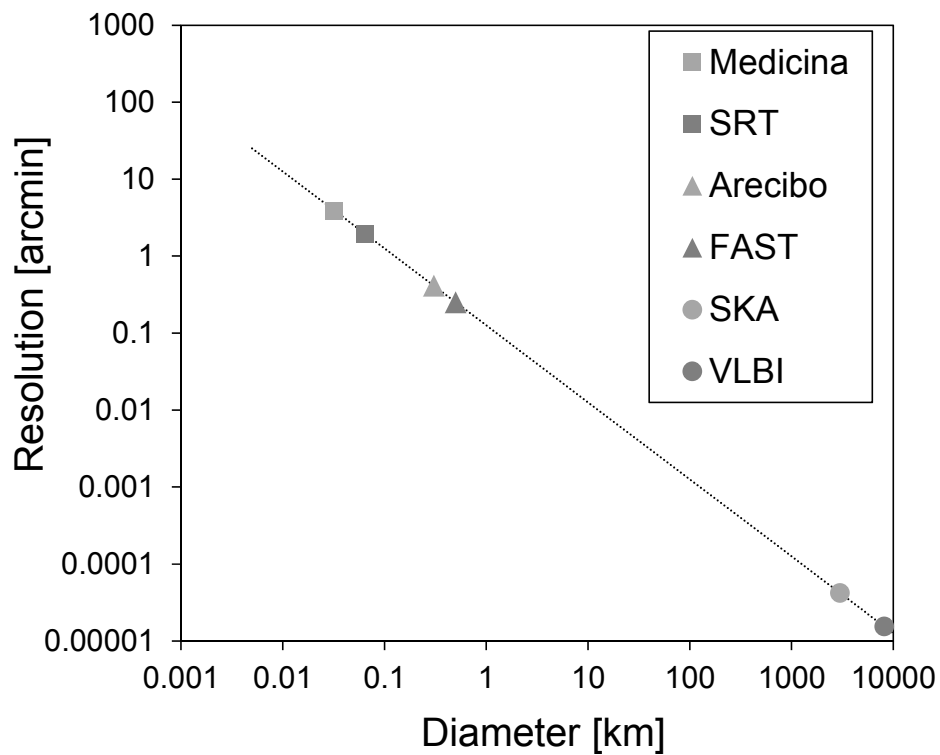


Figure 3.2: Resolutions achievable in the X-band (10 GHz) using different radio telescopes.



3.2 Cryogenic receivers for VLBI applications

The minimization of the receiver noise temperature [15] represents the main challenge to improve the system sensitivity and given that the first amplifier element of the receiver chain contributes the greatest amount of the noise power, the use LNAs [16, 17] at the front-end of the receiver plays a crucial role in determining the overall performance of the system. This concept is therefore essential for this kind of applications. The LNA receives the weak and faint incoming signal and amplifies it to a level strong enough to be detected and processed. Typical requirements for LNA in radio astronomy are noise temperature as low as 50 K [18]. Owing to this critical task of LNA, it generates a lot of noise into the receiver system which can shadow the source signal completely when its temperature rises. At extremely high frequency operation like in C and K bands LNAs require cryogenic condition of operation often around 20 K in order to keep the noise level to the minimum and prevent burnout. Moreover, the opportunity to cryogenically cool also the antenna feed to reduce the unacceptable ohmic losses at higher frequencies represents a smart way to reduce hugely the noise contributions and guarantee better performances. For this reason, the feed is typically surrounded by a Dewar [19] which realizes a thermal interface between the inner part at cryogenic temperature and the outer part at room temperature. For example in Figure 3.3, the part of the Dewar that is subjected to cryogenic temperature is highlighted with light blue lines. Unfortunately, it can be easily understood that the Dewar inevitably affects the radiation properties of the feed enclosed. For this reason, the electromagnetic transparency of the Dewar has to be taken into consideration during the design process meeting a compromise with the thermo-mechanical aspects. In the last years, several structures of this type have been designed and fabricated to be used for radio-astronomical applications including VLBI [20-23].

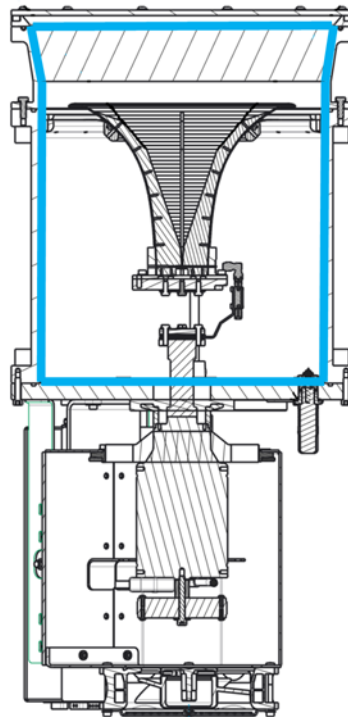


Figure 3.3: Schematic drawing of the cryogenic receiver. The light blue lines highlight the thermal interface between the inner part at cryogenic temperature and the outer part at room temperature. (Callisto design).

3.2.1 Design and Architecture of the Cryogenic Dewar

The cryogenic receiver presented in the frame of this thesis is characterized by two main elements: a wideband feed (2 – 14 GHz) and a Dewar, which are reported in Figure 3.4 with the overall vertical and lateral dimension. The feed, known as Quadruple-Ridged Flared Horn (QRFH) designed by the California Institute of Technology [24], works with an unbalanced configuration by means a dual-linear polarization and therefore it requires two LNAs for each outputs. In addition, it presents a good beam-width stability and small phase centre variation, fundamental requirements for radio astronomy systems. The Dewar, developed in collaboration with the French company Callisto [25], adopts a very compact design and can be divided into a lower and upper section.

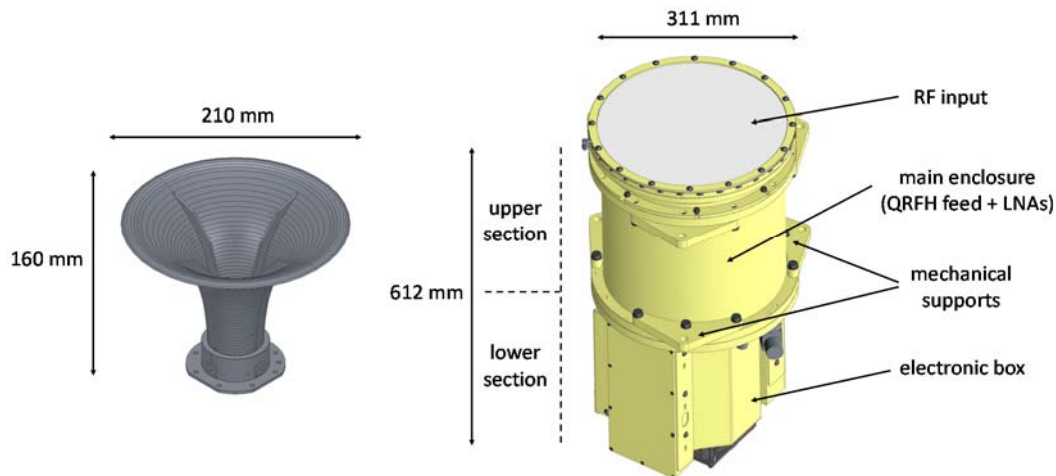


Figure 3.4: Schematic drawing of the cryogenic receiver and the QRFH feed (perspective view). Representation with the overall vertical and lateral dimension. Drawing not to scale.

The lower section is used to enclose the electronic box, which besides to contain the Phase and Noise Calibration system, houses the fan, the cryo-cooler and the Helium compressor. Conversely the upper section consists of the RF input, the main enclosure, and the mechanical supports. These latter are generally used to ensure a precise positioning of the entire system at the correct point of the antenna optics on which the receiver is installed. Within the main enclosure, where the QRFH feed and the LNAs are installed, the under-vacuum conditions are created to allow the cryogenic cooling. Due to the differential pressure between the inner and the outer side of the enclosure, the RF input window has to satisfy stringent mechanical requirements taking into account that is made out of dielectrics materials in order to enhance the microwave transparency. As possible to imagine, the presence of the Dewar above feed aperture entails an impact upon the radiation pattern of the QRFH itself. For this reason, the impact of the Dewar cannot be neglected, and an assessment of the radiation patterns and input matching with and without the Dewar is required. In particular, the attempt to reduce the impact as much as possible over the entire frequency range has been addressed exploring different solutions between the thicknesses/nature of the dielectric layers above the feed aperture and the geometries of the external metallic window. A 3D sketch of the cryogenic receiver, composed by the QRFH feed and the upper section of the Dewar, is shown in Staring through the external metallic structure depicted in transparency, it is possible to observe the block of rigid foam ($\epsilon_r = 1.093$ and $\text{tg}\delta = 0.0038$) (experimental values provided by Callisto) depicted in blue placed above the aperture of the feed. This



block serves to ensure a thermal insulation and, at the same time, it provides a mechanical support against the external pressure for the RF window. Depicted in white, a radome ($\epsilon_r = 2.8$ and $\text{tg}\delta = 0.005$) (experimental values provided by Callisto), is used to provide a protection from weather effects like rain, wind, dusts, hail, Ultra-Violet (UV) radiation, possible birds attack, also provides thermal isolation from the infrared (IR) heat loads coming from the warmer surrounding parts and possible direct solar radiation. The model has been analysed through a full-wave solver (Ansys HFSS) [26], and even if the requirements imposed by the thermal and mechanical constraints are quite stringent, the best solution with minor effects has been found out acting on the length and tilt angle of the slanted metallic wall, highlighted in Figure 3.5 by black dashed profile.

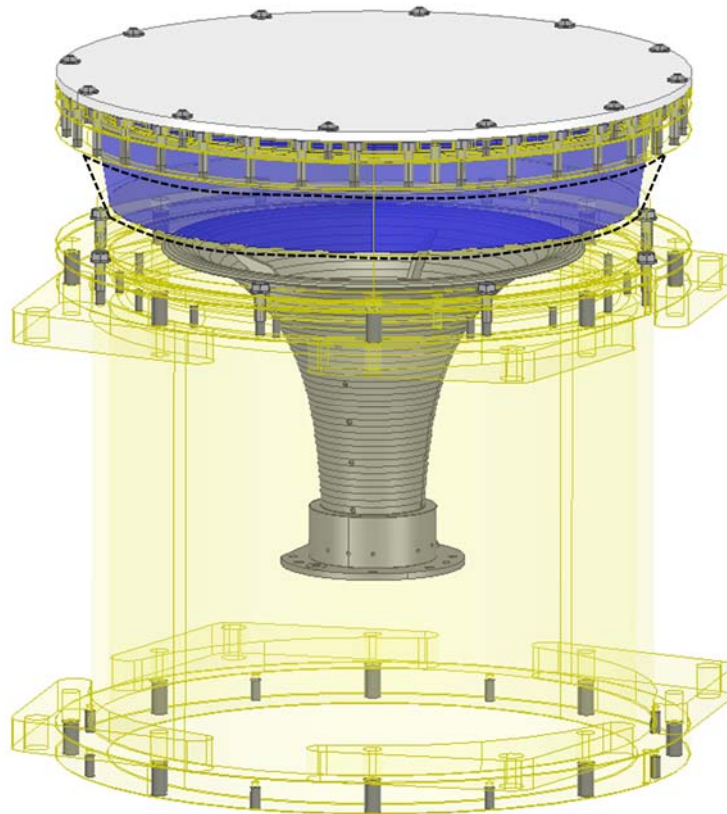


Figure 3.5: Schematic drawing of the cryogenic receiver model simulated.



3.2.2 Measurement of the Cryogenic Dewar

Before installing the cryogenic receiver on the 12-m VLBI antenna, a prototype of the system shown in Figure 3.6, has been manufactured and tested in a full anechoic chamber (CNES ONERA), suited to perform free-space measurements. In particular, the radiation pattern of the QRFH feed has been measured, with and without the Dewar, for the E- and H-plane, in order to appraise the effect of the Dewar. For the sake of simplicity and given that the dual-linear polarizations present anyhow a symmetric pattern, only the results related to one linear polarization are reported.

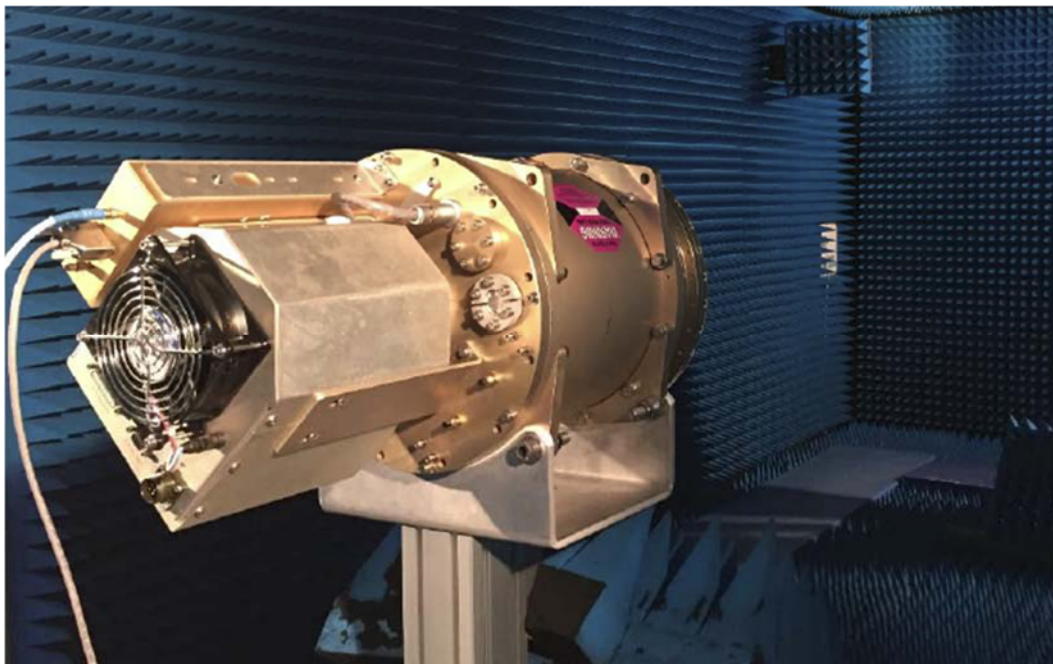


Figure 3.6: Prototype of the cryogenic system measured in the anechoic chamber (ONERA facilities).

As benchmark, three frequencies have been considered: 4.9 GHz, 7GHz and 12 GHz, and the comparisons are shown in:

- Figure 3.7 and Figure 3.8 for the co- and cross-polarization at 4.9 GHz.
- Figure 3.9 and Figure 3.10 for the co- and cross-polarization at 7 GHz.
- Figure 3.11 and Figure 3.12 for the co- and cross-polarization at 12 GHz.

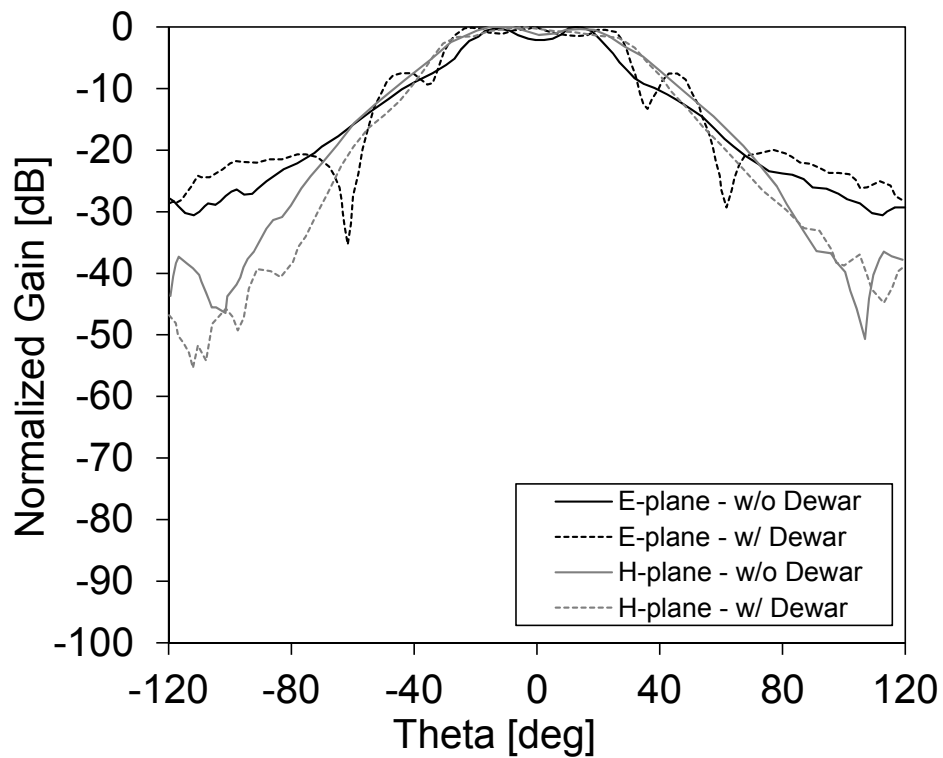


Figure 3.7: Comparison between the radiation patterns with and without the Dewar at 4.9 GHz, for E-plan and H-plan: Co-polarization.

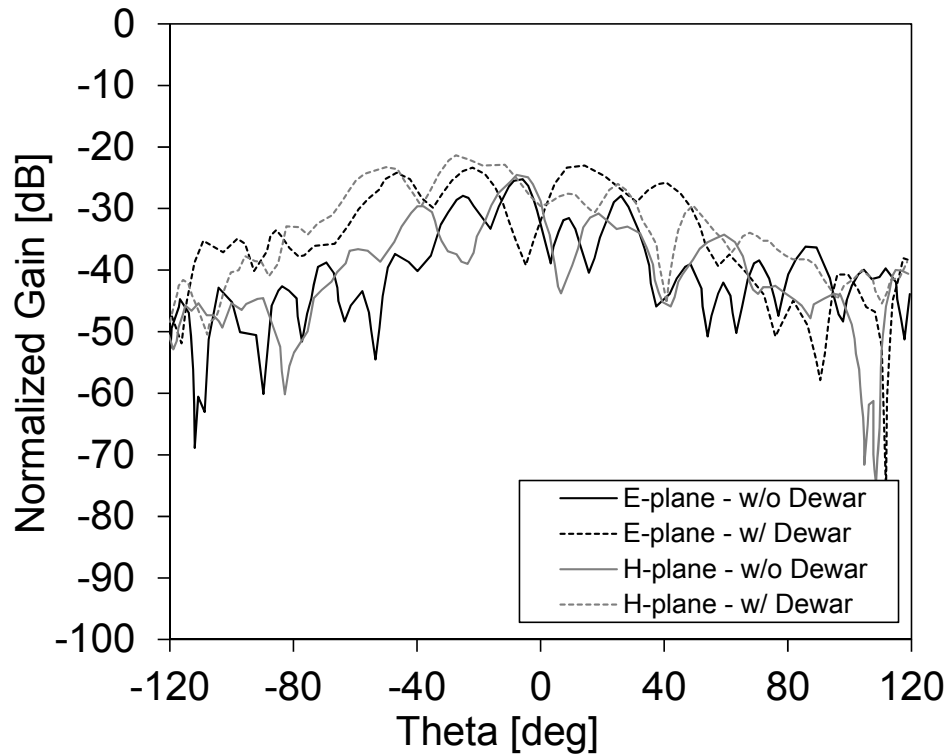


Figure 3.8: Comparison between the radiation patterns with and without the Dewar at 4.9 GHz, for E-plan and H-plan: Cross-polarization.

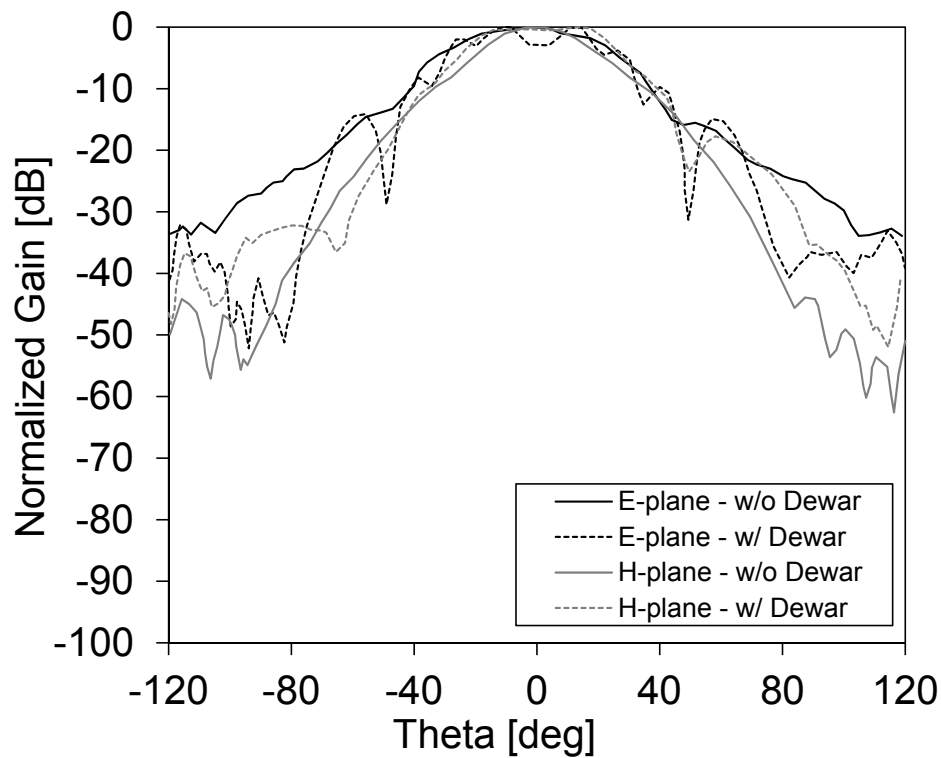


Figure 3.9: Comparison between the radiation patterns with and without the Dewar at 7 GHz, for E-plane and H-plane: Co-polarization.

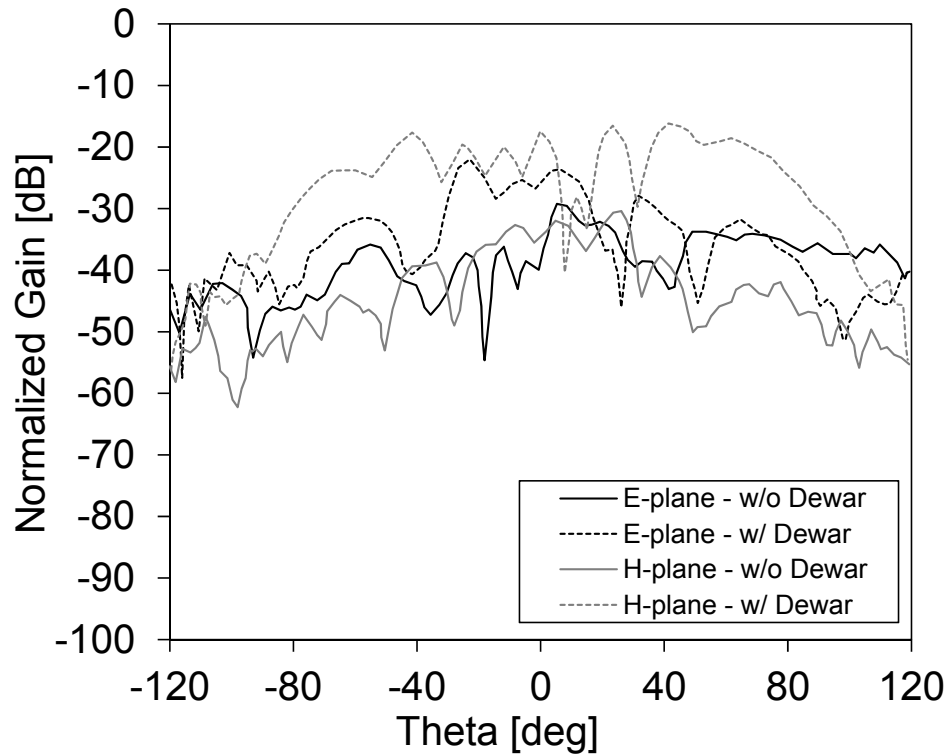


Figure 3.10: Comparison between the radiation patterns with and without the Dewar at 7 GHz, for E-plane and H-plane: Cross-polarization.

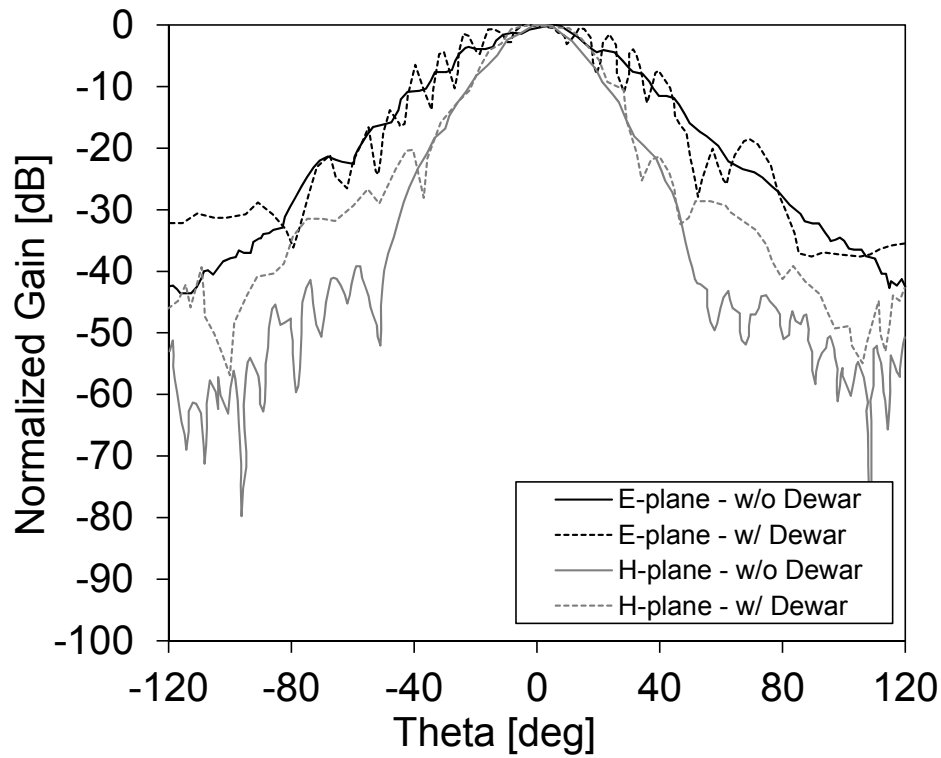


Figure 3.11: Comparison between the radiation patterns with and without the Dewar at 12 GHz, for E-plan and H-plan: Co-polarization.

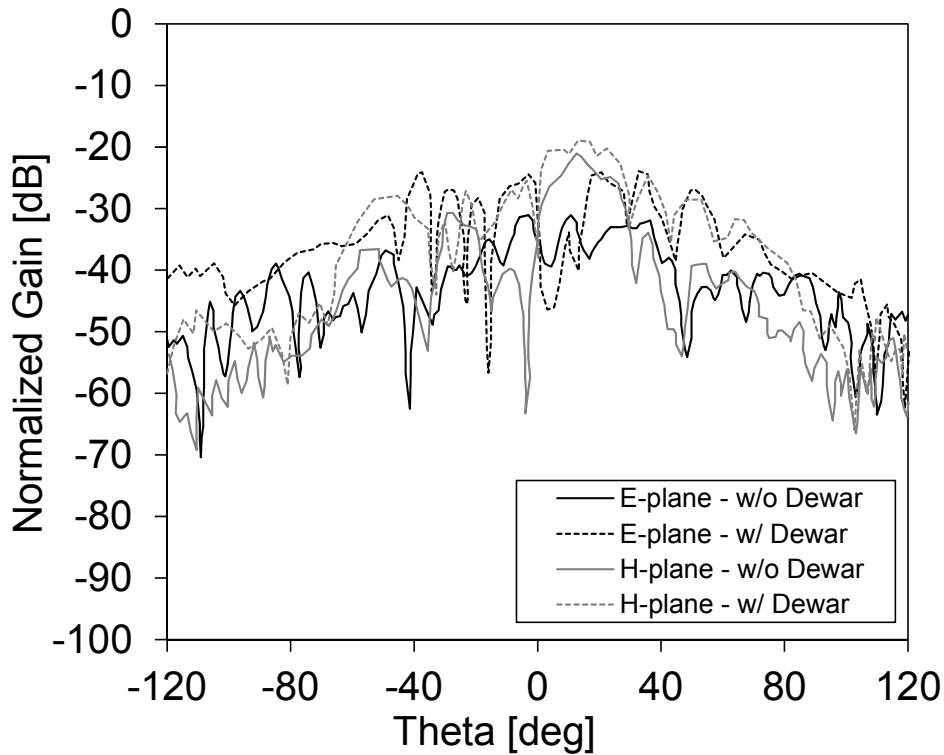


Figure 3.12: Comparison between the radiation patterns with and without the Dewar at 12 GHz, for E-plan and H-plan: Cross-polarization.



It can be observed that the presence of the Dewar does not affect significantly the aperture distribution in terms of the beam-width of the radiated patterns. In addition, the impact on the cross-polarization of the radiated field cause an increase of approximately 10 dB, even if it is nevertheless maintained be low around -20 dB. On the other hand, the presence of the Dewar entails a ripple-like effect in the aperture distribution, which is translated into radiation patterns with ripples, a typical effect of a weak resonances given by the partial (open) metallic cavity. This aspect can be easily appreciated in Figure 3.13 and in Figure 3.14, which show the magnitude of the electric field with and without the Dewar at low and high frequency, respectively. In particular, it can be noted that at 2 GHz the impact of the Dewar is very limited while at 12 GHz the difference is not negligible.

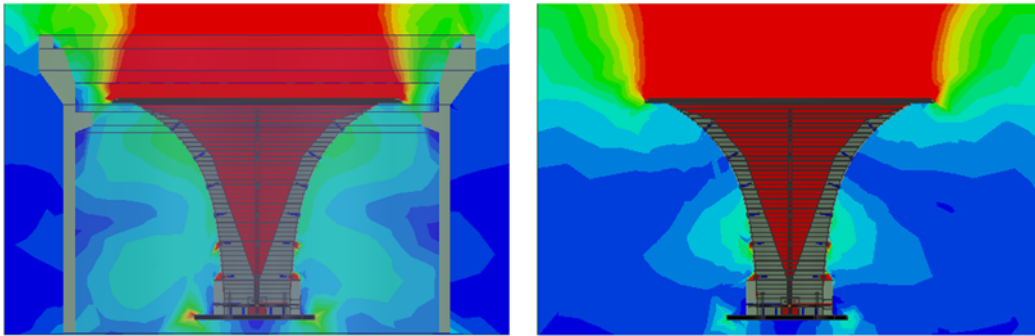


Figure 3.13: 2D sketch of the electric field magnitude distribution at low frequency for an input power of 1 W: (on the left) with the Dewar at 2 GHz; (on the right) without the Dewar at 2 GHz. Colour scale from 0 (blue) to 100 V/m (red).

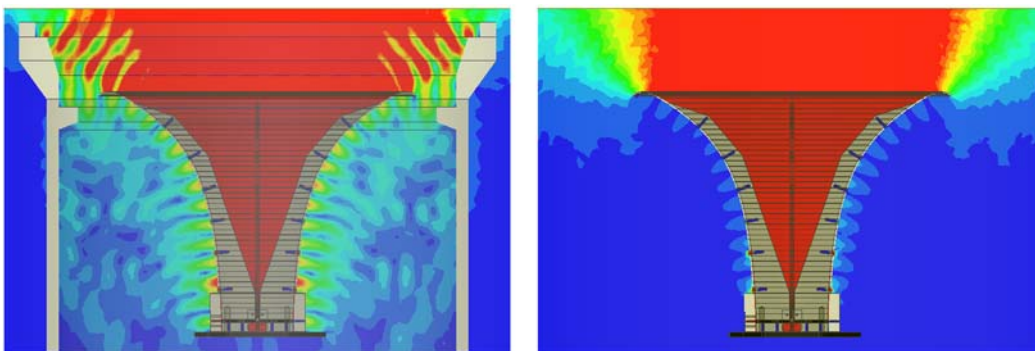


Figure 3.14: 2D sketch of the electric field magnitude distribution at high frequency for an input power of 1 W: (on the left) with the Dewar at 12 GHz; (on the right) without the Dewar at 12 GHz. Colour scale from 0 (blue) to 100 V/m (red).



In addition to the evaluation of the radiation properties, the reflection and transmission coefficient of the QRFH feed has been measured at both ports. The comparison between those parameters with (grey lines) and without (black lines) Dewar is shown in Figure 3.15. It is possible to note that a good isolation (transmission coefficient), better than around -30 dB, is maintained along the frequency range 2 - 14 GHz in both cases. Conversely the input matching (reflection coefficient), beyond to provide performance better than around -10 dB and -8 dB in the frequency range 2.5 - 14 GHz, the comparison with and without Dewar is quite concordant and the trend is respected for the whole frequency range.

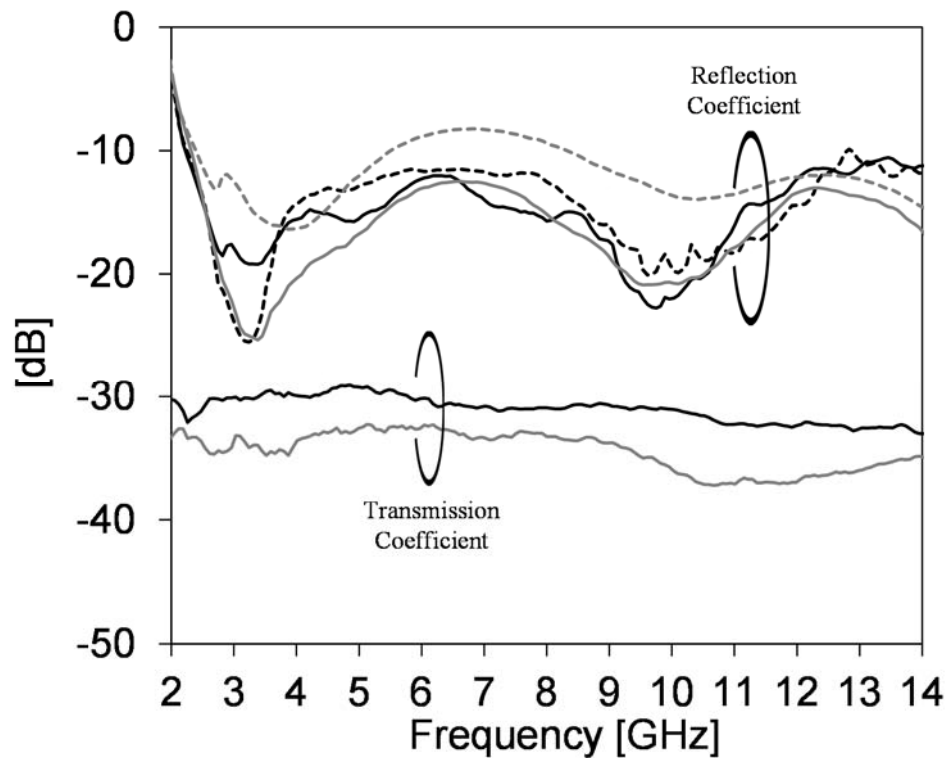


Figure 3.15: Reflection coefficient (Input matching) and transmission coefficient (Isolation) measured at both ports. Measured reflection coefficient with (solid and dashed grey lines) and without (solid and dashed black lines) the Dewar measured at both ports. Measured transmission coefficient with (solid grey line) and without (solid black line) the Dewar.

The noise temperature represents an important parameter to test in these applications, and generally it is evaluated excluding external noise contributions (i.e. noise temperature of the sky or noise temperature of the ground). The noise temperature measurement has been performed by Y-factor technique, connecting the receiver input to different



adapted loads with known temperatures: a high temperature state (when the load has a higher output noise power) and a low temperature state (when the load has a reduced output noise power). The noise temperature has been measured in the frequency range 3 - 14 GHz and the active stage is based on an LNA from Low Noise Factory (LNF-LNC0.3_14A) with a noise temperature at room temperature from around 65 K at 2 GHz to around 85 K at 14 GHz. The experimental results, measured at a physical temperature of 80 K, are reported in Figure 3.16. It can be observed that the values are better than around 40 K, which represents the specification given by the VLBI Global Observing System (VGOS).

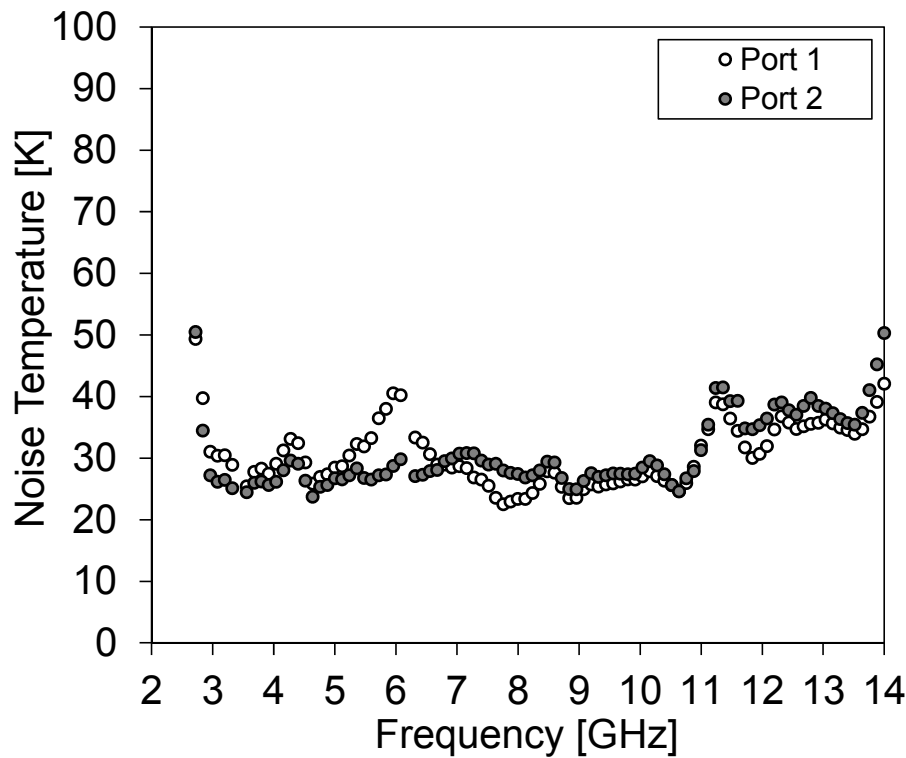


Figure 3.16: Noise temperature measured at both ports of the cryogenic receiver.



3.3 12-m Radio Telescope

The cryogenic receiver discussed in the previous section, has been designed to be installed on the 12-m Hobart antenna located in Tasmania, which is part of the AuScope VLBI array [27], an infrastructure composed by three radio telescopes separated by more than 2000 Km between each other. Figure 3.17 shows the locations of these stations: Hobart (Tasmania), Katherine (Northern Territory) and Yarragadee (Western Australia), whereas Figure 3.18 shows a photo of the Hobart antenna. This antenna, whose RF optical design is based on the system presented in [28], is characterized by a shaped Cassegrain configuration optimised to maximize the G/T_{SYS} performance and minimize the losses incurred by the blockage of the feed. Another critical feature that has to characterize this kind of radio telescopes, concerns the drive speed. Given that the fast switching from source to source is a critical task in the telescope operations, it is advisable to favor small structures (i.e. 12-m rather than 25-m diameter) with powerful drive motors [29]. In this way, it is possible to observe more sources at wide separations on the sky in a given time interval [30] and consequently to provide better performance for the specific needs of a geodetic VLBI array. As example, these kind of antennas can move around at up $5^\circ/\text{s}$ in azimuth and $1.5^\circ/\text{s}$ in elevation.

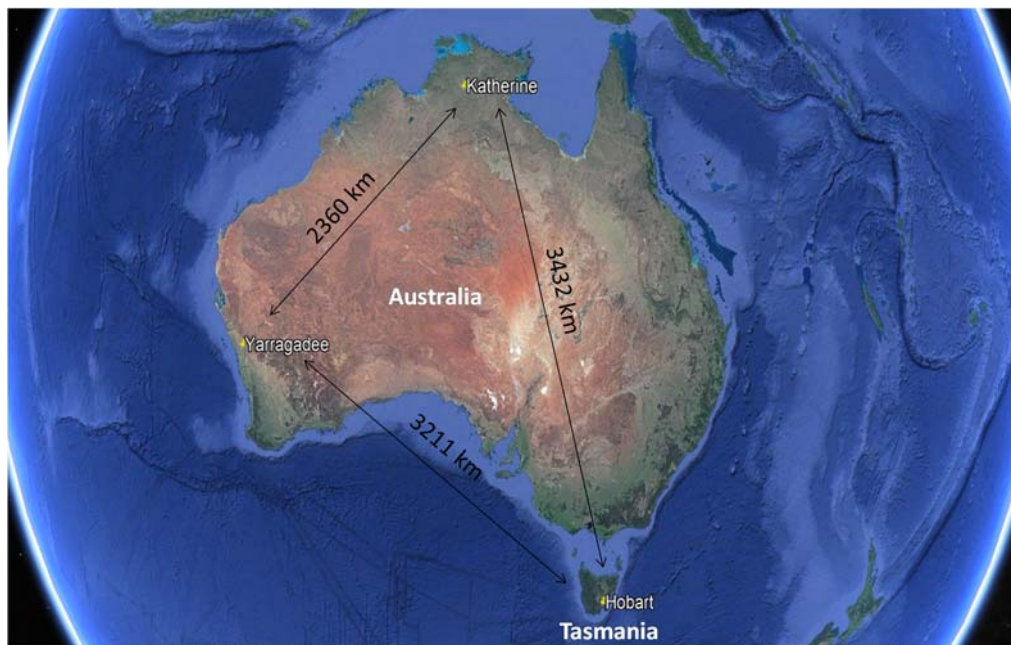


Figure 3.17: Geographical distribution of the AuScope VLBI infrastructure.

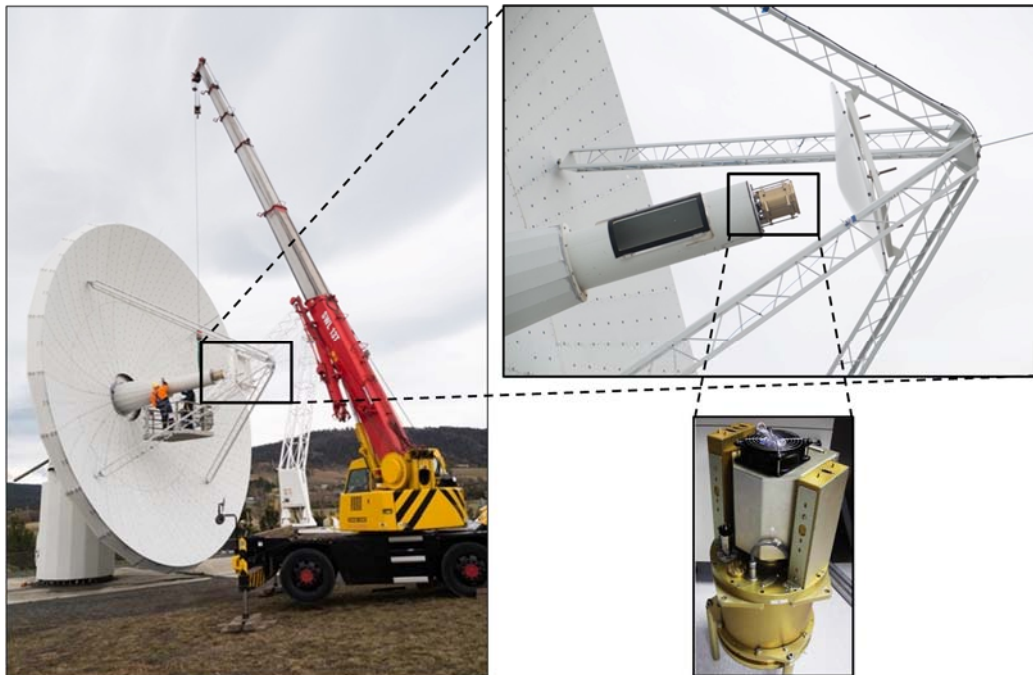


Figure 3.18: Photo of the 12-m Hobart antenna. It is possible to appreciate the cryogenic receiver (represented in gold colour) installed in front of the shaped sub-reflector (highlighted in the black boxes, respectively). Photo credits of Callisto.

3.3.1 Analysis of the antenna system

It has been shown that in a cryogenic receiver, the Dewar may involve radio frequency interferences, in particular at high frequency by means a distortion of the radiation pattern of the feed surrounded. Therefore, it is fundamental to evaluate if this inconvenience would cause a deterioration on the performance of the antenna.

The antenna system has been modelled and simulated by the hybrid combination between PO (Physical Optic) and FEM (Finite Element Method) method. The feed system, characterized by the cryogenic receiver, has been simulated by Ansys HFSS (FEM method) [30] and its radiation pattern has been imported in an asymptotic method⁴ (Tiera GRASP), useful to simulate electrically large structures, in which the whole antenna system characterized by the sub- and the main-reflector has been analysed.

In Figure 3.19 the schematic drawing of the antenna system implemented in the EM simulators is shown.

⁴ Description of the procedure adopted may be found in Appendix C.

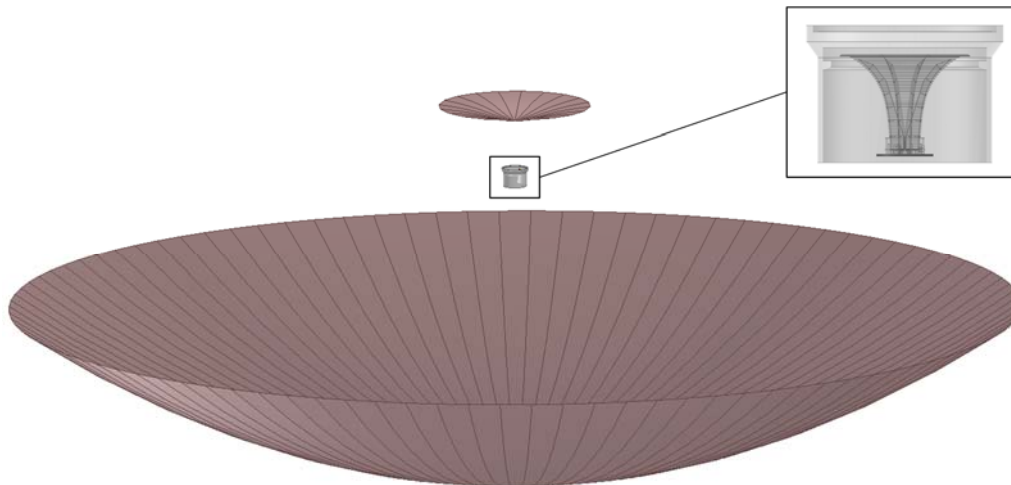


Figure 3.19: Schematic drawing of the antenna modelled by GRASP. In the black box the representation of the QRFH feed enclosed by the Dewar is highlighted.

The radiation pattern has been simulated for different frequencies and the comparison with (w/) and without (w/o) Dewar is shown in:

- Figure 3.20, for the co- and cross-polarization at 2 GHz.
- Figure 3.21, for the co- and cross-polarization at 4 GHz.
- Figure 3.22, for the co- and cross-polarization at 6 GHz.
- Figure 3.23, for the co- and cross-polarization at 8 GHz.
- Figure 3.24, for the co- and cross-polarization at 10 GHz.
- Figure 3.25, for the co- and cross-polarization at 12 GHz.
- Figure 3.26, for the co- and cross-polarization at 14 GHz.

For the sake of simplicity and since the antenna presents anyhow a circularly symmetric pattern, only the cut $\phi = 0$ deg is reported. As it can be easily noted, it exists a good overlapping between the co- and cross-patterns compared and therefore the Dewar practically does not affect the radiation characteristics of the antenna system.

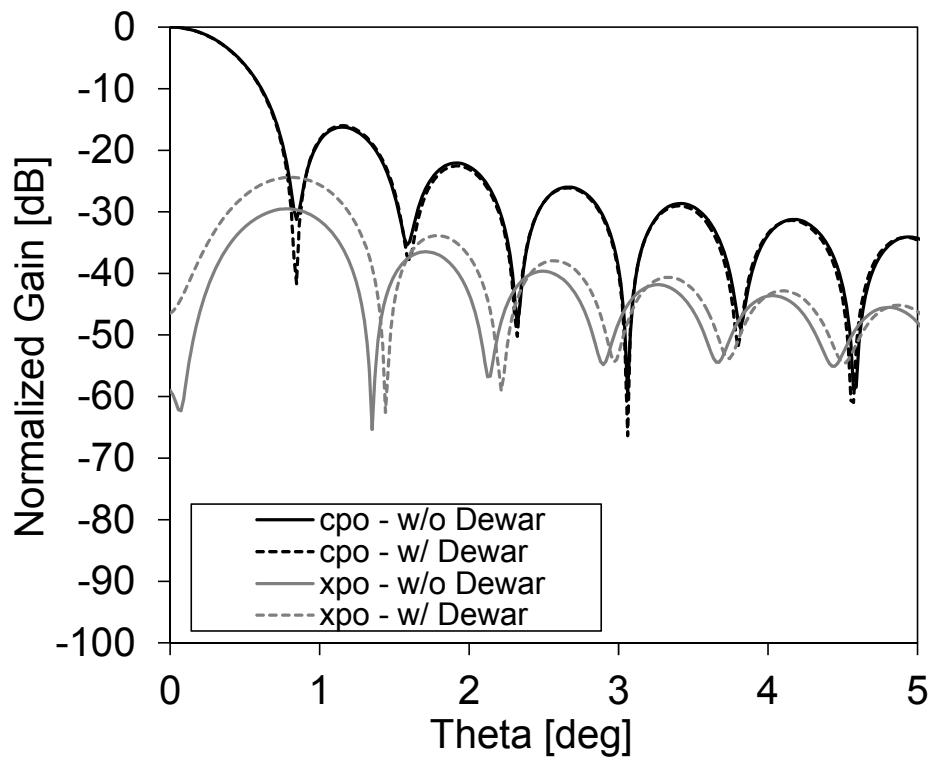


Figure 3.20: Antenna radiation pattern simulated at 2 GHz. Comparison with (w/) and without (w/o) the Dewar.

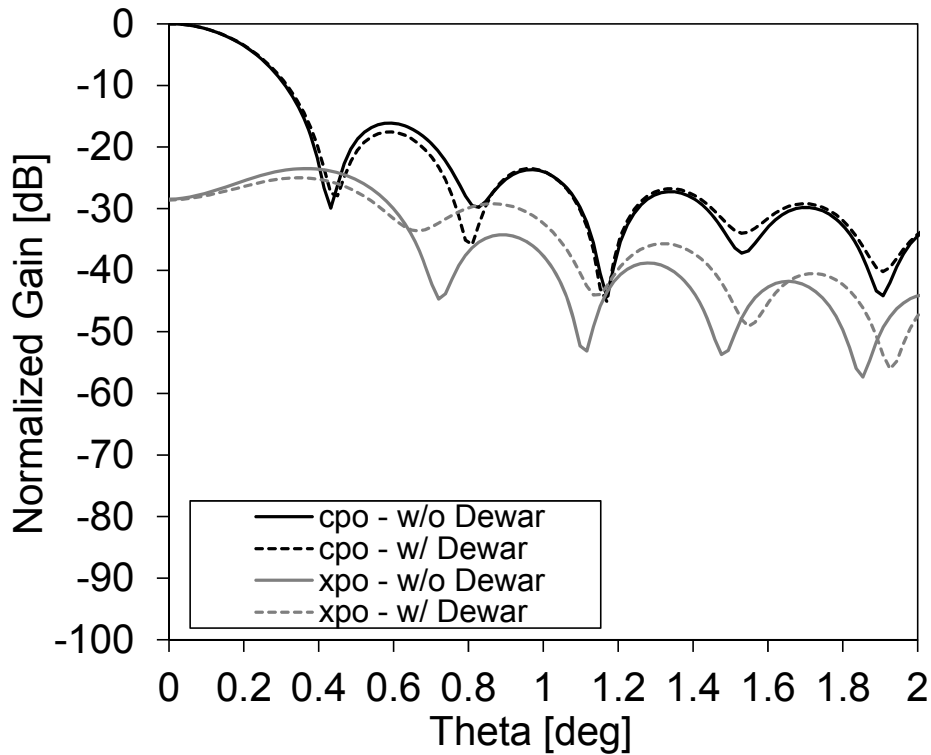


Figure 3.21: Antenna radiation pattern simulated at 4 GHz. Comparison with (w/) and without (w/o) the Dewar.

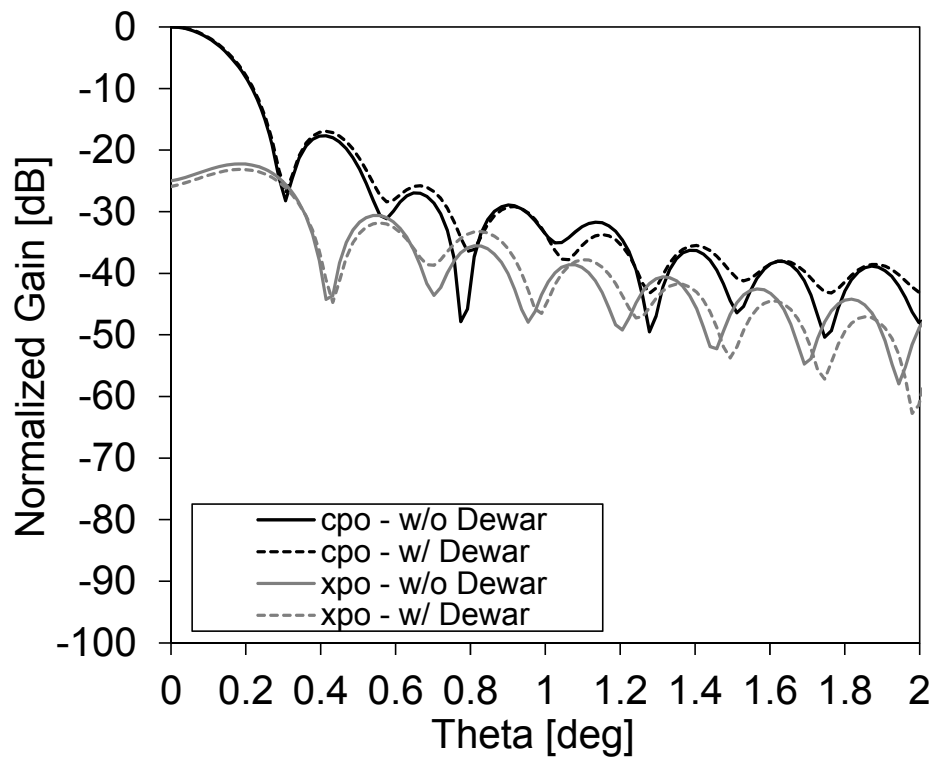


Figure 3.22: Antenna radiation pattern simulated at 6 GHz. Comparison with (w/) and without (w/o) the Dewar.

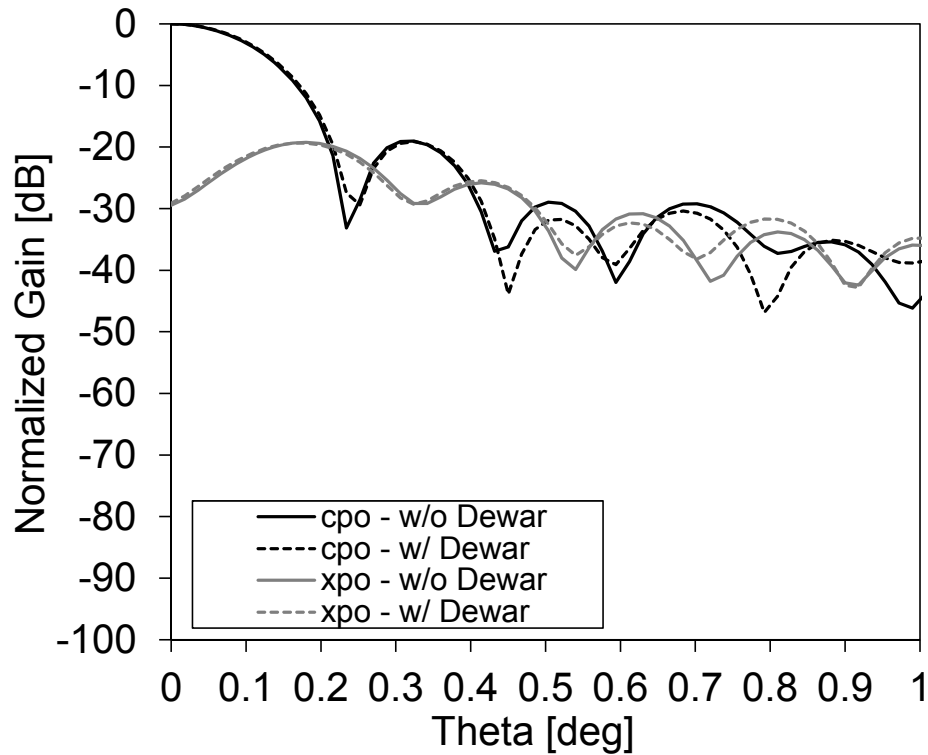


Figure 3.23: Antenna radiation pattern simulated at 8 GHz. Comparison with (w/) and without (w/o) the Dewar.

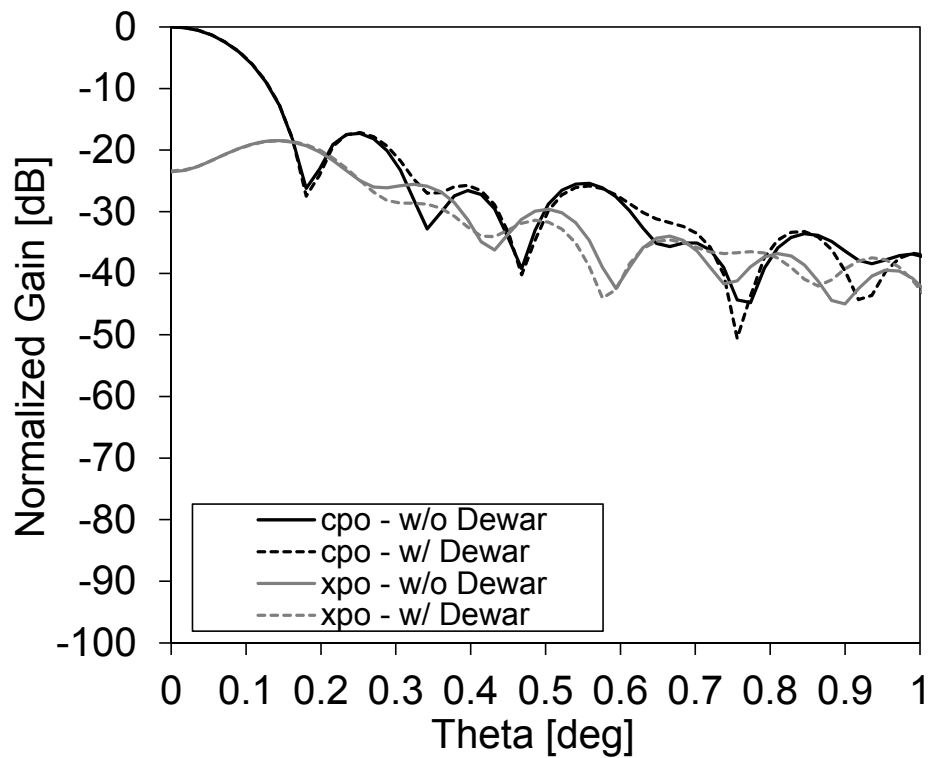


Figure 3.24: Antenna radiation pattern simulated at 10 GHz. Comparison with (w/) and without (w/o) the Dewar.

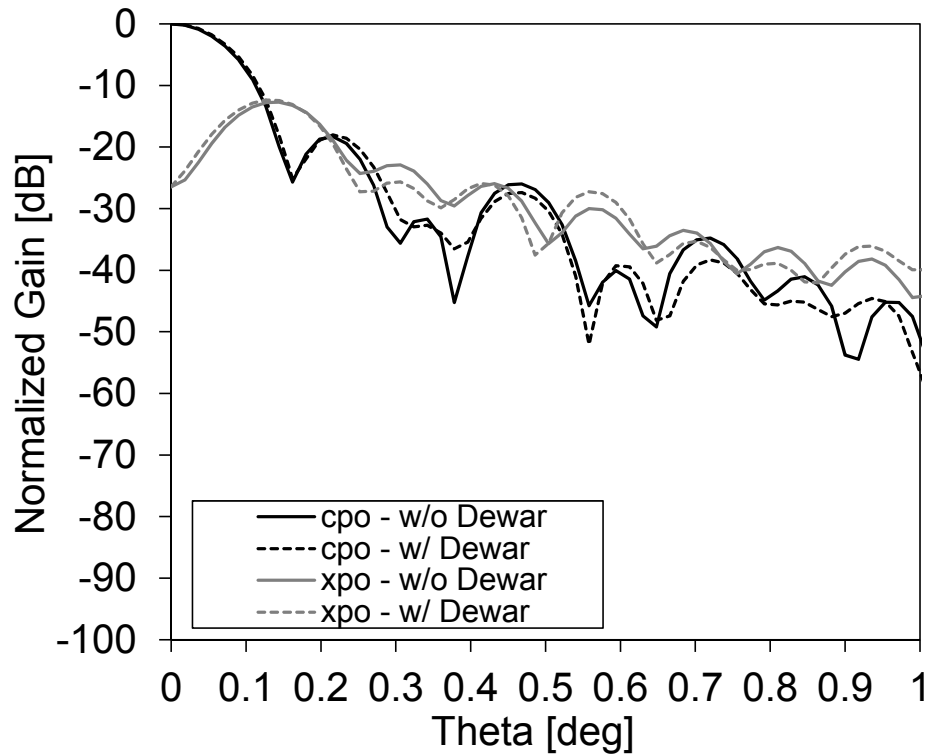


Figure 3.25: Antenna radiation pattern simulated at 12 GHz. Comparison with (w/) and without (w/o) the Dewar.

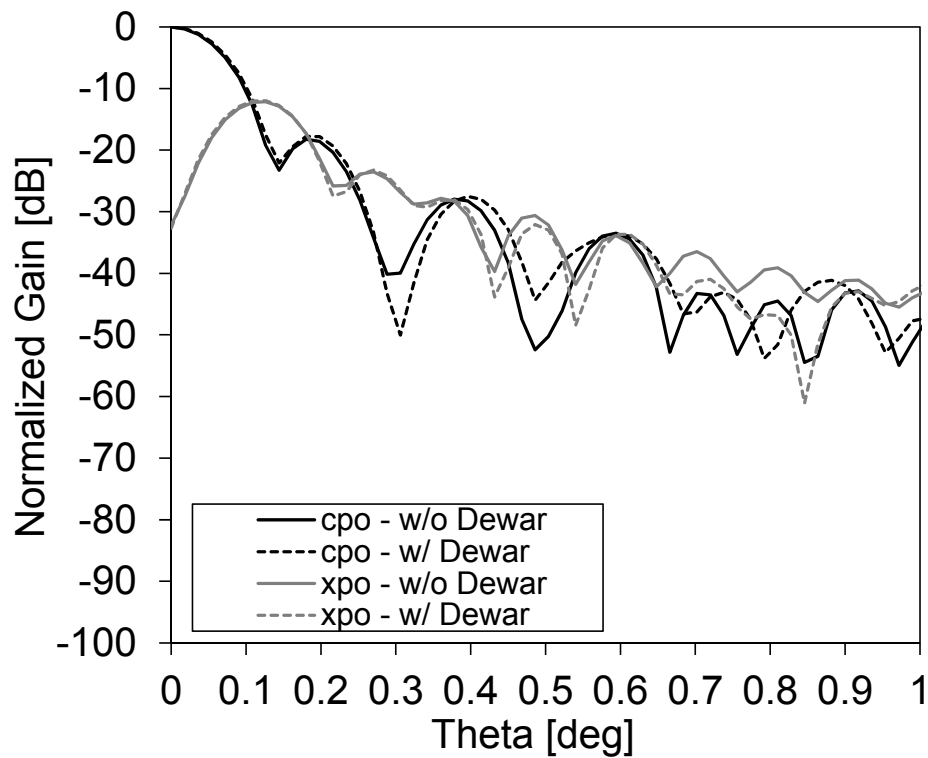


Figure 3.26: Antenna radiation pattern simulated at 14 GHz. Comparison with (w/) and without (w/o) the Dewar.

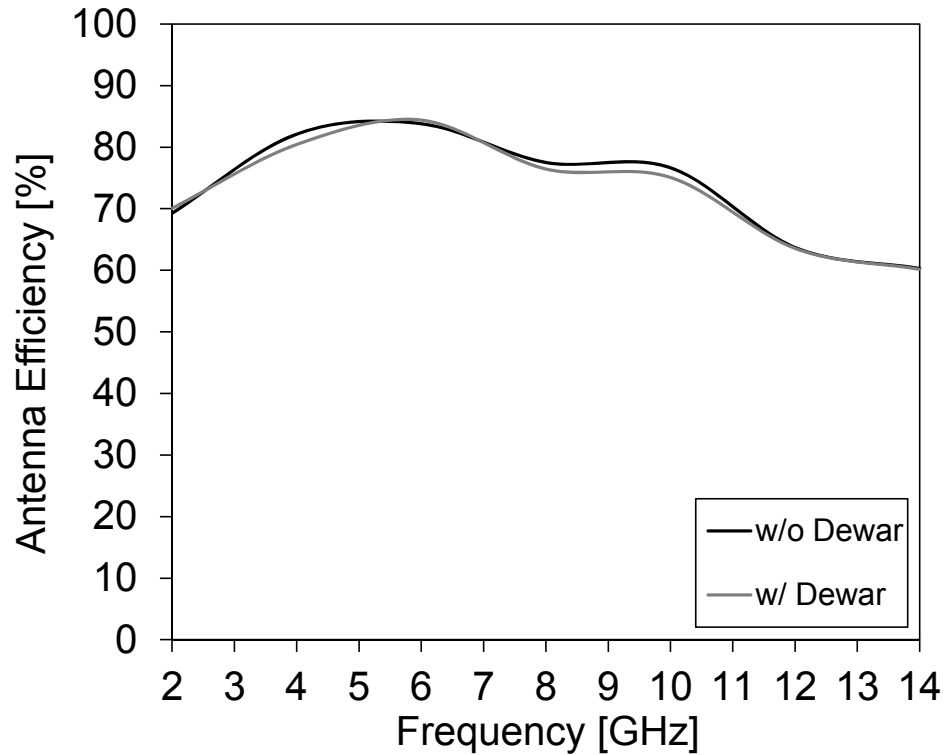


Figure 3.27: Antenna efficiency computed for the entire frequency range. Comparison with (w/) and without (w/o) the Dewar.



It has been observed that the presence of the Dewar does not have any impact on the performance of the antenna. In fact, it can be noted that the trend of the co- and cross-polarization is unchanged, the level of the side-lobes, the cross-polarization and the beam-width is maintained, and in addition it is possible to observe that no distortion of the radiation pattern (i.e., beam-squint) is achieved. To simplify the assessment, in addition to the radiation patterns, the antenna efficiency has been calculated to simplify the comparison through a unique parameter as a function of the frequency. The computed antenna efficiency is shown in Figure 3.27 which sets out, as expected, no significant changes providing an additional demonstration about the very limited impact of the Dewar.



3.4 Calibration of the VLBI receivers

In the VLBI applications the signals received are generally subjected to the same problems [31] arising from the interferometry, and the question that each individual radio telescope is separated by hundreds or thousands kilometres from the others, adds few complications. The largest issue, due to the variations of the electric properties in the atmosphere, can cause a scattered energy away from the correct direction of the source and consequent different time delays of the radio waves. This phenomenon entails a reduction of the SNR and in extreme cases the total hindrances of the detections. Therefore, a calibration of the receiver is necessary as counter measure to avoid the possible limitations [32, 33]. In general the calibration procedure uses a noise calibration system to measure the variations in the power sensitivity, and a phase calibration system to measure the variations in the in system phase/delay. The procedure can be implemented by two different techniques: a direct signal injection and an irradiative signal injection. The first technique incorporates a microwave component for the injection of the calibration signal into the frontend (i.e. between the feed and the LNA, as currently used for S/X band system) of the receiver. Whereas the second technique uses a small broadband probe to radiate the calibration signal into the front-end of the receiver. Even if this latter approach can be influenced (on the basis on the radiation properties of the probe antenna) by multipath, it avoids the necessity to realize high-performance microwaves components with ultra-wide band characteristics, as required by the former approach, hence the consequent need to adapt the others components (i.e. LNAs). For these reasons, in the frame of this project the second approach has been choice, and ultra-wide-band probe antennas have been designed to irradiate the calibration signal within the feed.

3.4.1 Design of the Ultra-Wideband (UW) Coaxial Probe Antenna

An UW-Coaxial probe antenna [34] has been manufactured by two U.S. one cent pieces (pennies) and a semi-rigid coaxial cable characterized by an inner conductor with a radius equal to 0.419 mm, an outer conductor with a radius equal to 1.448 mm, and the inner dielectric is realized by Teflon. A 3D sketch of the antenna model is shown in Figure 3.28 in which the two pennies have a diameter of 19 mm whereas the coaxial line feed is divided in three different segments: $a = 17$ mm, $b = 2$ mm and $c = 53$ mm. A prototype has been manufactured and a photo is shown in Figure 3.29.

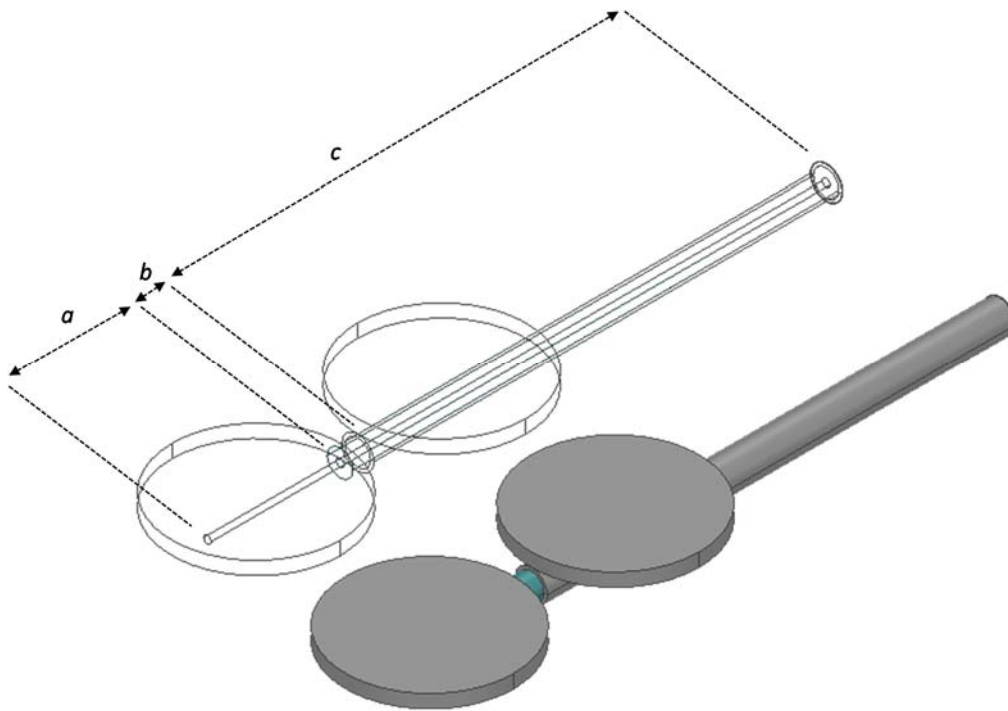


Figure 3.28: Schematic drawing of the UW-Coaxial probe antenna. Dimension of the segments along the axial direction: $a = 17$ mm, $b = 2$ mm and $c = 53$ mm.



Figure 3.29: Prototype of the UW-Coaxial probe antenna manufactured.

The input matching of the probe antenna has been simulated by Ansys HFSS and the good agreement with the measurement can be observed in Figure 3.30. Given that the antenna has been designed for the calibration signal injection thus for near-field use, it has not been characterized in terms of the radiation properties (i.e. Gain or Directivity). Beyond to the fact that these kind of ultra-wide-band devices are generally characterized by an omnidirectional radiation pattern, the relevant parameter for these particular functions concerns the coupling factor with the QRFH feed enclosed.

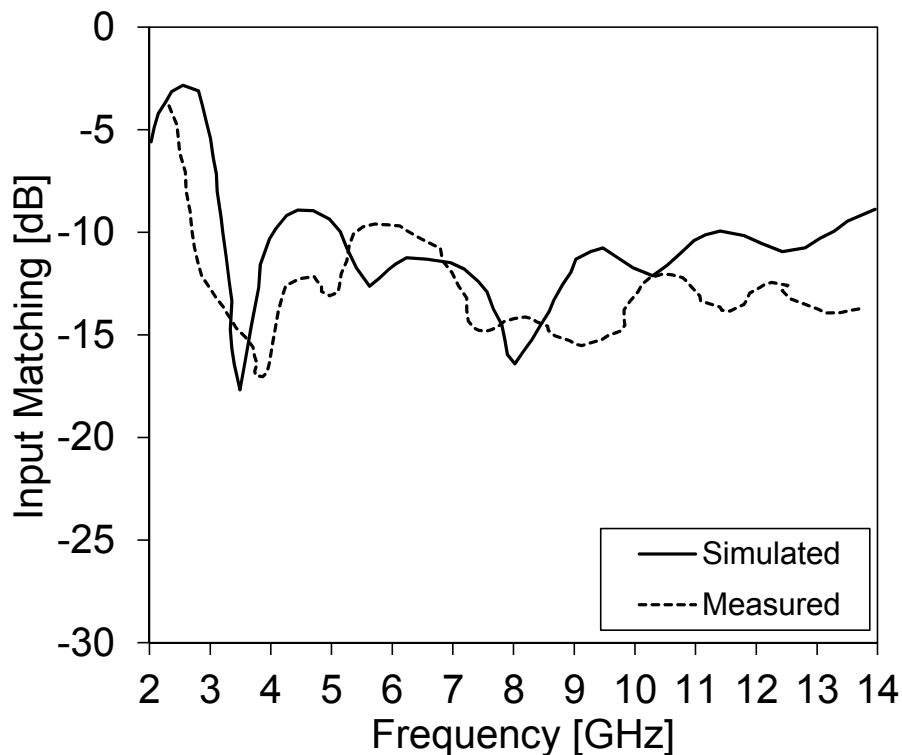


Figure 3.30: Input matching of the UW-Coaxial probe antenna. Comparison between simulation and measurement.

3.4.2 Optimization of the coupling factor between the UW-Coaxial probe antenna and the QRFH feed

The UW-Coaxial probe antenna designed has been included into the HFSS model of the cryogenic Dewar as shown in Figure 3.31, and the optimum position has been identified to achieve a minimum coupling factor of -35 dB from 2 GHz to 14 GHz for the two QRFH feed input ports. While the vertical displacement of the probe antenna with respect to the QRFH feed aperture and the distance respect to the QRFH feed central axis are fixed because of mechanical constraints.

Different positions have been investigated including angular locations close to port 1 and close to port 2 as presented in Figure 3.32. Due to the QRFH feed characteristics, which works with a dual linear polarization, it is clear through the Figure 3.33 that the coupling factor appears higher with the nearest port.

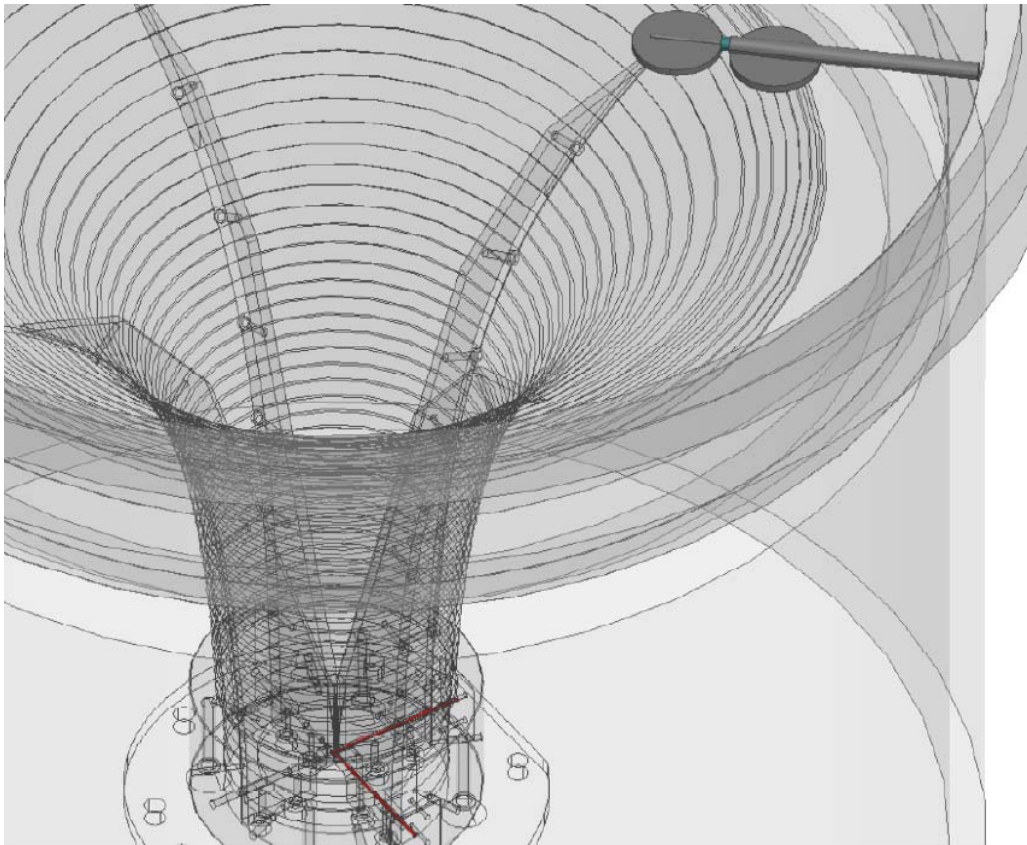


Figure 3.31: Schematic drawing of the UW-Coaxial probe antenna (upper-right) integrated in the cryogenic Dewar. The QRFH ports (lower-centre) are shown in light red.

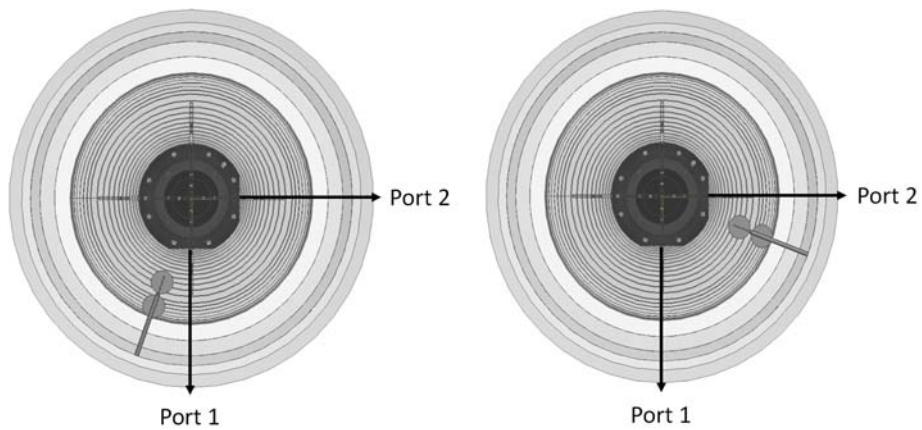


Figure 3.32: Schematic drawing of the UW-Coaxial probe antenna placed in different positions. Near the port 1 (on the left) and near the port 2 (on the right).

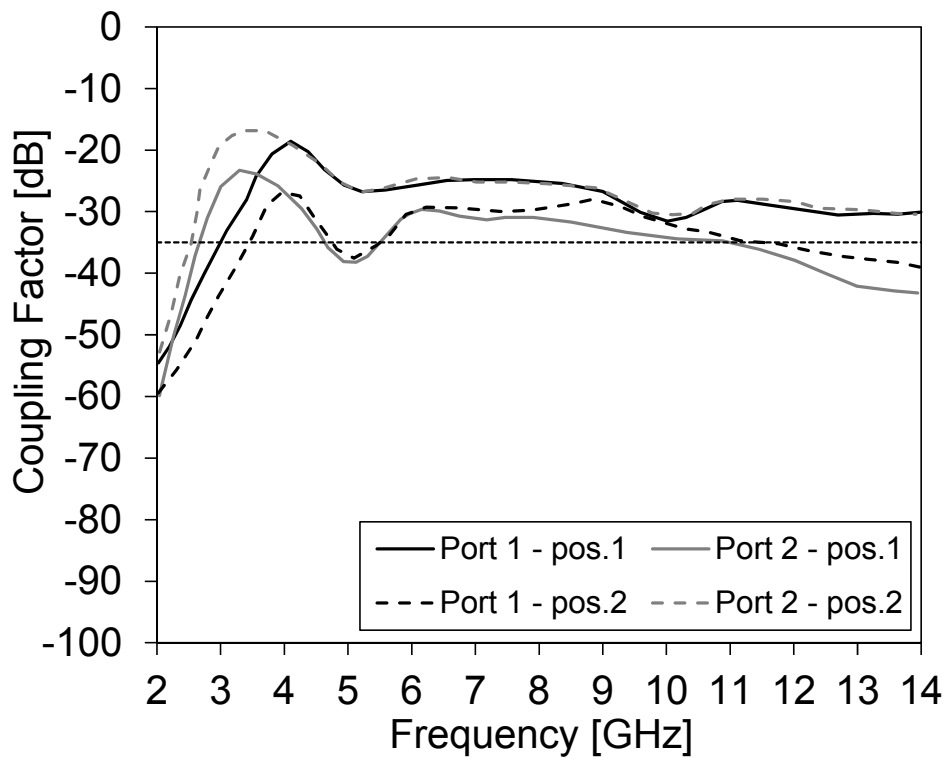


Figure 3.33: Coupling factor of the positions investigated near the port 1 (pos.1) and near the port 2 (pos.2).
The specification of -35 dB to be met is outlined.

For this reason, a balanced solution has been investigated placing the antenna probe at 45 degree from both port 1 and port 2, as shown in Figure 3.34.

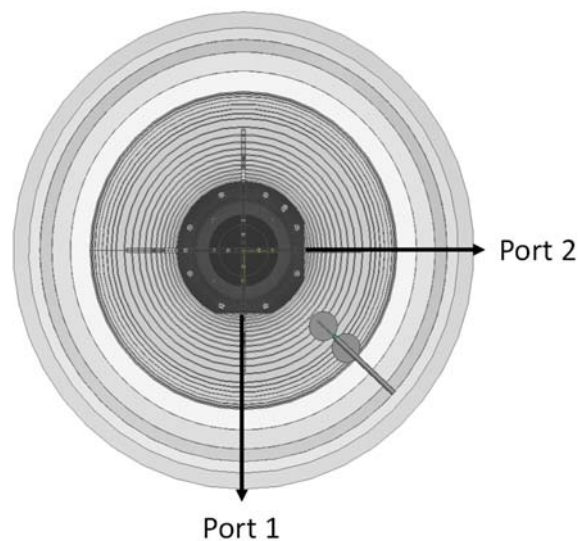


Figure 3.34: Balanced solution: schematic drawing of the UW-Coaxial probe antenna placed at 45 degree from both port 1 and port 2.



As expected, a balanced coupling factor between port 1 and port 2 is achieved and shown in Figure 3.35. Beyond to the fact the specifications required are properly satisfied (greater than -35 dB, outlined with the horizontal dashed black line in Figure 3.35), it is possible to observe an excellent agreement between simulations and measurements, while some discrepancies can be noted for lower frequencies. This is probably due to the poor manufacturing of the UW-Coaxial probe antenna.

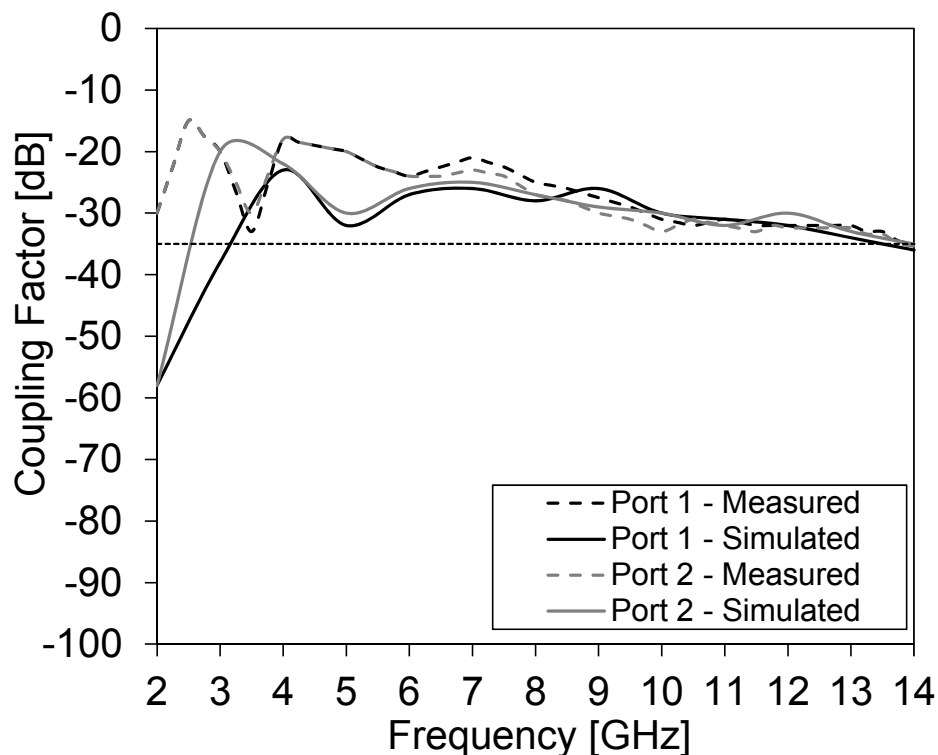


Figure 3.35: Coupling factor between the UW-Coaxial probe antenna and the QRFH feed. Comparison between simulation and measurement. The specification of -35 dB to be met is outlined.

In addition, the problem related to the possible impact due to the presence of the probe antenna in front of the QRFH feed, has been considered and addressed in [35]. Through EM analysis has been demonstrated that the impact on the radiation pattern of the receiver is negligible and therefore it represents a good solution for the irradiative injection purposes.



3.4.3 Design of the Ultra-Wideband PCB Probe Antenna

Although the results achieved using the UW-Coaxial probe antenna are very satisfactory concerning the coupling factor, this kind of solution is not suitable from the engineering point of view due to the poor feasibility and repeatability. For this reason, a Printed Circuit Board (PCB) microstrip solution, characterized by a double side, has been investigated and designed in order to overcome the limitation. Given that the design has to satisfy some geometrical restrictions, it is required a maximum size of 50x30x10-mm. In particular, the actual dimensions are 50x25x1.52-mm in which the thicknesses of the metal top and bottom layer are not considered. The schematic drawing of the UW-PCB probe antenna designed is shown in Figure 3.36 and the manufactured prototype is reported in Figure 3.37. As possible to observe, the layout is characterized by a dual layer, which the top one is necessary to realize the irradiative source whereas the bottom one is necessary to realize the matching for the entire band-width. In addition, in the sketch, in which it is possible appreciate both geometrical shapes that characterize the top and bottom layer. The geometrical dimensions and the parameters of the substrate used, like the dielectric constant (ϵ_r), the loss tangent ($\text{tg}\delta$), the thickness of the substrate (h) and the thickness of the copper layers (t) are reported in Table 9.

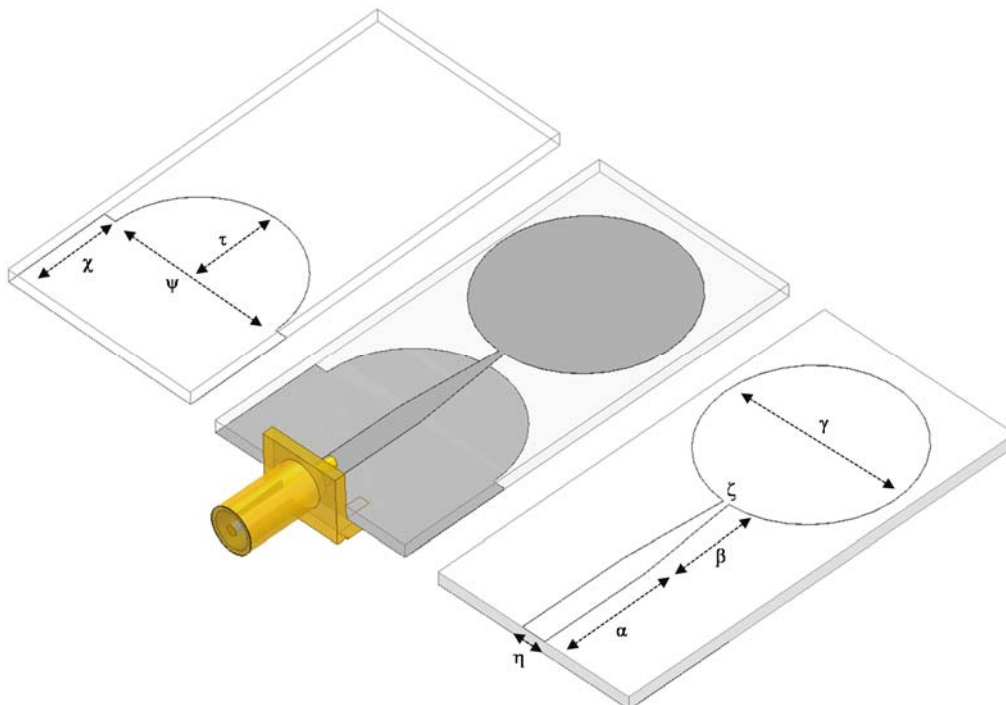


Figure 3.36: Schematic drawing of the UW-PCB probe antenna. The several dimensions that characterize the geometrical shape for both sides are highlighted and the numerical values are reported in Table 9.

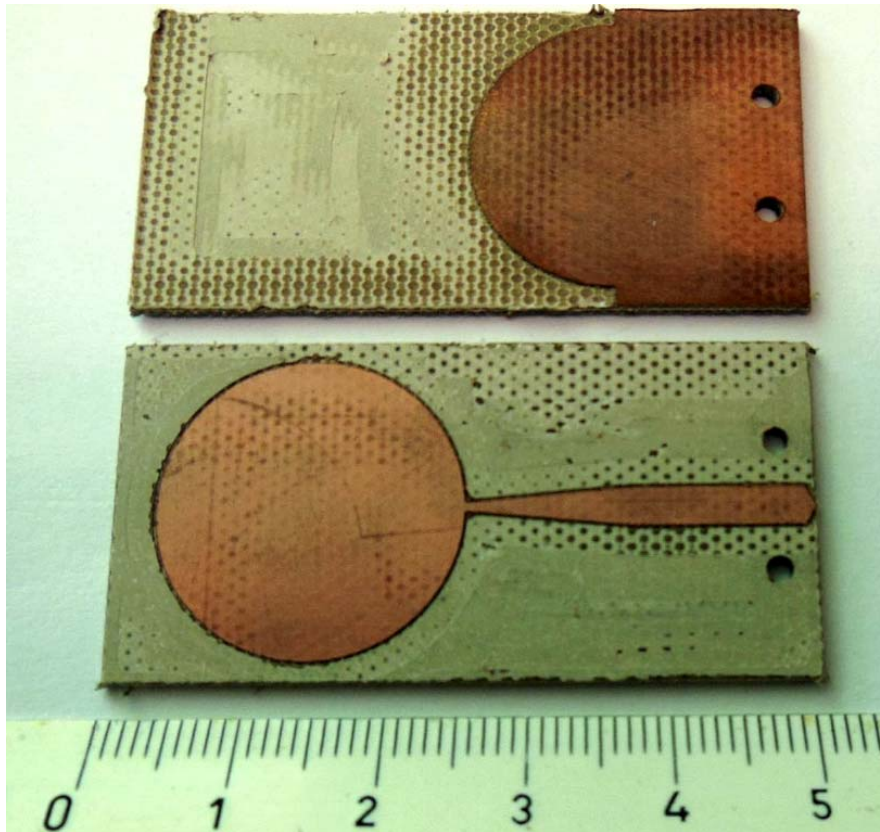


Figure 3.37: Prototype of the UW-PCB probe antenna manufactured. (Scale in centimetres).

Parameter	Value	Parameter	Value
Dielectric Constant (ϵ_r)	3.5	α (mm)	13
Loss Tangent ($\text{tg}\delta$)	0.0018	β (mm)	11.95
Substrate thickness (mm)	1.52	γ (mm)	22
Copper thickness (mm)	0.035	ζ (mm)	0.682
		η (mm)	2.95
		τ (mm)	11
		χ (mm)	13
		ψ (mm)	22

Table 9: Characteristics of the substrate (Taconic - RF-35-0600-C1/C1) used to realize the UW-PCB probe antenna.

The input matching of the UW-PCB probe antenna has been simulated by HFSS and the good agreement with the measurement can be observed in Figure 3.38. On the basis of the optimum position (balanced solution at 45 deg from the port1 and the port 2),



investigated in the previous section, the coupling factor between the probe and the QRFH feed has been evaluated and tested, as presented in Figure 3.39. Figure 3.40 reports the comparison between the coupling factor with both ports, measured and simulated respectively.

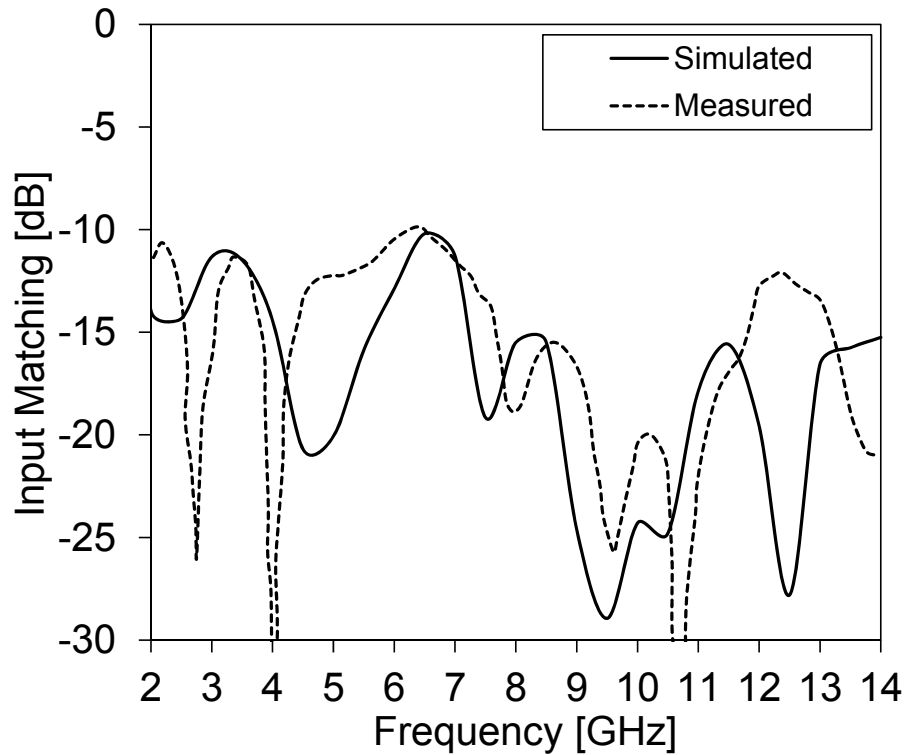


Figure 3.38: Input matching of the UW-PCB probe antenna. Comparison between simulation and measurement.

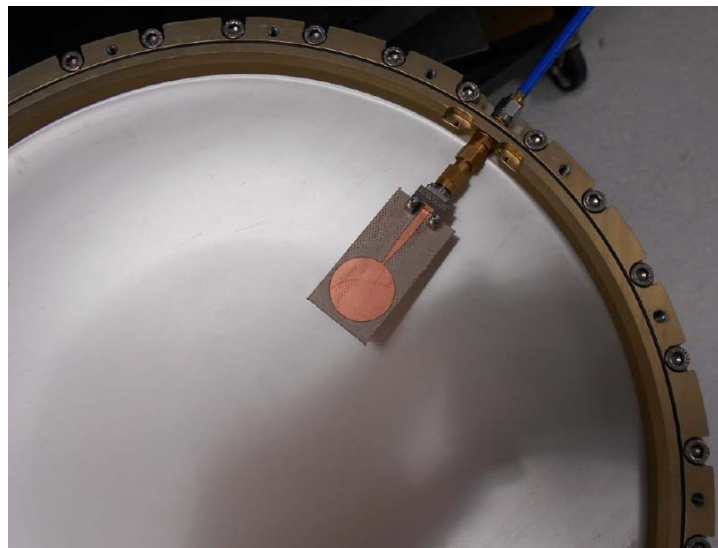


Figure 3.39: Measurement phase of the coupling factor between the UW-PCB probe antenna and the QRFH feed enclosed by the cryogenic Dewar. Photo credits of Callisto.

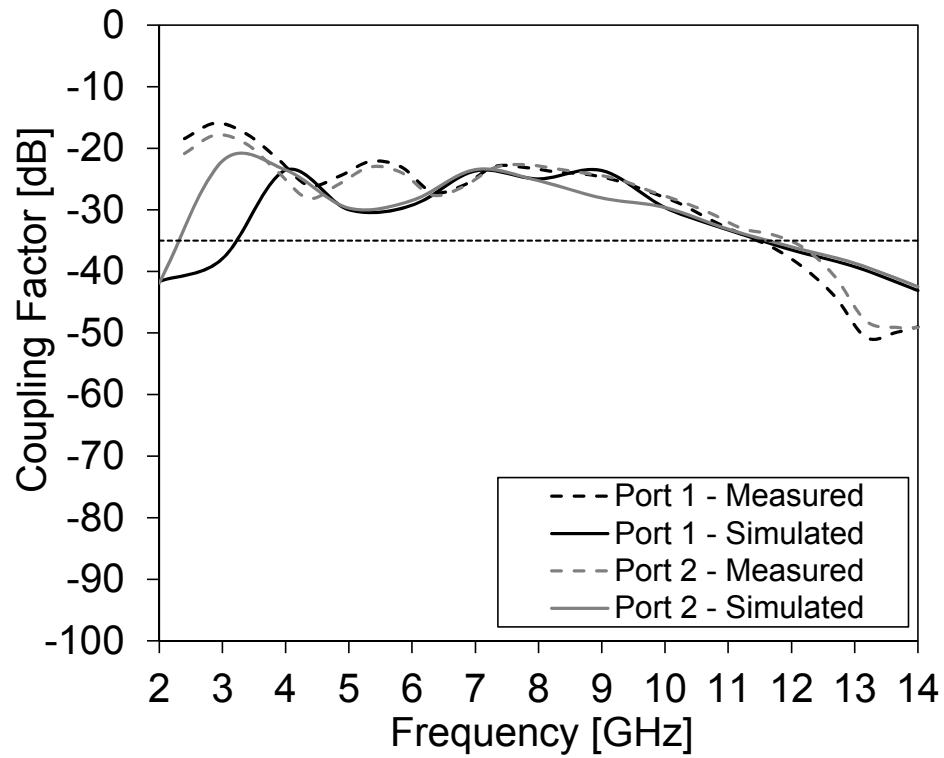


Figure 3.40: Coupling factor between the UW-PCB probe antenna and the QRFH feed. Comparison between simulation and measurement. The specification of -35 dB to be met is outlined.



3.4.4 Summary

In this section it has been addressed the topic concerns the calibration of the VLBI receivers. In the frame of this project the irradiative approach has been choice and in particular two different probe antennas (coaxial and printed version) have been designed. In Figure 3.41 a general comparison between the two solutions is shown in terms of the coupling factor, which is the key parameter to consider for these purposes. As it can be noted, the UW-Coaxial probe provides satisfactory results while the UW-PCB probe presents some restrictions at higher frequencies, due to the fact that it is not perfectly omnidirectional for these frequencies. However, the printed version represents the best solution from the engineering point of view, thanks to the precision and repeatability of the manufacturing process.

The consideration of this trade-off will be the cornerstone to find out the best candidate between the two solutions proposed.

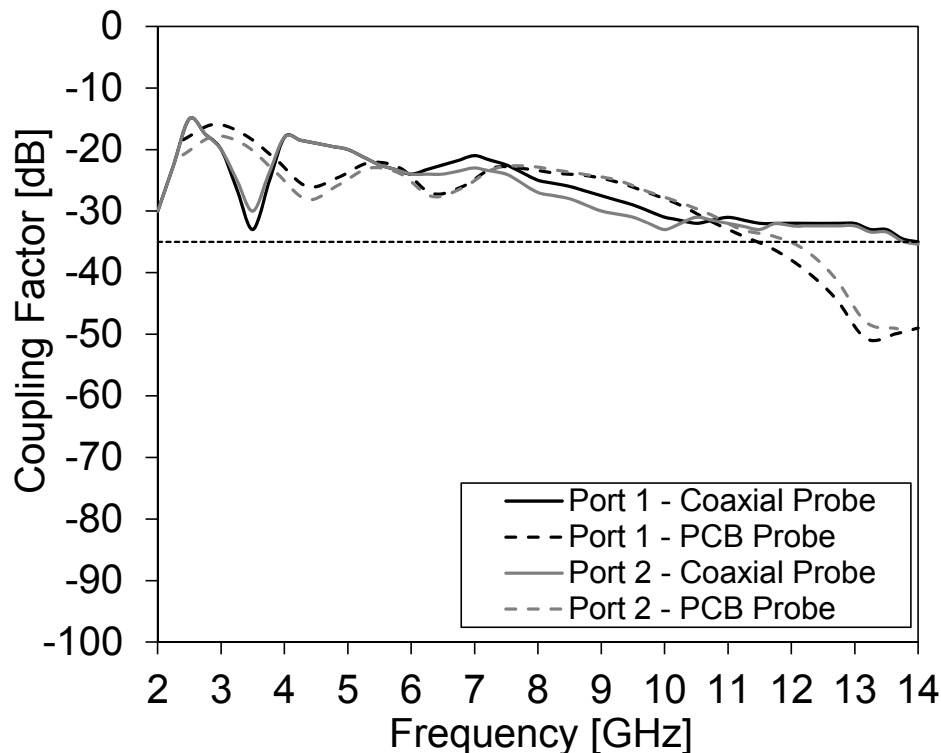


Figure 3.41: Coupling factor of the probe antenna place at 45 degree from the port 1 and the port 2. The black dashed line highlights the specification to be met.



3.5 Conclusions

In this third chapter, the analysis and design of a cryogenic Dewar has been addressed. In particular, this is used to bring the receiver front-end (feed antenna and LNAs) at cryogenic temperatures, and providing in addition its protection against the external agents at once. An optimized structure has been found out through a careful design process in order that the impact of Dewar does not affect strongly the performance of the feed enclosed. Thereafter, a comprehensive RF assessment has been performed on the antenna system characterized by the 12-m Hobart radio telescope, highlighting that the presence of the cryogenic Dewar does not affect the performance of the whole system. Finally, the calibration question has been considered by means the design of two different probe antennas. It has been demonstrated that the printed version represents a good solution and compromise between the manufacturing design and the coupling factor required.



3.6 References

- [1] F. T. Haddock, "Introduction to Radio Astronomy," Proceedings of the IRE, vol. 46, no. 1, pp. 3-12, January 1958.
- [2] R. C. Hansen, Microwave Scanning Antennas – Volume I Apertures, Academic Press, U.S.A., 1964.
- [3] Effelsberg Radio Telescope, official Web site:
<http://www.mpifr-bonn.mpg.de/en/effelsberg>
- [4] Sardinia Radio Telescope (SRT), official Web site:
https://www.med.ira.inaf.it/SRT_page_EN.htm
- [5] Green Bank Radio Telescope, official Web site:
<http://www.gb.nrao.edu/gbt/>
- [6] C. A. Balanis, Antenna Theory: Analysis and Design, 3rd Edition, John Wiley & Sons, 2005.
- [7] Five-hundred-meter Aperture Spherical radio Telescope (FAST), official Web site: <http://fast.bao.ac.cn/en/>
- [8] Arecibo Observatory, official Web site:
<http://www.naic.edu/>
- [9] A. R. Thompson, J. M. Moran, and G. W. Swenson, Jr., Interferometry and Synthesis in Radio Astronomy, J. Wiley & Sons, U.S.A., 1986.
- [10] Very Large Array (VLA), official Web site:
<https://science.nrao.edu/facilities/vla>
- [11] Allen Telescope Array (ATA), official Web site:
<https://www.seti.org/ata>
- [12] Australia Telescope Compact Array (ATCA), official Web site:
<https://www.narrabri.atnf.csiro.au/>
- [13] M. H. Cohen, "Introduction to very-long-baseline interferometry," Proc. of the IEEE, vol. 61, no. 9, pp. 1192-1197, September 1973.
- [14] Thompson, A. R., Moran, J. M., & Swenson, Jr., G. W. 2001, Interferometry and Synthesis in Radio Astronomy, 2nd ed., New York: Wiley.
- [15] M. E. Tiuri, "Radio Astronomy Receivers," IEEE Transactions on Military Electronics, vol.
- [16] Callisto Patent n° WO 2012/038400 A1 "Cryogenic Low Noise Amplifier".



- [17] Callisto Patent n° WO 2011/003929 A1 “Dual Performance Low Noise Amplifier for Satellite Based Radio Frequency communications”.
- [18] “EE406 - MTU Radio Telescope Project Design and Fabrication of the Radio Receiver” Aaron Koslowski, January 13, 1999. Available online at:
http://www.ece.mtu.edu/faculty/wfp/research/radio_astron/mainreport.pdf
(31/10/2017)
- [19] R. Rayet, S. Rawson, T. Bonhoure, M. Sevrin, A. Martellosio, and M. Pasian, “Wideband cryogenic feed receivers for VLBI,” 36th ESA Antenna Workshop on Antennas and RF Systems for Space Science, 6–9 October, ESA/ESTEC, The Netherlands.
- [20] J. L. Casse, E. E. M. Woestenburg and J. J. Visser, “Multi frequency Cryogenically Cooled Front-End Receivers for the Westerbork Synthesis Radio Telescope,” IEEE Trans. Microwave Theory Tech, v o l. 3 0 , no. 2, pp. 201-209, February 1982.
- [21] R. Gawande and R. Bradley, “Towards an Ultra-Wide band Low Noise Active Sinuous Feed for Next Generation Radio Telescopes,” IEEE Trans. Antennas Prop., vol. 59, no. 6, pp. 1945-1953 , June 2011.
- [22] W. A. Imbriale, et al., “The Design and Performance of a Wideband Radio Telescope for the GAV RT Program,” IEEE Trans. Antennas Prop., vol. 59, no. 6, pp. 1954-1962 , June 2011.
- [23] J. Yang et all., “Cryogenic 2 – 13 GHz Eleven Feed for Reflector Antennas in Future Wideband Radio Telescopes,” IEEE Trans. Antennas Prop., vol. 59, no. 6, pp. 1 918-1934 , June 2011.
- [24] A. Akgiray, New Technologies Driving Decade-Bandwidth Radio Astronomy: Quad-Ridged Flared Horn & Compound-Semiconductor LNAs, Ph.D. thesis , California Institute of Technology, U.S.A., 2013.
- [25] Callisto space, official Web site:
<http://www.callisto-space.com/en/>
- [26] Ansys HFSS, official Web site:
<http://www.ansys.com/products/electronics/ansys-hfss>
- [27] J. Lovell et all, “The AuScope VLBI Array,” The AuScope VLBI Array, IVS 2012 General Meeting Proceedings, p.176–180.



- [28] W. A. Imbriale and E. Gama, "Antennas for the Array-Based Deep Space Network: Current Status and Future Designs," Jet Propulsion Laboratory, California Institute of Technology.
- [29] J. Lovell, "The AuScope geodetic VLBI array" *Journal of Geodesy*
- [30] O. Titov, "Effect of the selection of reference radio sources on geodetic estimates from VLBI observations" *Journal of Geodesy*.
- [31] E. Middelberg and U. Bach, "High resolution radio astronomy using very long base line interferometry" *Reports On Progress In Physics*
- [32] B. Petrachenko, "Radio Antennas, Feed Horns, and Front-End Receivers " EGU and IVS Training School on VLBI for Geodesy and Astrometry. Available on line at: http://www.evga.org/teaching/VLBI_school_2013/VLBI-school-2013_02_Petrachenko.pdf
- [33] C. Beaudoin, Overview of the NASA/Haystack VLBI2010 Receiver Frontends, MIT Haystack Observatory. Available on line at: <https://www.yumpu.com/en/document/view/38600869/overview-of-the-nasa-haystack-vlbi2010-receiver-frontends>
- [34] H. Visser, "Low-cost, compact uwb antenna with frequency band-notch function," 2nd European Conference on Antennas and Propagation (EuCAP 2007), Nice, France, November 11–16, 2007.
- [35] A. Martellosio, M. Pasian, R. Rayet, S. Rawson and T. Bonhoure, "Electromagnetic analysis and optimization of a cryogenic receiver for VLBI applications," 2016 10th European Conference on Antennas and Propagation (EuCAP), Davos, 2016.





4 Conclusions

This thesis presented the work carried out by its author during his Ph.D. studies on the analysis and design of protective structure for feed and reflector antennas. The design of these structures has always been very widespread both in the civil and military field, where the main challenge is always to realize high-performance solutions. Although the design process is a compromise between the electrical and mechanical performance, the innovation technology is pushing the engineering to research and development of new structures to satisfy the requests overly stringent from the customers.

The development of this topic followed two parallel roads.

The first, described in detail in the Chapter 2, is oriented to the analysis and design of a Radome structure necessary to protect a 6.4-m Ground-Station intended to be installed at Polar latitudes. This work, carried out in cooperation with the European Space Operations Centre (ESOC) and FDS ITALY S.r.l., takes part in the SNOWBEAR (Svalbard grouNd statiOn for Wide Band Earth observation dAta Reception) system, which will support the future generation of satellite missions that provide the use of K-band down-link channels. JPSS-1, planned by a cooperation of National Aeronautics and Space Administration (NASA) and the National Oceanic and Atmospheric Administration (NOAA), and Metop-SG, planned by a cooperation between the European Space Agency (ESA) and the European Organization for the Exploitation of Meteorological Satellites (EUMETSAT), represent the first candidates for these purposes.

The second, described in detail in the Chapter 3, is oriented to the analysis and design of a cryogenic Dewar necessary to protect and realize the cryogenic cooling of a Quad-Ridge Flared Horn (QRFH) feed antenna. This work, carried out in cooperation with the French company CALLISTO, provides the installation of the cryogenic Dewar on a 12-m radio telescope, located in Hobart (Tasmanian) and planned to operate in the VLBI field.

First of all, both of these topics reported an introductory part in order to assay clearly the kind of structure concerned. Thereafter they have been shown in detail the main aspects to provide the analysis and design with particular reference to the electromagnetic part. In particular, the use of professional software has been essential to outline the electrical performance of these structures. Concerning the first topic, the MLR Radome has been simulated exploiting a combination between MOM (Method of Moments) and



PO (Physical Optic) method, which allowed to derive a comprehensive Radio Frequency (RF) evaluation about its impact on the 6.4-m reflector antenna enclosure. It has been demonstrated that an opportune design and optimization of the MLR Radome allowed to achieve high performance, making this technology one of the best for these applications. The preliminary tests carried out in Svalbard have shown that the impact of the Radome is indeed limited and contained, confirming what expected by the simulated results. Conversely, concerning the second topic, the use of the FEM (Finite Elements Method) method allowed to study and optimize the design of the cryogenic Dewar in order to minimize its influence on the feed antenna enclosed. In addition, the combination with the PO method allowed to analyze its influence on the performance of the whole antenna system. It has been shown that by means electromagnetic investigations it has been possible to identify which part of the Dewar can be modified and optimize appraising its impact on the radiation characteristics of the feed enclosed. This allowed to find out the best design required for this particular application.

Although they have been presented analysis strongly electromagnetic oriented, it has been shown and demonstrated by the results achieved that through an appropriate design based on a fundamental synergy between the electrical and mechanical engineering, it is possible to design and realized high-performance protective structure able to stand up to several impairments.





5 Appendices

5.1 Appendix A: EM evaluation of Radome performance

Ideally a Radome should appear totally transparent to any electromagnetic signal received or transmitted. Since this is an ideal condition, the Radome must be designed to minimize the EM impact on the enclosed antenna. The EM response of Radomes is traditionally analysed using two different parameters: the scattering parameters for the Radome wall and the IFR for the Radome interconnections.

The scattering parameters of the wall are practically always calculated using the transmission matrices for plane-wave incidence, assuming a plane wave incident and an infinite lateral extension. In particular, the scattering parameters for a wall in between two media (medium 1 and medium 2, for Radome applications almost always standard air), can be calculated for the normal incidence following the Eq. A1 and Eq. A2.

$$\Gamma = \frac{A\eta_2 + B - \eta_1(C\eta_2 + D)}{A\eta_2 + B + \eta_1(C\eta_2 + D)} \quad (\text{Eq. A1})$$

$$T = \frac{2\eta_2}{A\eta_2 + B + \eta_1(C\eta_2 + D)} \quad (\text{Eq. A2})$$

Where Γ and T represent the reflection and transmission coefficient of the wall, respectively. η_1 and η_2 represent the characteristic impedances of the medium 1 and medium 2, respectively. A , B , C and D are the four terms of the transmission matrix of the wall, and as anticipated they can be calculated cascading the transmission matrices of each single layer composing the wall.

For example, the transmission matrix of a two-layer wall is calculated by the Eq. A3

$$\begin{bmatrix} A & B \\ C & D \end{bmatrix} = \begin{bmatrix} a & b \\ c & d \end{bmatrix}_1 * \begin{bmatrix} a & b \\ c & d \end{bmatrix}_2 \quad (\text{Eq. A3})$$

Where the coefficients a , b , c and d of each layer (1,2,...i-th) are given by the Eq. A4, A5 and A6, calculated on the basis of the complex propagation constant (k), the physical thickness of the layer (d) and the characteristic impedance (η)



$$a = d = \cos(kd) \quad (\text{Eq. A4})$$

$$b = j\eta \sin(kd) \quad (\text{Eq. A5})$$

$$c = j \frac{1}{\eta} \sin(kd) \quad (\text{Eq. A6})$$

Conversely, as shown in Figure 5.1, the IFR of the interconnection can be calculated simulating (most often using full-wave solvers) or measuring the differential transmission coefficient between two probe antennas, with and without the interconnection under test, according by the Eq. A7.

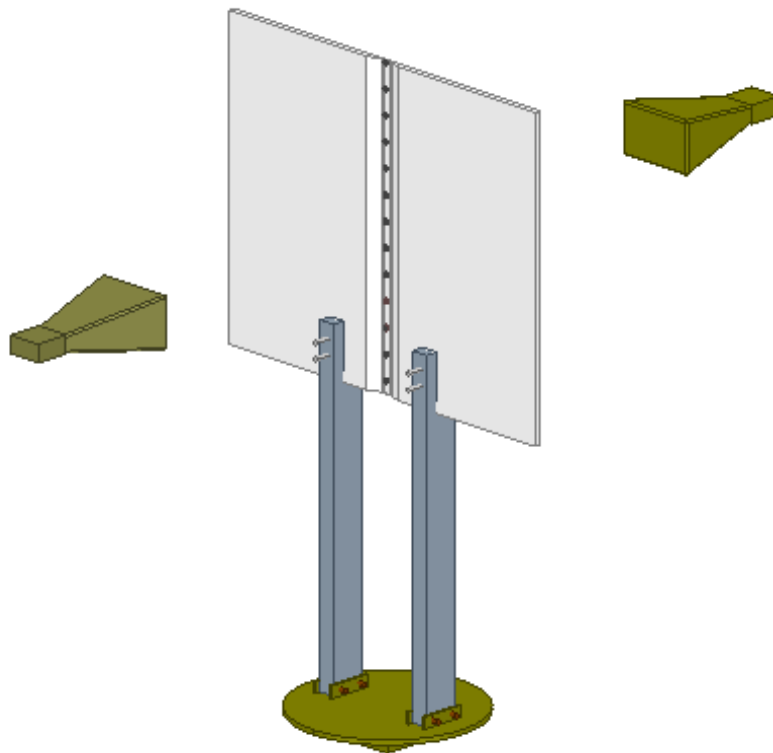


Figure 5.1: Schematic drawing of the setup adopted for the evaluation of the IFR of a Radome interconnection.

$$\text{IFR} = \left(e^{-\Delta\alpha} e^{-j\Delta\varphi} - 1 \right) \sqrt{\frac{\lambda R_1 R_2}{R_1 + R_2}} \frac{e^{j\frac{\pi}{4}}}{w} \quad (\text{Eq. A7})$$



Where $\Delta\alpha$ and $\Delta\phi$ represent the amplitude and phase variation respectively of the incident field on the interconnection, λ is the wavelength, R_1 and R_2 are the distances between the interconnection and the two probe antennas, and w is the width of the interconnection.

The IFR is defined as the ratio of the forward scattered field from the obstacle when illuminated by a uniform plane wave, to the hypothetical field radiated in the same direction by the fields of the same illuminating plane wave when confined to an aperture of the same width as the projected width of the obstacle. The IFR is a complex dimensionless parameter, and is essentially a measure of how strongly the obstacle will block the incident fields by scattering in the forward direction (the direction of propagation of the incident wave). Because it is complex valued, however, it is important to note that its phase as well as magnitude will determine the influence of the obstacle on the net fields in the forward direction.

As example, for a perfectly conducting obstacle such as a metallic interconnection, in the limit of the projected width in wavelengths approaching infinity, the IFR will approach a value of $-1+j0$, which corresponds to purely geometrical blockage with the obstacle casting a geometrical shadow.



5.2 Appendix B: Evaluation of the down-link budget

The T_{SYS} has been calculated for two different scenarios: with and without the Radome. In both cases it is necessary to retrieve the contributions of the antenna (T_{ANT}), the feed (T_{FEED}) and the LNA (T_{LNA}) at the LNA input, as shown in Figure 5.2. As described by the following formulations, the calculation shown by the Eq. B1, B2, B3 and B4, shall take into account several inputs like the cosmic back ground (T_{CMB}), the atmosphere (T_{ATM}), the Radome (T_{RAD}), the antenna (T_{ANT}), the ground (T_{GND}), the feed (T_{FEED}), the LNA (T_{LNA}) and the ensuing receiver block (Down-Converter, IF Amplifier, etc.).

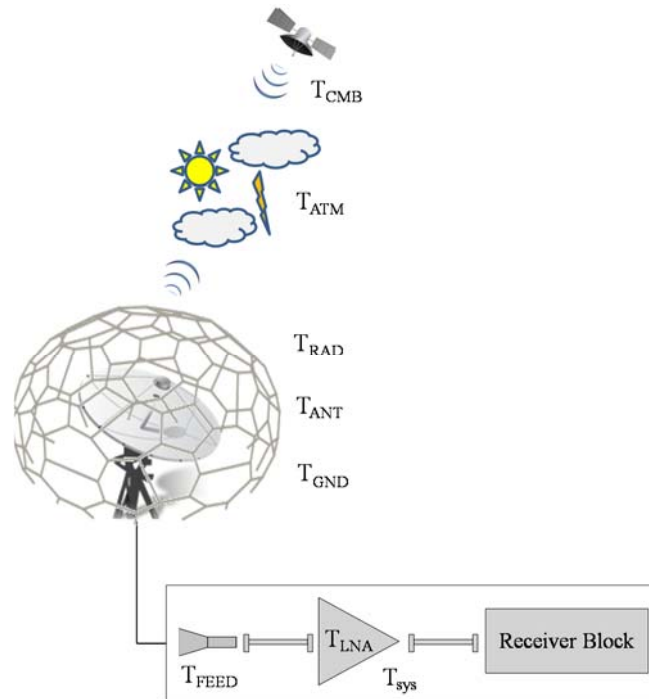


Figure 5.2: Schematic drawings of a SATCOM chain.

$$T_{SYS@LNA} = T_{ANT@LNA} + T_{FEED@LNA} + T_{LNA@LNA} \quad (\text{Eq. B1})$$

Where:

$$T_{ANT@LNA} = T_{ANT} 10^{\left(-\frac{L_{FEED}}{10}\right)} \quad (\text{Eq. B2})$$

$$T_{FEED@LNA} = T_{FEED} 10^{\left(-\frac{L_{FEED}}{10}\right)} \quad (\text{Eq. B3})$$

$$T_{LNA@LNA} = T_{LNA} + \frac{290 \left(1 - 10^{\frac{L_{CA}}{10}}\right)}{10^{\frac{G_{LNA}}{10}}} + \frac{290(NF-1)}{10^{\frac{G_{LNA}}{10}} 10^{\frac{L_{CABLE}}{10}}} \quad (\text{Eq. B4})$$



Computation of the antenna noise temperature (T_{ANT} , as indicated in the Eq. B2)

According to the parameter at issue, the effect of the EL and the CD have to be taken into account.

The T_{ANT} without Radome can be calculated as:

$$T_{ANT(EL,CD)} = T_{SKY(EL,CD)} + T_{GND(EL)} = T_{CMB} 10^{\left\{ \frac{L_{ATM}(CD,EL)}{10} \right\}} + T_{ATMp(CD)} \left(1 - 10^{\left\{ \frac{L_{ATM}(CD,EL)}{10} \right\}} \right) + T_{GND(EL)}$$

While the T_{ANT} with Radome

$$T_{ANT(EL,CD)} = T_{CMB} 10^{\left\{ \frac{L_{ATM}(EL,CD) + L_{RAD}(EL,CD)}{10} \right\}} + T_{ATMp(CD)} \left(1 - 10^{\left\{ \frac{L_{ATM}(EL,CD) + L_{RAD}(EL,CD)}{10} \right\}} \right) + T_{RAD(EL,CD)} + T_{GND(EL)} 10^{\left\{ \frac{L_{RAD}(EL,CD)}{10} \right\}}$$

Where:

- $T_{CMB} = 2.725$ °K.
- L_{ATM} represents the atmospheric attenuation. The correct values as a function of the CD, EL and frequency are computed by the PROPA model (Dynamic Link Library Propagation, developed by CNES [31]).
- $T_{ATMp} = [255 + 25 * CD(\%) / 100]$, and it represents the physical atmospheric temperature.
- T_{GND} is evaluated on the basis of the energy picked up by the antenna reflector. This depends on the antenna EL and as expected it increases with decreasing of the elevation.
- L_{RAD} represents the losses introduced by the Radome.
- T_{RAD} represents the noise temperature of the Radome which can be characterized by three sources:
 - absorption in the wall/panel (T_a);
 - reflection from the wall/panel (T_p);
 - back-scattering by the interconnections (T_j).



The absorption in the panel is described by

$$T_a = 290a_x$$

Where T_a [K] represents the noise contribution due to the Radome panel absorption, while a_x is the power absorbed by the panel itself. In fact, it can happen that a small fraction of the main beam of the antenna enclosed is absorbed by the wall, depending on the frequency and the material used to realize the wall.

The reflection from the panel is described by

$$T_p = T_{bp} * |R|^2$$

Where T_p [°K] represents the noise contribution due to the Radome panel reflection, $|R|^2$ the power reflection due to the panel and T_{bp} the panel brightness temperature. In fact, it can happen that a fraction of the energy reflected by the Radome panel reaches directly the feed either, eventually hits the ground and then into the antenna feed.

A similar situation may happen considering the interconnections of the Radome. Here the back-scattering is described by

$$T_j = T_{bj} \left(1 - 10^{-\frac{L_j}{10}} \right)$$

Where T_j [K] represents the noise contribution due to the Radome joints, L_j the losses introduced by the joints and T_{bj} the joint brightness temperature.

Summarizing all of the contributions just described, the noise temperature of the Radome (T_{RAD}) can be written as:

$$T_{RAD} = T_a + T_p + T_j$$



Computation of the feed noise temperature (T_{FEED} , as indicated in the Eq. B3)

Both in the case with and without Radome, the T_{FEED} depends on the operational conditions. In particular, for the evaluations carried out in this thesis a physical temperature of 290 K has been considered.

Computation of the LNA noise temperature (T_{LNA} , as indicated in the Eq. B4)

In the Eq. B4, it is shown how to calculate the T_{LNA} at the LNA input. In particular, for the evaluations carried out in this thesis the following parameters have been considered:

- $T_{\text{LNA}} = 150$ K (for the K-band).
- $T_{\text{LNA}} = 33$ K (for the S-band).

$L_{\text{C/A}}$ takes into account the losses contributions due to the cable and attenuator:

- $L_{\text{C/A}} = -13$ dB (for the K-band).
- $T_{\text{C/A}} = -12.8$ dB (for the S-band).

G_{LNA} represents the gain of the LNA:

- $G_{\text{LNA}} = 43$ dB (for the K-band).
- $G_{\text{LNA}} = 69$ dB (for the S-band).

NF represents the Noise Figure of the down-converter.

- NF = 17 dB (for the K-band).
- NF = 0.47 dB (for the S-band).

In the Eq. B4 the 2nd and 3rd parameter, that follow T_{LNA} , are practically always negligible.



5.3 Appendix C: Export-Import Grasp to HFSS Transfer procedure

In Figure 5.3 the block diagram of the EIGHT-procedure is shown.

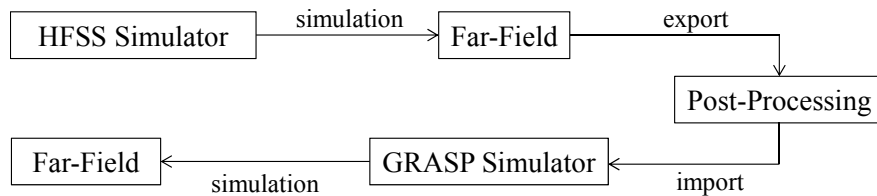


Figure 5.3: Block diagram of the 8-Procedure.

The procedure allows to obtain a tabulated far field simulated by HFSS, suitable to be imported in the GRASP simulator and therefore to be used as the source/feed of the antenna system.

As shown, the procedure requires 5 steps:

1. HFSS Simulator: it concerns the simulation of the element. As general case it can be called simply “antenna”.
2. Far-Field (1): it concerns the exporting phase of the far-field of the antenna simulated by HFSS, in terms of the co- and cross-polarization for different azimuth and elevation cuts.
3. Post-Processing: it concerns the processing of the far-field data in order to achieve a tabulated file suitable to be imported in the GRASP simulator.
4. GRASP Simulator: it concerns the simulation of the antenna in order to interpolate the input tabulated far-field and finally to achieve the radiation pattern.
5. Far-Field (2): it concerns the final step in which the far-field achieved by GRASP can be compared with the far-field achieved by HFSS.



6 Personal Bibliography

INTERNATIONAL JOURNALS

A. Martellosio, M. Pasian, R. Rayet, S. Rawson and T. Bonhoure, "Wideband Cryogenic Receiver for Very Long Baseline Interferometry Applications," in *IEEE Antennas and Wireless Propagation Letters*, vol. PP, no. 99, pp. 1-1.

S. Di Meo, P.F. Espín-López, A. Martellosio, M. Pasian, G. Matrone, M. Bozzi, G. Magenes, A. Mazzanti, L. Perregrini, F. Svelto, P.E. Summers, G. Renne, L. Preda, and M. Bellomi, "On the Feasibility of Breast Cancer Imaging Systems at Millimeter-Waves Frequencies," *IEEE Transactions on Microwave Theory and Techniques*, Vol. 65, No. 5, May 2017.

A. Martellosio, M. Pasian, M. Bozzi, L. Perregrini, A. Mazzanti, F. Svelto, P.E. Summers, G. Renne, and M. Bellomi, "Dielectric Properties Characterization from 0.5 to 50 GHz of Breast Cancer Tissues," *IEEE Transactions on Microwave Theory and Techniques*, Vol. 65, No. 3, pp. 998-1011, March 2017.

A. Martellosio et al., "High-Frequency Radomes for Polar Region Ground Stations: The State of the Art and Novel Developments of Radome Technologies," in *IEEE Antennas and Propagation Magazine*, vol. 59, no. 6, pp. 88-101, Dec. 2017.

A. Coves, E. Bronchalo, G. Torregrosa-Penalva, A.A. San-Blas, M.A. Sanchez-Soriano, A. Martellosio, and M. Bozzi, "A Novel Band-Pass Filter Based on a Periodically Drilled SIW Structure," *Radio Science*, Vol. 51, No. 4, pp. 328–336, April 2016.

A. Martellosio, M. Pasian, M. Bozzi, L. Perregrini, A. Mazzanti, F. Svelto, P.E. Summers, G. Renne, and M. Bellomi, "0.5–50 GHz Dielectric Characterization of Breast Cancer Tissues," *IET Electronics Letters*, Vol. 51, No. 13, pp. 974-975, June 2015.



INTERNATIONAL CONFERENCES

S. Di Meo, P. F. Espin Lopez, A. Martellosio, M. Pasian, M. Bozzi, L. Perregrini, A. Mazzanti, F. Svelto, P. Summers, G. Renne, L. Preda, and M. Bellomi, "Experimental Validation of the Dielectric Permittivity of Breast Cancer Tissues up to 50 GHz," IEEE MTT-S International Microwave Workshop Series-Advanced Materials and Processes (IMWS-AMP 2017), Pavia, Italy, 20-22 Sept. 2017.

A. Martellosio, M. Pasian, F. Concaro and P. Besso, RF Analysis at K band of a Radome-covered Ground Station at Polar Latitudes. 47th European Microwave Conference (EuMC2017), Nuremberg, Germany, Oct. 8–13, 2017.

A. Martellosio, P. F. Espin-Lopez, M. Pasian, M. Bozzi, L. Perregrini, A. Mazzanti, F. Svelto, M. Bellomi, L. Preda, G. Renne, P.E. Summers, "Exposure Limits and Dielectric Contrast for Breast Cancer Tissues: Experimental Results up to 50 GHz". European Conference on Antennas and Propagation, Paris, France, 9-24 March 2017.

A. Martellosio, M. Pasian, L. Perregrini, L. Piffer, R. Riccardi, F. Concaro and P. Besso, "Electromagnetic Analysis of High Frequency Radomes for Ground Stations in Polar Regions". European Conference on Antennas and Propagation, Paris, France, 9-24 March 2017.

A. Martellosio, M. Pasian, R. Rayet, S. Rawson and T. Bonhoure, "Electromagnetic Analysis and Optimization of a Cryogenic receiver for VLBI Applications," European Conference on Antennas and Propagation (EuCAP 2016), Davos, Switzerland, April 10-15, 2016.

P. Espin-Lopez, A. Martellosio, M. Pasian, M. Bozzi, L. Perregrini, A. Mazzanti, F. Svelto, M. Bellomi, G. Renne, P.E. Summers, " Breast Cancer Imaging at mmWaves: Feasibility Study on the Safety Exposure Limits," 46th European Microwave Conference (EuMC2016), London, United Kingdom, Sept. 3–7, 2016.



R. Rayet, S. Rawson, T. Bonhoure, M. Sevrin, A. Martellosio, and M. Pasion, "Wide-band Cryogenic Feed Receivers for VLBI," 36th ESA Antenna Workshop on Antennas and RF Systems for Space Science, ESA/ESTEC, The Netherlands, October 6-9, 2015.

A. Coves, A. A. San Blas, S. Marini, G. Torregrosa, E. Bronchalo, A. Martellosio, "Low-cost Implementation of a Waveguide-based Microwave Filter in Substrate Integrated Waveguide (SIW) Technology," Proceedings of PIERS 2015, Prague, July 6-9, 2015.

A. Coves, A. A. San Blas, S. Marini, G. Torregrosa, A. Martellosio, "Ejemplo practico de disenyo de un filtro en iris rectangular empleando tecnologia SIW para laboratorios docentes," URSI 2014.